Blade surface pressure measurements of an axial flow fan

by
Johannes Nils Rohwer

Thesis presented in partial fulfilment of the requirements for the degree of Master of Engineering (Mechanical) in the Faculty of Engineering at Stellenbosch University

Supervisor: Prof. S.J. van der Spuy

April 2019

Declaration

By submitting this thesis electronically, I declare that the entirety of the work contained therein is my own, original work, that I am the sole author thereof (save to the extent explicitly otherwise stated), that reproduction and publication thereof by Stellenbosch University will not infringe any third party rights and that I have not previously in its entirety or in part submitted it for obtaining any qualification.

Date: April 2019

Abstract

Blade surface pressure measurements of an axial flow fan

J.N. Rohwer

Department of Mechanical Engineering,
University of Stellenbosch,
Private Bag X1, 7602 Matieland, South Africa.

Thesis: MEng (Mech)

April 2019

Large axial flow fans (approximately 10 m in diameter) are implemented in industrial air cooled condenser (ACC) arrays. The fans blow cool ambient air over heat exchanger bundles, causing the turbine exhaust steam to condense into a liquid form. The fans have a high parasitic energy consumption relative to the plant's electricity output. This necessitates more knowledge on possible fan improvements in ACC arrays. Experimental data on the operational fan performance can be used to analyse and further improve existing fan designs.

Fan performance characteristic tests (fan static pressure and efficiency curves) provide information on the global flow field, based on a stable inlet flow field distribution. When testing these fans, more information is often required on the local flow distribution existing in the vicinity of the fan blades. Information concerning the local flow field could prove to be vital in fan design considerations, better understanding of installed fan performance or for numerical validation of localized regions across the fan blade.

The objective of the work is to measure the pressure on the surface of a 1.542 m diameter scale model of an axial fan, termed the M-Fan. The fan is tested at a BS 848, type A test facility at its design operating speed. Experimental tests are conducted to obtain the characteristic curves. The aim of the research is to assess the experimental setup of the M-Fan blade surface pressure measurements by comparison to the results of a CFD model and other existing literature. Two specially constructed M-Fan blades, each with thirty pressure taps at five radial locations are manufactured to conduct blade surface pressure measurements on the fan blades. Piezo-resistive pressure transducers are

mounted inside a capsule which spins on the fan shaft. The data is transferred using a wireless telemetry setup. The results are compared to a periodic numerical model of a fan blade using ANSYS Fluent® version 17.2.

The experimental method and numerical model for the characteristic tests and pressure measurements is firstly verified by testing an existing B2a-fan which was manufactured for blade surface pressure measurements. The experimental characteristic tests and numerical results compare well with each other as well as with literature. The experimental and numerical blade surface pressure measurements also correlate well with each other and have a maximum minimum Pearson correlation factor of 0.955 (average 0.988). A similar method is applied to the M-Fan at its design flow rate. The blade surface pressure measurements have a maximum root mean square error (RMSE) of 95.51 Pa (average 47.95 Pa, minimum 17.36 Pa) and minimum Pearson correlation of 0.941 (average 0.977).

The experimental method used to measure the blade surface pressure is shown to be reliable and accurate for two axial flow fans. This, together with the numerical model, can be used as an effective method to provide further understanding on local flow distribution existing in the vicinity of axial flow fans in air cooled condensers.

Uittreksel

Lemoppervlak-drukmetings van 'n aksiaalvloeiwaaier

J.N. Rohwer

Departement Meganiese Ingenieurswese,
Universiteit van Stellenbosch,
Privaatsak X1, 7602 Matieland, Suid Afrika.

Tesis: MIng (Meg)

April 2019

Groot aksiaalvloeiwaaiers (ongeveer 10 m deursnee) word geïmplementeer in lugverkoelde hitteruilers. Die waaiers blaas koue atmosferiese lug oor hitteruiler bondels wat stoom wat uit die turbine kom in 'n vloeistof laat kondenseer. Die waaiers het 'n hoë parasitiese energie verbruik relatief tot die kragstasie se uitset elektrisiteit (produksie). Dit vereis meer kennis oor moontlike waaier verbeteringe in lugverkoelde hitteruilers. Eksperimentele data oor die operasionele waaiertoestand kan gebruik word om bestaande waaierontwerpe te analiseer en verder te verbeter.

Karakteristieke waaierkrommes (waaier statiese druk en benuttingsgraad kurwes) verskaf inligting oor die globale vloeiveld gebaseer op stabiele inlaatvloeiveldverdeling. Meer inligting oor die plaaslike stroomverspreiding word dikwels benodig. Eksperimentele data oor die plaaslike vloeiveld kan lei tot noodsaaklike besluite oor die waaierontwerp, beter begrip van die werkverrigting van geïnstalleerde waaiers, of vir die numeriese validering van gelokaliseerde gebiede oor die waaier lem.

Die doelwit van hierdie studie is om die druk op die oppervlak van 'n 1.542 m deursnee model van 'n aksiaalvloeiwaaier, genaamd die M-waaier te meet. Die waaier word getoets in 'n toetsfasiliteit wat voldoen aan die Britse Standaard 848, tipe A om die karakteristieke waaierkrommes te bepaal. Die studie mik om die experimentele opstel te asseseer en teen die numeriese model te vergelyk. Twee spesiaal vervaardigde M-Waaier lemme, elk met dertig drukpunte op vyf radiale plekke is vervaardig om die lemoppervlak-drukmetings van 'n

aksiaalvloeiwaaier te toets. Die waaier is by sy ontwerpspoed getoets. Piezoweerstand druk-omsetters word binne in 'n kapsule op die waaier gemonteer. Die data word oorgedra met 'n draadlose telemetrie-opstelling. Die resultate word vergelyk met 'n periodise numeriese model van 'n waaierlem met gebruik van die kommersiële program ANSYS Fluent® 17.2.

Die eksperimentele metode en numeriese model is eerstens geverifieer deur 'n bestaande B2a-waaier wat ontwerp is vir lemoppervlak-drukmetings. Die eksperimentele toetse en numeriese model vergelyk goed met mekaar sowel as met literatuur. Die eksperimentele en numeriese lemoppervlak-drukmetings van die B2a-waaier het 'n minimum Pearson-verwandskapsfaktoor van 0.955 (gemiddeld 0.988). 'n Soortgelyke metode word toegepas op die M-waaier. Die lemoppervlak-drukmetings het 'n maksimum wortel van gemiddeldekwadraadfout (RMSE) van 95.51 Pa (gemiddeld 47.95 Pa, minimum 17.36 Pa) en minimum Pearson-verwandskapsfaktoor van 0.941 (gemiddeld 0.978).

Die eksperimentele metode wat gebruik word om lemoppervlak-drukmetings te meet, word as betroubaar en akkuraat vir twee aksiaalvloeiwaaiers bewys. Dit, tesame met die numeriese model, kan gebruik word as 'n effektiewe metode om die plaaslike vloeiverspreiding wat in die omgewing van aksiaalvloeiwaaiers in lugverkoelde kondensors voorkom, verder te verstaan.

Acknowledgements

Professor S.J. van der Spuy for your supervision, guidance and encouragement throughout the duration of this thesis.

The MinWaterCSP project for their financial support.

Dr. Francois Louw and Mr. Coenraad Swanepoel for your assistance at various stages along the project.

Table of Contents

List of Figures

List of Tables

Nomenclature

Acronyms

ACC	Air cooled condenser
ACHE	Air cooled heat exchanger
ADM	Actuator disk model
BS	British Standards
BSPM	Blade Surface Pressure Measurements
CAD	Computer aided drawing
CFD	Computational fluid dynamics
CSP	Concentrated solar power
EADM	Extended actuator disk model
HPC	High performance computer
LDA	Laser Doppler anemometry
LES	Large eddy simulation
N-S	Navier-Stokes
P3DM	Periodic three-dimensional model
PC	Personal computer
PIV	Particle image velocimetry
RANS	Reyolds averaged Navier-Stokes
REEADM	Reverse engineered empirical actuator disk model
RMS	Root mean square error

Variables

A	Area	$[\mathrm{m}^2]$
a	Acceleration	$[\mathrm{m/s}^2]$
c	Absolute Velocity	$[\mathrm{m/s}]$
c_t	Tip clearence	$[\mathrm{m}]$
ch	Chord	$[\mathrm{m}]$
D	Drag	$[\mathrm{N}]$

d	Diameter	[m]
F	Force	[N]
K	Loss coefficient	[−]
k	Turbulence kenetic energy	[J/kg]
L	Lift force	[N]
$\dot{m}$	Mass flow	[kg/s]
N	Rotational speed	[rev/min]
P	Power	[W]
p	Pressure	[Pa]
R_p	Pearson correlation factor	[−]
T	Torque, Temperature	[Nm, K]
U_c	Blade tip speed	[m/s]
V	Volume	[m^3]
$\dot{V}$	Volumetric flow rate	[m^3/s]
v	Velocity	[m/s]
w	Relative Velocity	[m/s]
x/ch	Dimensionless chord length	[−]
z	Axial length	[m]

Greek symbols

α	Absolute flow angle	[°]
β	Relative flow angle	[°]
ε	Turbulence dissipation rate	[J]
η_{tt}	Total-to-total efficiency	[%]
η_{ts}	Total-to-static efficiency	[%]
θ	Angle	[°]
μ	Dynamic viscosity	[kg/m · s]
ξ	Stagger angle	[°]
ρ	Density	[kg/m^3]
σ	Standard deviation	[−]
ϕ	Flow coefficient	[−]
ψ_{Fs}	Static pressure coefficient	[−]
ω	Rotational speed	[rad/s]

Subscripts

a	Air

ann	Annulus
atm	Atmosphere
att	Angle of attack
avg	Average
c	Casing
ch	Chord
D	Drag force
d	dynamic
dim	Dimensionless
eff	Effective
F	Fan
Fs	Fan static
Ft	Fan total
L	Lift
m	Measured
o	Outer
p	Pressure
$plen$	Plenum
R	Radial Force
Res	Resultant
ref	Reference
s	Static
t	Tip clearence, Total
tap	Tap
$trans$	Transducer
x	Cartesian coordinate x
y	Cartesian coordinate y
z	Cartesian coordinate z
$zero$	Zero

Miscellaneous

g	Gravitational constant	$[9.81\ \mathrm{m/s^2}]$
R	Gas constant of air	$[287\ \mathrm{J/kgK}]$
Re	Reynolds number	$[-]$

Chapter 1

Introduction

1.1 Background

Air-cooled heat exchangers (ACHE) hold environmental and economic advantages in arid regions due to their reduced water consumption when compared to wet-cooled heat exchangers. The focus of this research is on an axial flow fan designed to fit into a typical A-frame design of the forced draught air-cooled condenser (ACC) shown in figure 1.1. Air-cooled condensers are commonly used in direct cooled power plants and are arranged in large condenser arrays.

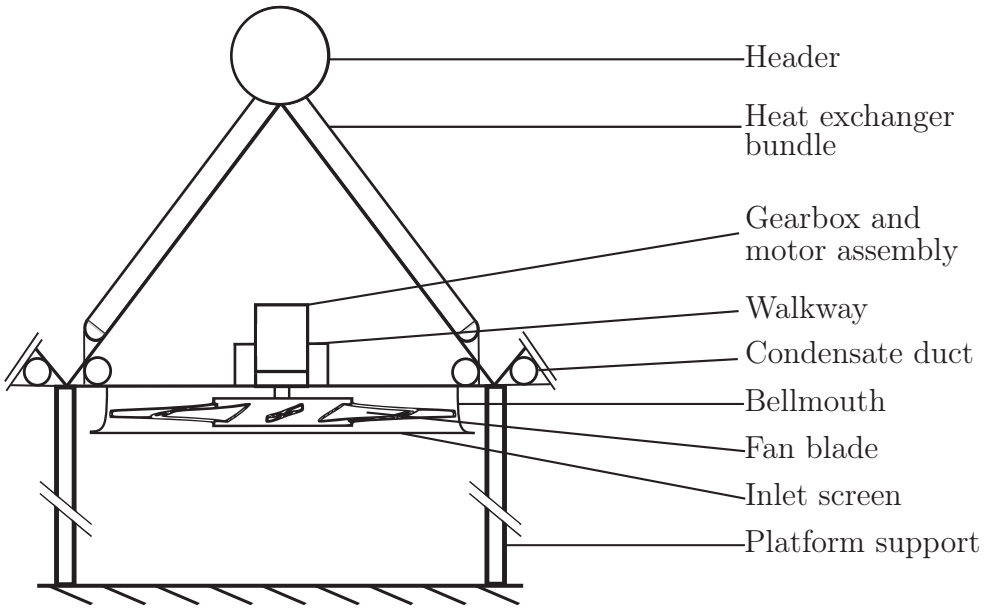

Figure 1.1: A-frame forced draught air-cooled condenser

An ACC consists of a series of heat exchanger bundles which receive steam from the turbine exhaust via a common steam header. The steam flows through finned tube heat exchanger bundles which reject heat to the ambient air, allowing the steam to condense. Large axial flow fans, approximately 10 m in diameter are driven through an electric motor and gearbox assembly. The fans force cool ambient air through the heat exchanger bundles. The steam condensate is collected in the condensate ducts at the bottom of the ACC.

One drawback of forced draught ACHEs is their reduced thermodynamic efficiency due to their higher condensing pressure, compared to wet-cooled heat exchangers. Another drawback is the relatively high parasitic energy consumption of the axial flow fans when compared to wet cooled heat exchangers. The Matimba coal-fired power plant has 6 x 665 MW(e) units and requires approximately 65 MW to power the axial flow fans in the ACC system at full load (Van der Spuy, 2011). One way of reducing this power loss is to implement more efficient axial flow fans. Experimental data on the operational fan performance can be used to analyse and further improve existing fan designs.

Fan performance characteristic tests (fan static pressure and efficiency curves) provide information on the global flow field, based on stable inlet flow field distributions. These tests usually require large test facilities adhering to industry specific standards. When testing axial flow fans, more information is often required on the local flow distribution existing in the vicinity of the fan blades. Information concerning the local flow field could prove to be vital in fan design considerations (e.g. flow distribution, local lift and drag performance characteristics), better understanding of installed fan performance under distorted inflow conditions or for numerical validation of specific/localized regions across the fan blade.

Bruneau (1994) designed a 1/6th scale low pressure rise axial flow fan for large ACHE application, termed the B-Fan ($d_c = 1.543$ m). This was followed by extensive simulation, testing and analysis by authors such as Stinnes and Von Backström (2002) and Augustyn (2013). Louw (2015) investigated a slightly modified version of the B2-fan, which used cylindrical aerofoil sections stacked along the blade radius. This was termed the B2a-fan, details of which can be found in Appendix A.1. The fan has a static pressure rise of 210 Pa and volume flow rate of 16 m^3/s ($c_t = 3$ mm) at its operating point. Blade surface pressure measurements (BSPM) were used to experimentally validate a numerical model at various flow rates.

Wilkinson (2017) designed an axial flow fan for a large ACHE, termed the M-Fan ($d_c = 7.3152$ m). The design requirements are based on the MinWaterCSP project (MinWaterCSP, 2018). The design requires a significantly lower pressure rise when compared to the B2a-fan. Wilkinson *et al.* (2018) conducted

numerical simulations and experimental tests on a scale model ($d_c = 1.543$ m) of the M-fan, details of which can be found in Appendix A.1. At a design blade setting angle of 34° and a tip clearence (c_t) of 2 mm, the fan exhibits a static pressure rise of 96 Pa at a flow rate of 14.4 m^3/s (Wilkinson *et al.*, 2018). Further performance testing of the scale M-Fan is required to provide more information for future analyses of the full scale M-Fan.

1.2 Objectives

The objectives for this research apply to the scale M-Fan ($d_c = 1.542$ m) and are to:

- Numerically model the fan at its design operating point.
- Experimentally test the fan to determine its performance at various operating points (fan characteristic curves).
- Conduct blade surface pressure measurements at the design operating point.
- Compare the results of the numerical simulation with the experimental results.

1.3 Project overview

This project forms part of the MinWaterCSP project which has the overall goal of minimizing water consumption in concentrated solar power (CSP) plants. One of its objectives is to improve the current fan static efficiency of axial flow fans (MinWaterCSP, 2018). This thesis aligns with the project goal of evaluating the axial flow fan performance in an effort to further understand and improve the AFF design. A large ACC test facility (with the full scale M-fan installed) is currently being constructed at Stellenbosch University. Information regarding to the performance and manufacturing (for BSPM measurement) of the M-Fan can be used for research on the full scale M-Fan.

Chapter 2

Literature Review

This literature study provides a brief explanation of the fundamentals concerning axial flow fans. This is followed by a description of their design procedure and off design operating conditions encountered in ACCs. The last two sections investigate the numerical modelling and experimental tests conducted on axial flow fans.

2.1 Fundamentals of axial flow fans in ACC

The heat rejection rate of an aircooled condenser is dependent on the airflow provided by the axial flow fan. A higher air flow over the heat exchanger bundles results in a higher heat rejection rate but comes at the expense of higher fan power consumption. The performance parameters of an axial flow fan are determined by the required (design) air flow rate over the heat exchanger bundle and the pressure difference needed to overcome this. Additional pressure losses caused by walkways, support structures and wind screens need to be accounted for as well. Noise is also a performance factor but can be seen as secondary as it is usually dependent on regulatory restrictions of the site location. An axial flow fan is most often designed to run close to its highest possible efficiently at its operating point while not being too expensive.

The fundamental functioning of a fan blade works on the principle of an aerofoil, shown in figure 2.1. An aerofoil is formed from a two dimensional wing profile which has an aerodynamic lift to drag ratio of ten or more (Wallis, 1983). The chord is defined as the shortest distance from the leading edge to the trailing edge. The camber line is a line which is half-way between the upper and lower aerofoil surfaces and the angle of attack (α_{att}) is the angle

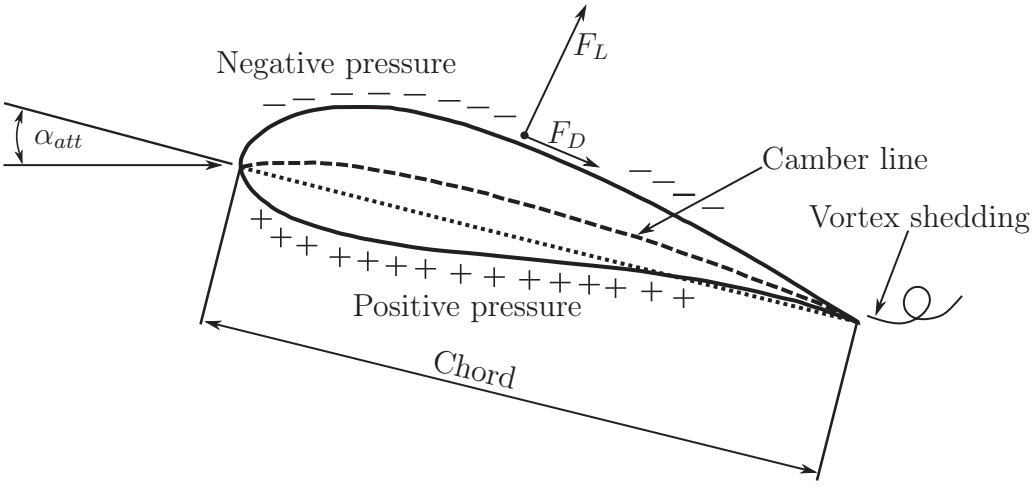

Figure 2.1: Two dimensional aerofoil profile

between the direction of airflow and the chord. The deflection of air and reduction in static pressure over the upper surface of the profile results in a net lifting force exerted on the aerofoil, perpendicular to the air flow direction. A drag force that exists parallel to the flow is caused primarily by skin friction. Stall occurs when the angle of attack has increased past a critical angle and the lifting force exerted on the aerofoil decreases. This is due to high flow separation at the upper surface of the aerofoil.

The axial flow fan under investigation consists of a number of aerofoil profiles at various radial stations along the blade, which are stacked around a common point, in this case the centroid of each respective profile. They are curved around their respective blade radius to accommodate the rotational motion of the rotor. A velocity diagram of an aerofoil section as well as the force components exerted on the axial flow fan aerofoil profile is shown in figure 2.2. The mean relative velocity vector ($\omega_{\theta z,\infty}$) consists of the mean axial velocity through the fan ($\omega_{z,\infty}$) and the mean tangential velocity ($\omega_{\theta,\infty}$) at the specific radius. The mean tangential velocity is the absolute tangential velocity subtracted from the fan blade speed (ωr). The angle between the chord line and $\omega_{\theta z,\infty}$ is defined as the angle of attack (α_{att}) while β is the relative inlet velocity angle. The angle between the chord line and axial direction is refered to the as the stagger angle (ξ).

As the radius of the fan increases, so does the tangential velocity. This requires various aerofoil configurations along the blade radius to promote efficient operation and reduce blade stall. The blade root typically has a higher camber angle than the blade tip. Various aerofoil designs and chord lengths can be employed throughout a blade. Kröger (2004) states that increasing the num-

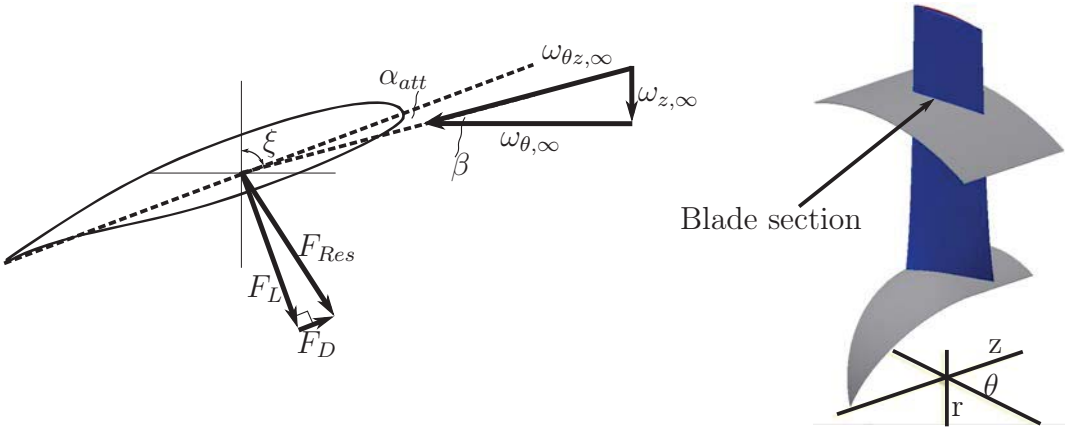

Figure 2.2: Velocity triangle and two-dimensional forces exerted on a M-fan aerofoil section

ber of fan blades can lead to an increased fan efficiency or lower fan noise but this comes at a higher manufacturing cost.

2.2 Axial flow fan design

Fans are designed to achieve their desired operating point while minimizing the losses caused by the deflection of flow around each blade. Two design approaches are used to achieve this: free vortex or controlled (non-free) vortex. The later incorporates a radial component along the blade, resulting in a different downstream vortex distribution when compared to the free vortex distribution.

Wallis (1983) considers the free vortex distribution to be the simpler of the two approaches. The distribution results in a spanwise uniform axial velocity, neglects any radial velocity component along the blade and results in a two dimensional problem. Van Niekerk (1958) investigated the theoretical total to static efficiency η_{ts} of a fan designed with a free vortex distribution and found that it could be in excess of 70 % (design parameter dependent). This however led to unwanted high turning angles at the blade root. Wallis (1983) adjusted this approach by limiting the turning angle at the hub such that back flow would not occur at the design operating point. This resulted in good theroretical static efficiency values of 65 %.

Van Niekerk (1958) developed an optimization method for the hub-to-tip ratio of a free vortex axial flow fan (with flow vanes). Bruneau (1994) modified this

by applying an additional relaxation factor to the blade stagger angle near the hub to extend the stall margin. He designed the B2-fan and experimentally tested it in a BS 848 type A test facility, achieving a total to static efficiency of 64 %. Louw (2012) assessed this fan to perform best when compared to some commercial fan designs (V-, DL- and L- fan).

There are however design requirements or cases which are not optimal for free vortex designs, some of which are suggested by Downie *et al.* (1993) and Vad and Bencze (1998). This then favours the use of the controlled vortex design approach. As mentioned, it incorporates a radial component in the velocity distribution over the blade. The disadvantage as stated by Vad (2008) is that the radial flow component can increase flow losses at the blade tip and have poorer stall behaviour when compared to free vortex design.

Downie *et al.* (1993) states that well designed vortex controlled fans are efficient and have low noise emissions. Several controlled vortex designs have been successfully implemented as shown by Sørensen *et al.* (2000) and Bamberger and Carolus (2012), achieving a total to static efficiency of 68 %. Bamberger and Carolus (2014) made use of artificial neural networks in a parametric study on fans. They showed that fans with a low hub-to-tip ratio have a high efficiency.

Based on the literature surveyed, both controlled and free vortex fan designs

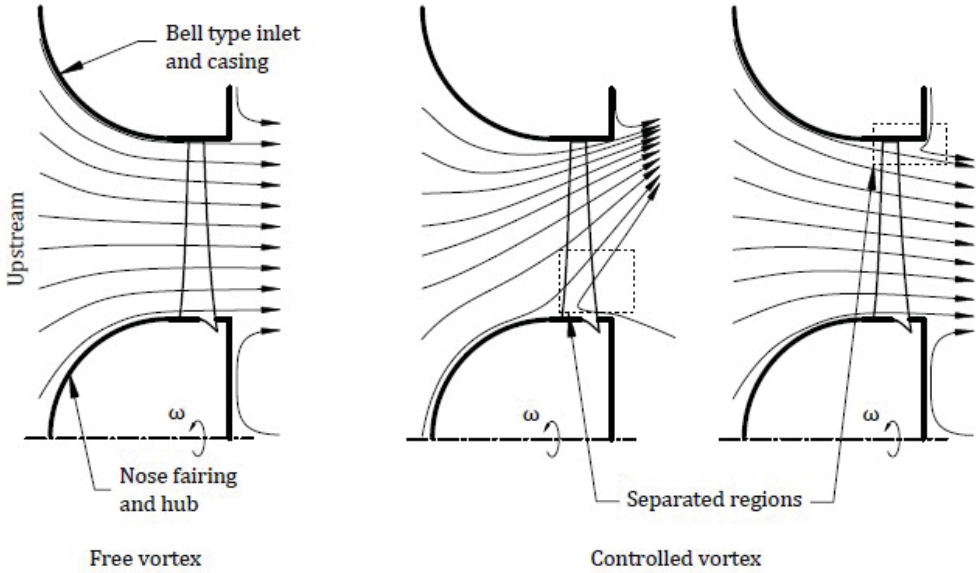

Figure 2.3: Two dimensional flow profile though a free vortex and controlled vortex design (Louw, 2015)

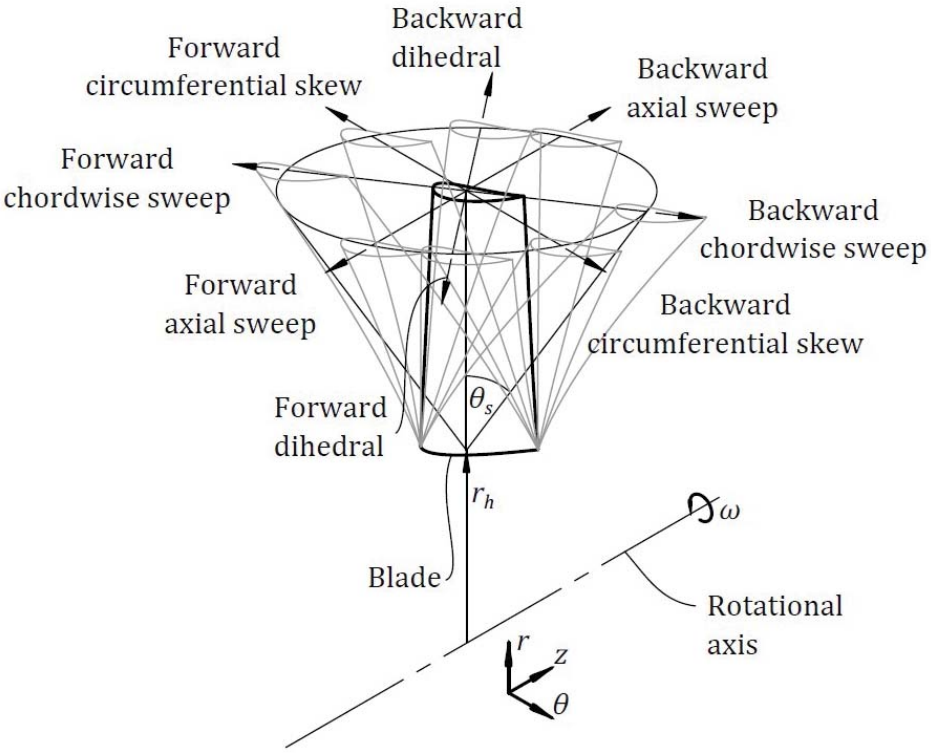

Figure 2.4: Definitions of blade sweep directions (Louw, 2015)

show high total to static efficiency values. Louw (2015) argues that the controlled vortex design can be seen as a mixed flow machine and can operate away from their optimal condition due to the separation effects. He states that efficient controlled vortex designs rely much more on the designer's ability when compared to free vortex design.

2.3 Blade sweep

Blade sweep refers to the non-symmetric radial stacking of blade sections, i.e. individual blade sections that are stacked in a certain direction. Blades can be swept in the chord wise, axial, circumferential or normal to the chord profile (dihedral) direction as shown in figure 2.4. The most prevalent fan blade sweep method found in literature is forward and backward sweep.

Forward sweep leads to unloading of the blade tip region and increased loading near the blade root. This reduces the losses associated with tip clearance when compared to an upswept blade Louw (2015). This especially complements

controlled vortex fans (as the flow has a radially outward migration) especially on the suction side, which is most prone to stall (Vad *et al.*, 2007). The peak efficiency of forward swept blades are either higher or the same as unswept blades at different operating points. This is shown in the work of Corsini and Rispoli (2004),Li *et al.* (2008), Vad *et al.* (2007) and Hurault *et al.* (2010). Most of these studies were either conducted on controlled vortex fans or fans of unknown vortex distribution.

Vad *et al.* (2007) showed that forward sweep changes the radial velocity distribution through the fan rotor. Radial velocity in the blade decreased with forward sweep and increased with backward sweep. Backward sweep therefore lends itself to more favourable conditions for stall to occur. Forward swept blades are found to increase the stall margin of a fan operating at lower flow rates as found by Wadia *et al.* (1998), Corsini and Rispoli (2004),Vad (2008) and Masi *et al.* (2016). An advantage of forward sweep in axial flow fans is the decrease in noise emissions as shown in the work of Beiler and Carolus (1999) and Kergourlay *et al.* (2006).

Backward sweep does not seem to have any benefit on axial flow fans (Corsini and Rispoli, 2004). Studies by Beiler and Carolus (1999) have shown that backwards sweep results in higher noise emissions and lower performance when compared to blades with no sweep.

2.4 Off design conditions

So far, the focus has been on ideal flow conditions i.e. that of a fan with uniform inlet flow and no downstream interference. The AFF in this study is installed in ACC arrays which may be subjected to adverse inlet flow conditions. Flow recirculation can also occur in ACC arrays (Louw *et al.*, 2014) but this is not necessarily directly related to axial flow fans and will not be investigated in this study. Off-design conditions result in lower volume flow rate through the fan and reduced total to static efficiency (Wilkinson, 2017). Goldschagg (1993) notes that in some cases there can even be reversed flow in axial flow fans due to these adverse inflow conditions.

In forced draught heat exchangers, axial flow fans have a vertical axis of rotation. The upstream flow enters at an angle, which in its most extreme case can be perpendicular to the axis of rotation. This adverse inflow condition is known as crossflow and has been investigated in numerous studies.

Venter (1990) experimentally measured the velocity field upstream of an operational axial flow fan at the Matimba Power plant. He concluded that an

increase in wind speed reduced the volume rate through the fan. Salta and Kröger (1995) experimentally tested a scale model of a street of heat exchangers. They show that axial flow fans around the periphery are most effected while their performance improves towards the middle. This is also shown in the works of Van der Spuy *et al.* (2009), Van der Spuy (2011) and Meyer (2005).

Meyer (2005) numerically modelled two banks of an ACHE and shows that the loss in the edge fans is due to flow separation occurring at the inlet bell mouth and the losses in fans further away from the periphery are due to oblique (skew) inlet flow. Van der Spuy (2011) conducted a detailed numerical and experimental investigation on a number of fans subjected to distorted inflow conditions and found that the distorted flows reduced the volumetric flow rate of the fans and could result in the fan running off its desired design operating range.

Van der Spuy *et al.* (2009) numerically simulated the performance of axial fans under installed conditions. He concluded that fans having a steeper static performance curve are less sensitive to flow distortions. It was also noted that the skew inflow conditions cause localised regions of high velocity and increased fan noise.

Venter (1990) and Stinnes and Von Backström (2002) show that fan hub configuration can reduce some of the effects caused by off design conditions in an ACC. Van der Spuy *et al.* (2009) notes that fans with larger hub to tip ratios performed better in adverse conditions.

Stinnes and Von Backström (2002) conducted a series of experiments on fans which were subjected to cross flow using inlet ducts at specific angles to the plane of rotation. They successfully derived a model to describe the decrease in performance due to off-axis inflow.

2.5 Axial flow fan modifications

Small modifications to axial flow fans have been investigated in order to ascertain their ability to increase the performance or reduce the noise emissions. Venter (1990) experimentally investigated the losses in fans which do not seal at the fan hub. This is often due to manufacturing or for installation reasons (Wilkinson and Van der Spuy, 2015). Venter (1990) found that reversed flow occurred at the root gap region and reduced the total to static pressure rise. The performance was improved by placing a steel disk downstream of the fan. Bruneau (1994) extended the hub in the axial length of the blade. This

increased the static pressure rise and total to static efficiency.

Tip clearance is defined as the distance between the fan blade tip and casing. Tip leakage occurs when air flows from the downstream high pressure side to the lower pressure upstream (inlet) side of the fan through the tip gap. Venter and Kröger (1992) determined an empirical formula in which they show a linear drop in efficiency with increasing tip clearance around the axial flow fan's practical operating range. This was also found in Wilkinson and Van der Spuy (2015), although the empirical formula differed, after which they concluded that the formulas are fan (design) specific. Noise levels generally increase with tip clearance (Hunnabal, 1992).

Winglets are small sections which are added to the fan blade tips. Kröger (2004) states that they reduce vortex development and thereby reduce noise. Corsini *et al.* (2007) and Corsini *et al.* (2010) investigated various endplates to reduce tip gap losses. The winglets either did not influence the performance or slightly improved fan performance and reduced noise emissions. Wilkinson and Van der Spuy (2015) used more basic square endplates on the blade tips of the B2a-fan and found that they could improve fan performance at larger tip clearances.

Serrated unswept blades were investigated by Longhouse (1977), who showed that the fan had an increased efficiency (max. 3 %) and lower noise at the operating point but emitted higher noise at low flow rates. Ye *et al.* (2015) simulated the effects of tip grooving on an axial fan in ANSYS Fluent. The results show an increase in noise and a maximum increase of 1 % in total to static efficiency at the design flow rate.

2.6 Numerical modelling

Recent developments in computational processing power have made computational fluid dynamics (CFD) very popular for modelling the flow around an axial flow fan. CFD can either be performed by modelling the flow around a full three dimensional (3D) axial flow fan or by using a simplified model which replicates the flow of the fan with representative terms. The 3D model is more computationally expensive and provides more detail on the localized flow around the fan. The simplified model is less computationally expensive and could result in a less accurate solution.

From the literature surveyed, only two authors were found to have modelled the entire fan rotor with all the blades present: Lee *et al.* (2005) (annular duct) and Ye *et al.* (2015) modelled their fans in an open inlet to outlet annular duct.

The other fifteen studies surveyed, all made use of a periodic section of the fan with only one blade.

The majority of the literature surveyed makes use of an annular model to simulate the upstream and downstream flow field of an axial flow fan. This is done by extending the hub and shroud in the axial direction from the flow inlet to outlet. Only a few studies make use of open-inlet to open-outlet configurations. The latter being more computationally expensive due to the more complex grid required and solution thereof. More specific to this thesis is the work of Louw (2015) and Augustyn *et al.* (2016), who modelled flow domains to simulate flow in a BS 848, type A test facility.

2.6.1 Full 3D modelling

Most practical CFD simulations, which are often in the turbulent flow regime, require solving the Navies-Stokes (N-S) equations. The fundamental flow equations needed to simulate flow are given in Appendix B. These can be solved by Direct Numerical Simulation (DNS), Large Eddy Simulation (LES) or by making use of the Reynolds Averaged Navier-Stokes (RANS) models.

DNS directly solves the N-S equations. It comes at a very high computational cost, which often exceeds available computational power. It is however a useful tool for further research in fundamental turbulence modelling. LES uses a special filtering technique to categorize eddies according to their size. The larger ones are calculated directly while the smaller ones are modelled (Versteeg and Malalasekera, 2007). Even though it is less computationally expansive than DNA, it is still too computationally expensive for axial flow fan models that evaluate large flow domains and different flow rates. The third and most computationally economical approach are the use of RANS models. This requires solving the Reynolds stresses by making use of turbulence models, as detailed in appendix B.1.

The Spalart-Allmaras turbulence model (Spalart and Allmaras, 1992) is a one equation model that solves for the kinematic eddy viscosity using a single transport equation. It is used to solve the viscous sub-layer close to the wall and therefore requires a very fine mesh (reqired y^+ value of 1). The model shows good results for two dimensional flow with adverse pressure gradients. It does however perform poorly in three dimensional flow with abrupt changes from wall bounded to free shear flow (Versteeg and Malalasekera, 2007). This does not bode well for AFF flow modelling and also requires a computationally expensive (dense) mesh close to the walls.

The k-ε model of Launder and Spalding (1974) is a two equation model which

uses a turbulent kinetic energy (k) and a dissipation rate (ε) term to model turbulent viscosity. Various wall functions can be used to resolve the flow near the element wall, each with their acceptable range of y^+ values. Versteeg and Malalasekera (2007) describes it as being very robust, economical and applicable for a wide range of CFD simulations. The k-ε model is the most common model used in axial flow fan modelling due to its comparatively low computational expense and good correlation with experimental results (Louw, 2015) and (Wilkinson and Van der Spuy, 2015). Beiler and Carolus (1999) investigated skewed blades and found that the Standard k-ε model shows good correlation between experimentally determined span wise axial velocity distributions across an axial flow fan. Accurate modelling using this model is also shown in the work of Corsini and Rispoli (2005).

More recent non-linear models of the k-ε model such as the Cubic k-ε model of Lien and Leschziner (1994) and Realizable k-ε model of Shih *et al.* (1995), model the flow separation of swirling flows in turbomachinery well at a comparatively low computational expense (Wilkinson and Van der Spuy, 2015). Shih *et al.* (1995) notes that the Realizable k-ε model accurately predicts flow where separation, rotating flow and adverse pressure gradients are present. More details of the model along with its wall functions are provided in Appendix B.2.

Mention must be made of two further RANS models: the k-ω model of Wilcox (1988) and the Shear stress transport (SST) model of Menter (1994). The k-ω model is a two equation model which makes use of turbulence frequency as a second variable in the length scale. The k-ω model was specifically designed for aeronautical applications and gives good predictions across a range of aerofoils (ANSYS Fluent Inc., 2017). The SST model uses a blending function to combine the k-ω model and the k-ε model where appropriate. Louw *et al.* (2012) compared the various turbulence models at steady state and noted that they all resulted in similar results at the operating point of the B2a-fan.

2.6.2 Simplified modelling

Simplified axial flow fan models are typically employed in large 3D simulations (e.g. ACC arrays) where the number of cells used to model fans can be significantly reduced.

The Pressure Jump Model (PJM), models an AFF as a pressure discontinuity by making use of the specific fan test data. Owen and Kröger (2010), Louw (2011) and Van der Spuy (2011) used this model to simulate the flow in condenser bays. The PJM is however not relevant to this study as it does not

simulate the localized flow around an AFF needed for an in depth performance analysis.

The Actuator Disk Model (ADM) was originally developed by Thiart and von Backström (1993) and stems from the work of Pericleous et al (1987). A momentum source term is calculated from two dimensional blade element theory. The model contains some detail concerning the localized flow field through an axial flow fan (e.g. swirl velocity component), pressure rise through the fan and power consumption.

The ADM has successfully been implemented in modelling ACC arrays as shown in the work of Van der Spuy (2011) and Bredell (2005). Meyer and Kröger (2001) obtained good results when comparing an ADM model of the B2a-fan with its respective experimental results (BS 848, type A test facility). Wilkinson *et al.* (2018) shows good correlation between the ADM and experimental results obtained for the M-Fan. The ADM does under predict fan performance at low flow rates as shown by Louw (2015), Van der Spuy (2011) and Wilkinson *et al.* (2018). Meyer and Kröger (2001) reasoned that this is due to radial flow increasing at low flow rates, which the ADM does not account for.

The lift and drag coefficients of two dimensional aerofoils differ when they are in a rotational plane (Himmelskamp, 1947). This finding was incorporated by Van der Spuy (2011) into the development of the extended actuator disk model (EADM). The standard ADM model is modified with empirical rotating lift and drag coefficients. This was done by extending the linear part of the lift and drag profile. The model shows improved results at low flow rates but over predicts at high flow rates (Van der Spuy, 2011). A further model termed the reverse engineered empirical actuator disc model (REEADM) was developed by Louw (2015). It incorporates a radial source term based on a three dimensional study. This performed slightly better than the EADM but comes at the expense of performing the three dimensional simulation needed in order to determine the source terms.

2.7 Experimental tests

The performance characteristics of an axial flow fan can be determined using standard test facilities, such as those described by the BS 848 test facility. Other experimental methods are however required to analyse the local flow fields surrounding the fan blades. The following techniques will be briefly discussed: hot wire anemometry (HWA), optical techniques, multi-hole probe measurements and BSPM.

A hot wire anemometer contains electrically heated wires over which a gas flows. Heat from the electric wires is transferred to the moving gas stream, causing the wires to cool down. This results in a change in electric resistance which corresponds to the gas flow rate. HWA allows for a fast response rate and therefore lends itself well to rapid velocity measurements (high gradients). Beiler and Carolus (1999) used HWA to measure the downstream flow field of an AFF. Good correlation was shown between their numerical and experimental results.

Optical techniques are non-intrusive and use lasers to track artificially inserted particles (tracers) into the fluid flow. The most common techniques are Particle image velocimetry (PIV) and Laser Doppler Anemometry (LDA). PIV uses a pulse laser to illuminate small tracer particles in the moving fluid. Each pulse is visually recorded and post processed for cross sectional velocity maps and flow visualization. LDA is by far the more complicated and only its basic functioning is discussed. At the measurement volume (order of mm), two laser intersecting beams of known frequency produce parallel planes of high intensity light. The tracers scatter light, which causes a Doppler shift (change in frequency) which corresponds to a flow velocity.

Estevadeordal *et al.* (2000) conducted digital PIV measurements downstream of an axial flow fan. These showed steady and unsteady flow field visualizations. Yoon and Lee (2004) investigated flow behind an axial fan rotating in a water tank using PIV. Various flow patterns concerning the fan wake were observed. Ubaldi *et al.* (1994) measured the flow within an AFF using LDV which showed the pressure distribution along the blade. Vad *et al.* (2006) investigated the blade loading of forward and backward swept AFF using LDA.

Multi-hole probes have individual holes at different locations measuring the pressure induced by the flow. The magnitude and direction of flow can then be determined from a pressure differential between the holes. Downie *et al.* (1993) used a cobra 4-hole probe to measure the downstream flow distribution of three different axial flow fans. The experimental data shows similar results to that of the design (theoretical) velocity profile.

BSPM measure the static pressure on the blade. This is done by either having a pressure sensing device in the blade or tubes inside the blade transferring the static pressure to an outside pressure sensing device. Himmelskamp (1947) successfully recorded BSPM on a rotating propeller with a series of tubes located on the inside of the blade. The rotating tubes were connected through seals which then connect to manometers during experimental runs. The experimental results showed the pressure distribution along the blade profiles. Schreck (2007) conducted BSPM on a large 10 m diameter horizontal axis wind turbine. The blades were large enough to house the pressure transducers in

the blade cavity. The data was then used to derive normal force coefficients and compared to the mean flow field states. Hurault *et al.* (2012) conducted BSPM to investigate pressure fluctuations on an automotive cooling fan. This was done by moulding piezo resistive sensors in the fan. Good comparisons were obtained between the experimental and numerical results.

Louw (2015) conducted BSPM by the use of pressure taps and tubes located inside the fan blades. The experimental results showed very good correlation when compared to the numerically modelled blade surface pressure at various flow rates, even at low flow rates. This was used to validate his numerical model which was used for further flow investigation at low flow rates.

Chapter 3

Periodic three dimensional numerical model

The flow of air through the M-Fan is modelled using a periodic three dimensional numerical model (P3DM). The P3DM separates the domain into rotationally symmetric regions, i.e. only one of the blade region's is modelled, with repeated periodic sides. Louw *et al.* (2012) states that this model could exhibit inaccurate results at low flow rates due to rotating stall patterns near the fan hub not being simulated. This study is only concerned with the fan's designed operating point, which is far from stalling conditions as shown in the work of Wilkinson (2017). The numerical model will be solved using a steady state approach. Louw (2015), Meissner (2018) and Wilkinson (2017) all show that steady state modelling gives accurate results at their respective design operating points.

The blade geometry and computational domain are developed using the ANSYS 17.2 WORKBENCH software packages, unless stated otherwise. The same numerical modelling technique covered in this chapter is used for the numerical modelling of the B2a-fan. These results will be used in chapter 5 when validating model accuracy against experimental data. The current chapter will use the M-Fan as a reference. A nose fairing similar to the B2a-fan is added to the M-Fan model (details in Appendix A.1). This is done to allow smooth flow onto the fan blade and is further explained in section 3.1.2.

3.1 Computational domain

The simulated P3DM is a simplified version of the BS 848 type A test facility, on which the experimental work is performed. As the fan consists of 8 blades, a 1/8th section of the domain (fan) is modelled. This saves on computational resource and assumes that the flow through the rotor flow is periodic. The (45° wedge) domain comprises of three subdomains: the inlet, rotor and outlet subdomain.

The creation of the individual subdomain allows flexible grid resolution based on localized pressure gradients, saving on computational processing where necessary. ANSYS Turbogrid limits the size of the blade domain and cannot create the inlet and outlet domain shapes required for this study. Louw (2015) conducted a sensitivity study on the subdomain for accurate simulation of the B2a-Fan in a BS 848, type A test facility. The same dimensions will also be used in this numerical simulation of the M-Fan as shown in figure 3.1. The subdomains will be discussed in more detail in the following sections.

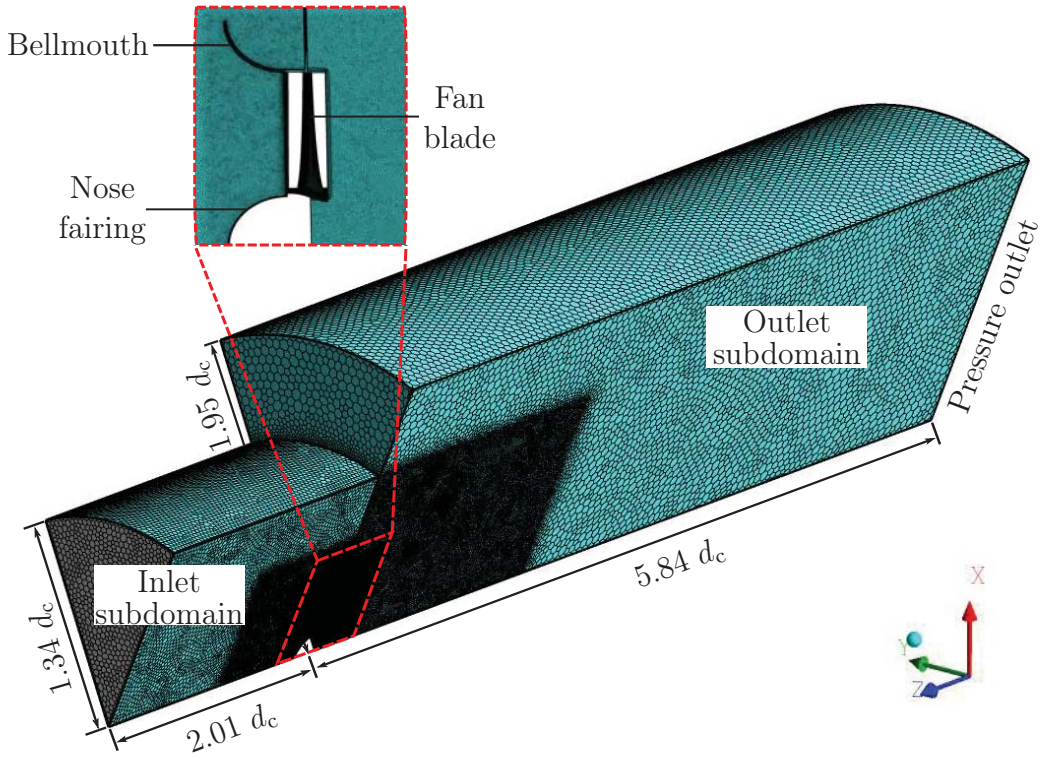

Figure 3.1: Computational domain of the periodic three dimensional numerical model

There are two methods used to model flow in multiple sub domains, namely the single frame of reference (SRF) and multiple frame of reference (MRF) model. The SRF rotates all the domains about one axis at the same rotational speed. Walls that are stationary relative to the reference frame must be rotated individually about the rotational axis. The MRF rotates individual domains at different axis and/or rotational speeds. Each sub domains is then solved by calculating the relative flow in the reference frame specifically chosen for it. A special treatment of the interface between adjacent domains is used in order to have the boundary conditions required by each domain in the proper reference frame.

In the MRF model, the subdomain interfaces can be solved using either the Frozen Rotor model or the Mixing plane model. Both models assume the domains to experience steady state flow. This steady state approach can cause inaccurate modelling when the blade is close to stalling. Unsteady flow appears before the occurrence of definite flow separation on the blade. There is a flow regime in which separations and reattachments occur depending on turbulence or any slight modification of the boundary conditions. This behaviour cannot be captured by steady state calculations. This can occur even if no noticable rotating stall is present and care must be taken when modelling and interpreting results.

The frozen rotor model interfaces the flow between sub domains by translating it from one reference frame to the next, i.e. the flow is not completely mixed and potentially contains non-uniformities across the boundary. The rotational interaction between the upstream and downstream frames (interfaces) is not accounted for. This allows the simulation to be considered as a frozen or still image, where the flow results can be obtained from a specific fan position in space (ANSYS Fluent Inc., 2017).

The mixing plane model is applicable where flow has not reached a uniformity or and is in a completely mixed state between the interfaces. The flow data is circumferentially averaged at the interfaces of the subdomains. Mass or area weighted averaging is done at various radial locations along the interfaces. This result in a more uniform flow profile at the interfaces.

Initial simulations with a static inlet and outlet domain and rotating blade did not result in accurate simulated answers when compared to the experimental data. This observation was also seen in Louw *et al.* (2012). Meissner (2018) also sees these results and puts it down to the mixing plane model having slight mass imbalances between the inlet and outlet subdomains due to the required radial averaging. This is compensated for by imposing a pressure jump across the mixing plane (ANSYS Fluent Inc., 2017). The domain with a multiple moving reference frame results in more accurate simulation results, as seen by

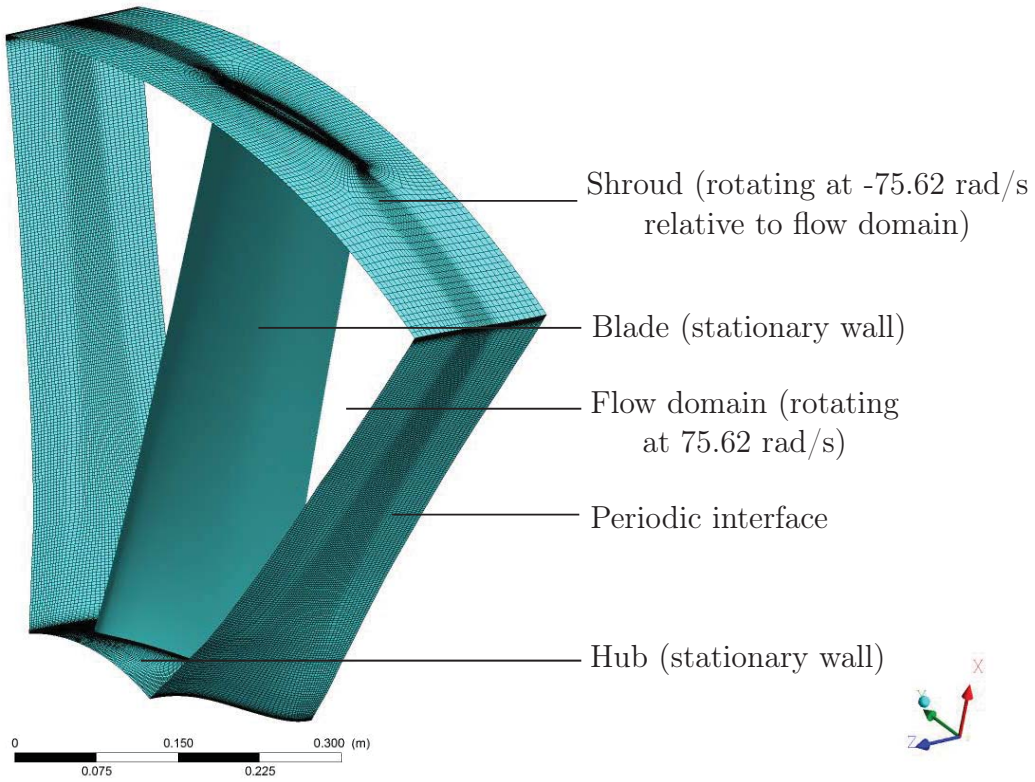

Figure 3.2: Blade subdomain boundary conditions

Louw *et al.* (2012) and Meissner (2018). All sub domains therefore rotate about the positive z axis at 75.61 rad/s in the absolute coordinate system, while the blade remains stationary in the absolute reference system. The interfaces are calculated using the frozen rotor approach.

3.1.1 Blade subdomain

The blade domain models the annular section of the shroud of the BS 848 test facility between the inlet and outlet subdomain. A no-slip boundary condition is set for the fan blade, hub and shroud. The fluid inside the domain rotates at 75.61 rad/s around the z-axis. The wall boundaries of the hub and the blade rotate along with the domain i.e. 0 rad/s relative to the fluid domain (stationary wall). The frozen rotor reference frame requires that the shroud moves in the opposite direction relative to the flow at -75.61 rad/s. The upstream, downstream and periodic radial sections are set as interfaces, the joining of which will be explained in section 3.2.

The Computer Aided Design (CAD) model of the blade is constructed in

Autodesk Inventor Professional 2018. The various points of each individual blade profile, obtained from Wilkinson *et al.* (2018) are stacked radially along the blade. The points are imported and joined where appropriate. The blade profiles are then lofted, extended and finally the blade is sculpted to produce a blade which is used in the P3DM. The blade is exported as a .stp file and imported into ANSYS Design Modeller.

ANSYS Turbogrid is used to create the blade mesh. Individual meshing layers (approx. 15) are created along the span of the blade. The Automatic Topology and Meshing feature (ATM) is used to create control points along the blade profiles. The topologies are then automatically expanded into an optimal mesh upstream and downstream of the blade. More detailed information about the various topology types incorporated by the ATM meshes can be found in ANSYS Fluent Inc. (2017).

The element size next to the blade surface was chosen to accommodate the various turbulence models. An expansion rate allows the cells to accommodate the higher pressure gradients at the blade and transition into a slightly coarser mesh where the gradients are smaller and flow more uniform.

The result is a domain with a structured mesh in which a smooth transition from the blade profile contour to the outer mesh parts is created. The mesh cells are aligned with the radial direction of the flow field around the blade. The blade tip gap (0.003 m) is separated into 40 even radial sections allowing for sufficient detail to take in the effect of blade tip clearance.

3.1.2 Inlet and outlet subdomain

The inlet subdomain models the settling chamber of the BS 848 test facility. The domain connects with the blade subdomain and was constructed in ANSYS Design Modeller. It includes the inlet bellmouth and nose fairing of the fan. A mass flow inlet at the inlet allows a uniform inlet velocity profile along the negative z direction to enter the domain. The bellmouth and fan nose fairing are assigned with a no-slip condition boundary condition and are stationary relative to the rest of the domain. The top of the inlet domain is a zero shear wall, as this only serves as a conduit to channel the air flow into the fan.

An unstructured polyhedral mesh is constructed for the inlet domain using ANSYS Mesher. This requires a tetrahedral mesh to be generated in Design Mesher and then to be converted in FLUENT, as ANSYS Mesher cannot convert directly to polyhedral mesh. The main advantage of the polyhedral mesh is that it provides similar accuracy to hexahedral mesh at half the number of

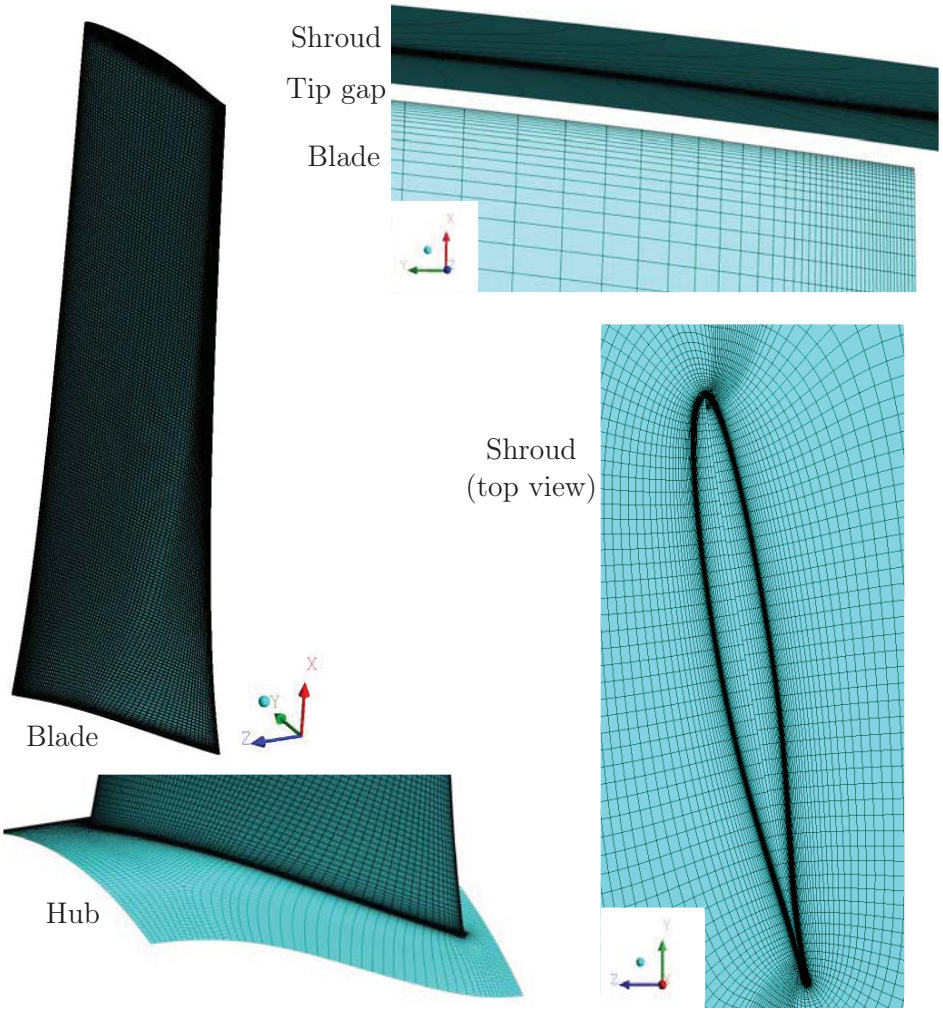

Figure 3.3: Blade subdomain mesh structure

cells, saving on computation power but providing the same amount of resolution detail (Lanzafame *et al.*, 2013). Grids along the wall boundaries requiring more detail (y^+ value) use structured prism layers. This was also seen to improve mesh orthogonality and skewness.

The polyhedral mesh transitions from a coarse resolution at the inlet to a more fine resolution at the blade inlet subdomain. This is to accommodate the low pressure gradients at the inlet and higher pressure (velocity) gradients as the flow moves closer to the blade subdomain. The exiting interface has a mesh approximately twice as refined at the blade subdomain interface. This allows good interpolation from the upstream to the downstream blade domain interface.

The outlet subdomain is modelled to be open to the atmosphere, allowing air

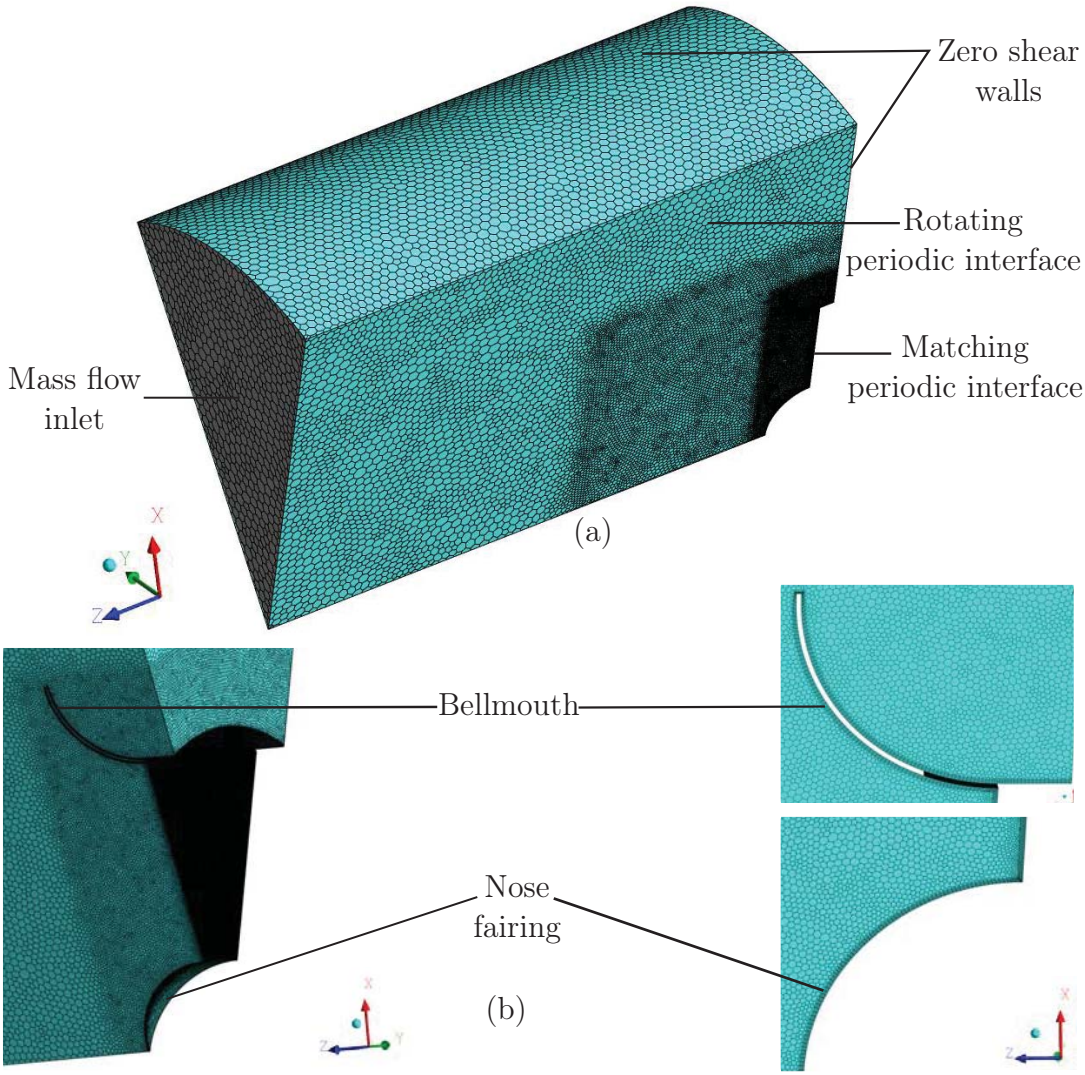

Figure 3.4: Inlet subdomain (a) boundary conditions and (b) mesh structure

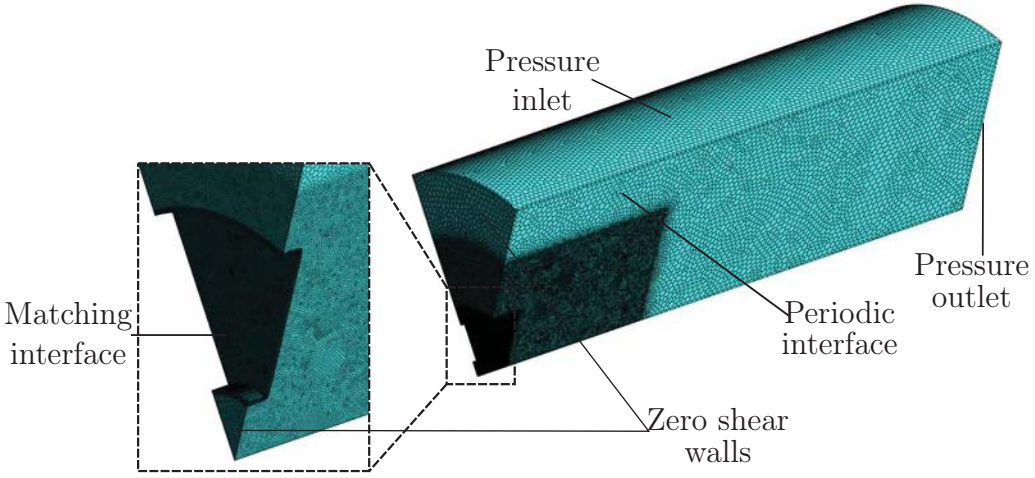

Figure 3.5: Outlet subdomain boundary conditions and mesh structure

to move freely after the blade subdomain. A pressure outlet with a gauge pressure of 0 Pa is specified at the downstream side of the outlet domain. A pressure inlet is specified at the top of the outlet domain. Louw *et al.* (2012) found that at high flow rates, flow enters the top of the domain. A pressure inlet allows the solution to converge faster due to less potential backflow at the top of the domain. A polyhedral approach similar to the inlet subdomain is used. The mesh resolution is as fine as the upstream blade domain. This then becomes coarser along the direction of the airflow.

3.2 Domain assembly

Each subdomain is imported into ANSYS Fluent where they need to be joined together. Each subdomain needs to have its periodic boundary (interface) paired with its partner boundary. A periodic repeat mesh interface allows the rotating flow to exit the periodic boundary and re-enter into the matching periodic boundary of the subdomain.

The blade subdomain has a tangential offset from the inlet and outlet subdomain. As a result, there are non-touching interfaces which do not align. This is inherent to ANSYS Turbogrid, as it creates its own trapezoidal domain shape and position according to the blade profile and flow conditions. A periodic repeat mesh interface combines the offset (overlapping) interface of the inlet and outlet subdomains with the blade subdomain. This can be done due to the rotationally symmetric nature of the computational domain. Alternatively put, the flow across the non-touching boundaries (overhanging interfaces) is accounted for by adding it to the other missing side on the other piece of the

interface so that the domain is rotationally symmetric.

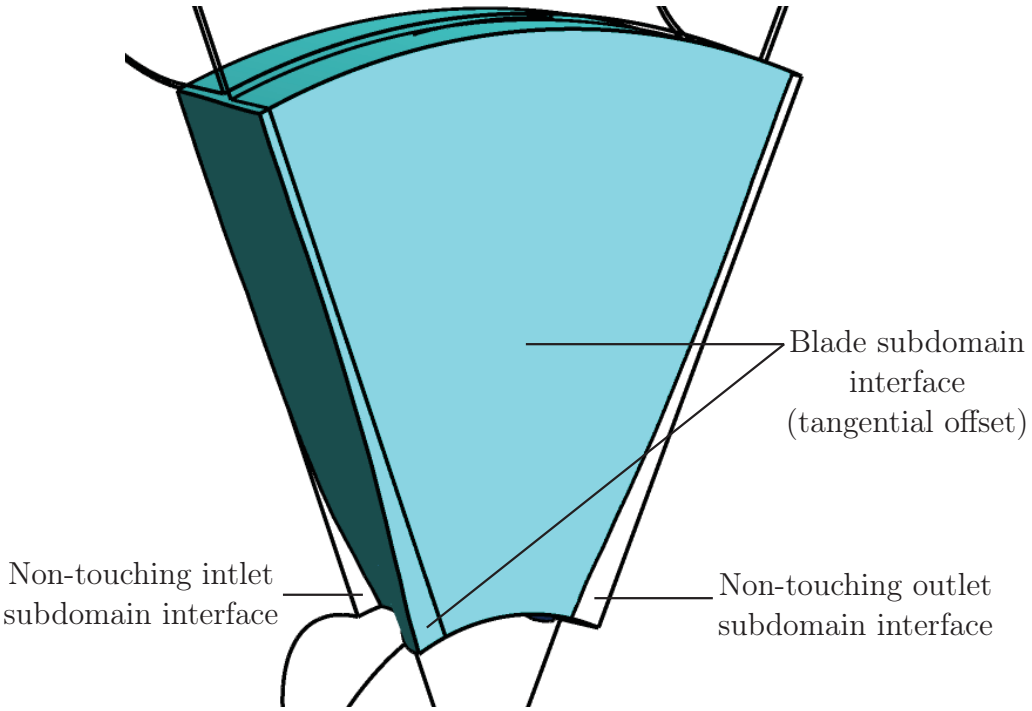

Figure 3.7: Tangential offset of the blade subdomain interfaces

The mesh interfaces between the inlet, blade and outlet domains each have their individual meshing scheme and density. To successfully combine these

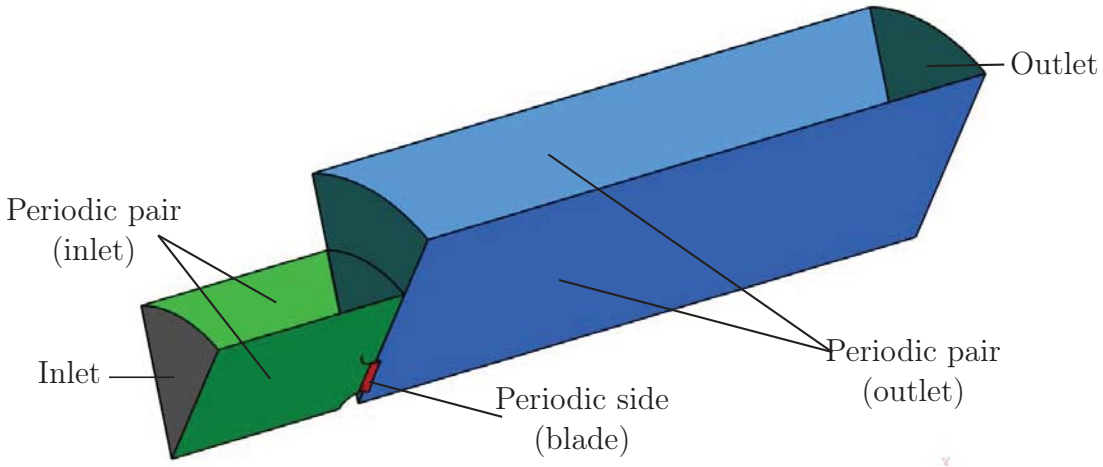

Figure 3.6: Periodic boundary pair in numerical model

non-conformal interfaces, a new periodic repeat mesh interface is created by using a virtual polygon approach (ANSYS Fluent Inc., 2017). This places new nodes on a new interface and uses them to allow a smooth transition of the variables through the sub-domain interfaces. It was ensured that the upstream nodes are always the same or more fine than the downstream nodes, allowing for easier interpolation and reducing numerical inaccuracies.

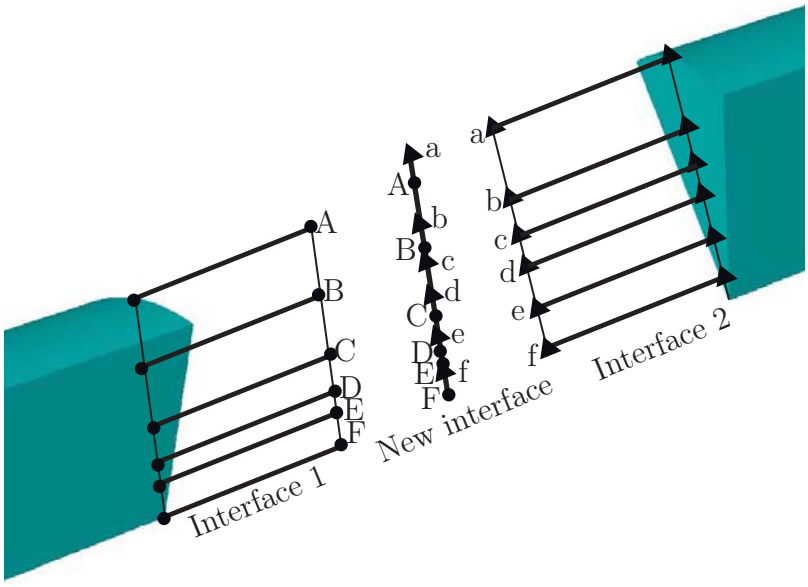

Figure 3.8: Example of two dimensional interpolation at the matching subdomain interfaces

3.3 Turbulence modelling

Turbulence modelling is performed using the realizable k-ε turbulence model of Shih *et al.* (1995), further detailed in Appendix B.2. Shih *et al.* (1995) states that the model shows significant improvement over the standard k-ε turbulence model of Launder and Spalding (1974). ANSYS Fluent Inc. (2017) states that the realizable model provides the best performance of all the k-ε models when seperated flows with secondary flow features are encountered.

The realizable k-ε model with enhanced wall function is used to model the M-Fan while the standard wall function is used to model the B2-a fan. The turbulence intesity is set to 2 % with a length sacle of 0.01 m. The reason for the different wall functions is due to the finer mesh created for the M-fan blade in ANSYS turbogrid.

The higher blade twist of the M-fan blade requires a very fine mesh (higher mesh density), especially close to the trailing edge of the blade tip . This is to ensure that the meshing cells are of a high quality (proportion), i.e. an acceptable aspect ratio, orthogonal quality and skewness. The small cells at the wall, necessitates the need for the enhanced wall function, which can model cells with a minimum y^+ value of 1 and maximum of approximately 300. Details of the enhanced and standard wall functions are provided in Appendix B.3. Augustyn (2013) showed good results when using the enhanced wall function to model the B2-fan. Even though the finer mesh is more computationally expensive, it results in more stable solution due to the higher quality cells along the fan blade wall.

The k-ε model with standard wall function is more economical (less computationally expensive) than the enhanced wall function while still achieving a high modelling accuracy. Louw *et al.* (2012) and Meissner (2018) make use of the Realizable k-ε model with standard wall function on the B2a-fan. The model compared well with their experimental results for the B2a-fan. The model can be used on the B2a-fan, as it does not require such fine cells close to the fan blade wall. The model with standard wall function requires a y^+ value between 30 and 300 for it most accurate solution.

3.4 Solver settings

The solver settings and discretization schemes are shown in table 3.1. Louw (2015) and Meissner (2018) both use the same settings which resulted in accurate numerical modelling. These will briefly be discussed in this section.

Table 3.1: Numerical model solver settings

Pressure-velocity coupling	SIMPLE
Discretization scheme (Gradient)	Least Squares Cell Based
Discretization scheme (Pressure)	PRESTO!
Discretization scheme (Momentum)	QUICK
Turbulent kinetic energy	QUICK
Turbulent dissipation rate	QUICK

The numerical model assumes incompressible flow, which warrants the use of the pressure coupled solver over the density based solver. Mass conservation is achieved through the *SIMPLE* pressure-velocity coupling algorithm. The *Least squares cell based* discretization scheme uses a weighting factor to calculate the gradients of the solution variables. It is less computationally

expensive than the node-based gradient scheme and provides fair accuracy for skewed and distorted cells (ANSYS Fluent Inc., 2017). The *PRESTO!* pressure discretization scheme is chosen as it is suited for high pressure gradients and swirl (Versteeg and Malalasekera, 2007).

The *First order upwind* momentum and turbulence discetization schemes are initially run until satisfactory convergence was reached. This allows the most numerically stable schemes to initially calculate a solution. They are then changed to the *QUICK* discetization schemes as they have a higher accuracy scheme for cells which are aligned in the flow direction (ANSYS Fluent Inc., 2017). It should be noted that ANSYS FLUENT resorts to *Second order upwind* discretization schemes for unstructured meshed (ANSYS Fluent Inc., 2017).

The convergence of the solution is monitored by three criteria: mass continuity, inlet and outlet pressure fluctuation and solution residuals. The convergence criteria for the residuals is set at 10^{-12}. The residuals are very low as to allow the solution to run until the outlet pressure has converged to the user's satisfaction (independent of residuals). The solution was monitored until convergent total outlet pressure was observed.

A detailed study of the mesh density of each individual subdomain is conducted (see Appendix B.4). The mesh densities of each individual subdomain of the M-Fan are shown in table 3.2.

Table 3.2: Subdomain mesh densities of the M-Fan

Subdomain	**No. of elements**
Inlet	1596661
Blade (3 mm tip gap)	2298388
Blade tip gap (layers)	40
Outlet	1659736

3.5 Summary

The M-fan is numerically simulated by making use of a periodic three dimensional numerical model. It consists of three subdomains each with their respective boundary conditions. A steady state approach is used to solve the solution using the realizable k-ε turbulence model with enhanced wall function. To verify the numerical method an experimental setup is constructed and is detailed in the following chapter.

Chapter 4

Experimental testing

The performance characteristics of the M-Fan are determined experimentally using the BS 848 (ISO 5801) testing standards. This provides data on the global flow performance of the axial flow fan. Further blade surface pressure measurements are conducted to obtain experimental data on localized pressure distribution across the fan blade. Both experimental techniques will be discussed in this chapter. The experimental results provide data for comparison with the numerical model and analysis of the M-Fan performance, discussed in chapter 5.

The experimental M-fan has a 2 mm thick stainless steel circular hub located approximately half way between the blade leading and trailing edge, details of which are shown in Appendix A.1. This models the full scale M-Fan installed at the ACC test facility at Stellenbosch University. The plate hub also provides secure mounting for the wireless transmitters.

Experimental techniques to measure fan performance have been discussed in the literature study. Of these, BSPM is the only technique which does not need to take spacial effects into account as only the the static pressure on the blade is measured. A high level of certainty exists in the measured values as shown in the work of Louw *et al.* (2012). The experimental technique can be scaled up to conduct BSPM on larger diameter fans and sets a foundation for conducting performance tests on the full scale M-fan ($d_c = 7.12$ m).

Louw *et al.* (2012) conducted BSPM on the B2a-fan. The experimental results compared well with their numerical model. The same experimental tests are conducted on the B2a fan to verify the experimental method and data processing required for BSPM analysis. Once satisfactory BSPM results are achieved, the same experimental method and data processing is applied to the M-Fan.

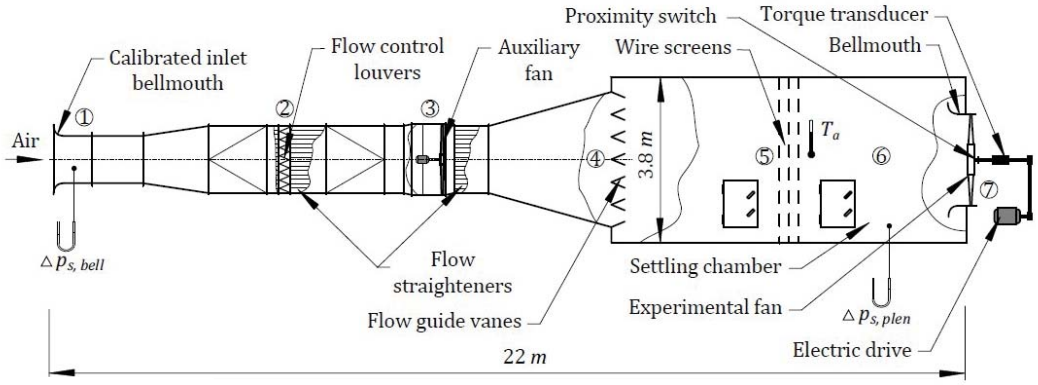

(a)

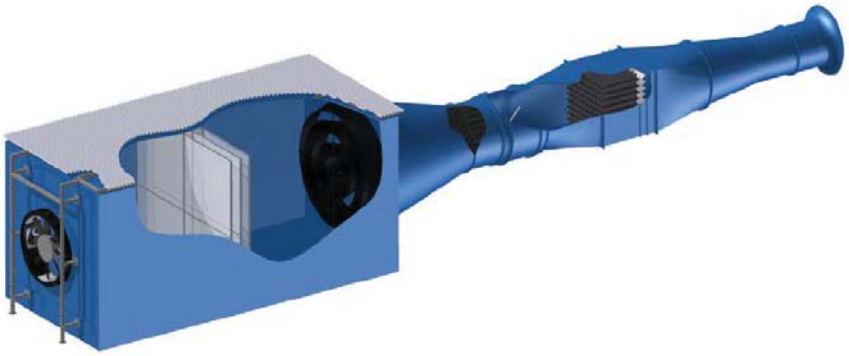

(b)

Figure 4.1: (a) Side view and (b) isometric view (excluding motor assembly) of the BS 848, type A fan test facility located at University of Stellenbosch (Louw, 2015)

4.1 Standard performance testing

The characteristic fan curves consist of the fan total to static pressure difference (p_{Fs}), the fan shaft power (P_{F}) and total to static efficiency (η_{ts}). These parameters are measured relative to the respective volume flow rate passing through the fan ($\dot{V}$). Experimental tests are conducted on a BS 848, type A (open-inlet and open-outlet) fan test facility at the Stellenbosch University shown in fig 4.1. Further information regarding the design and commissioning of the test facility can be found in Venter (1990).

4.2 Fan test facility

A description of the fan test facility's main components is shown below and corresponds to the numbered sections in fig 4.1.

1. Air flow is drawn through a calibrated inlet bellmouth, where static pressure is measured relative to the atmospheric pressure. There are 4 taps located around the bellmouth which all join into one common bellmouth pressure line ($\Delta p_{\mathrm{s,bell}}$).

2. Air flow through the test facility is controlled (throttled) by a set of louvres. Flow straighteners are located before and after the louvers.

3. An axial flow booster fan (7.5 kW) is operated to overcome mechanical flow losses in the test facility. A second set of flow straighteners is located after the booster fan.

4. Guide vanes allow a relatively even flow distribution into the settling (plenum) chamber. The settling chamber (4 m $\times$ 4 m $\times$ 7 m) allows for a low flow velocity, so that the dynamic effect of the air can be neglected (specific to type A test facility). The BS 848 standards (2007) state this as being lower than 2 m/s so that the fan can be considered to have an "open" inlet.

5. A set of three wire screens are situated inside the settling chamber to allow a uniform velocity profile entering the fan. Two pressure measuring points are located inside the plenum chamber, which join into a common plenum pressure line ($\Delta p_{\mathrm{s,plen}}$). A temperature gauge is also located inside the plenum chamber (T_{a}).

6. The test fan is located inside a shroud which is connected to a bellmouth ($d_{\mathrm{bell}} = 1.543$ m). A coupling is located between the fan shaft and the drive shaft.

7. A variable speed drive (VSD) controls the speed of a 10 kW motor. The motor uses a pulley to turn to the drive shaft. The torque transducer is positioned between the drive shaft and the fan shaft. The shaft speed (N_{F}) and torque (T_{F}) are recorded.

4.2.1 Measuring equipment and data logging

The ambient pressure (p_{atm}) is measured with a mercury barometer situated nearby the test facility. The temperature inside the settling chamber (T_{a}) is

measured by a mercury thermometer. Two HBM PD1 pressure transducers are used to measure the static pressure at the inlet bellmouth ($\Delta\ p_{s,bell}$) and settling chamber pressure ($\Delta\ p_{s,plen}$) relative to the atmospheric pressure. The fan shaft torque is measured by a HBM T22 torque transducer. The rotational speed (N_F) is measured by a proximity sensor mounted adjacent to the shaft and connected to a frequency to voltage converter. The measuring devices send a 0-10 V signal to a HBM PMX data acquisitioning system. This is connected to a computer which uses CATMAN Software for data recording. Figure 4.2 shows a line diagram of the measuring equipment while table 4.1 details the measuring equipment along with the maximum relative standard deviation between the calibration sets. Details of the calibration of each measurement device can be found in Appendix C.2.

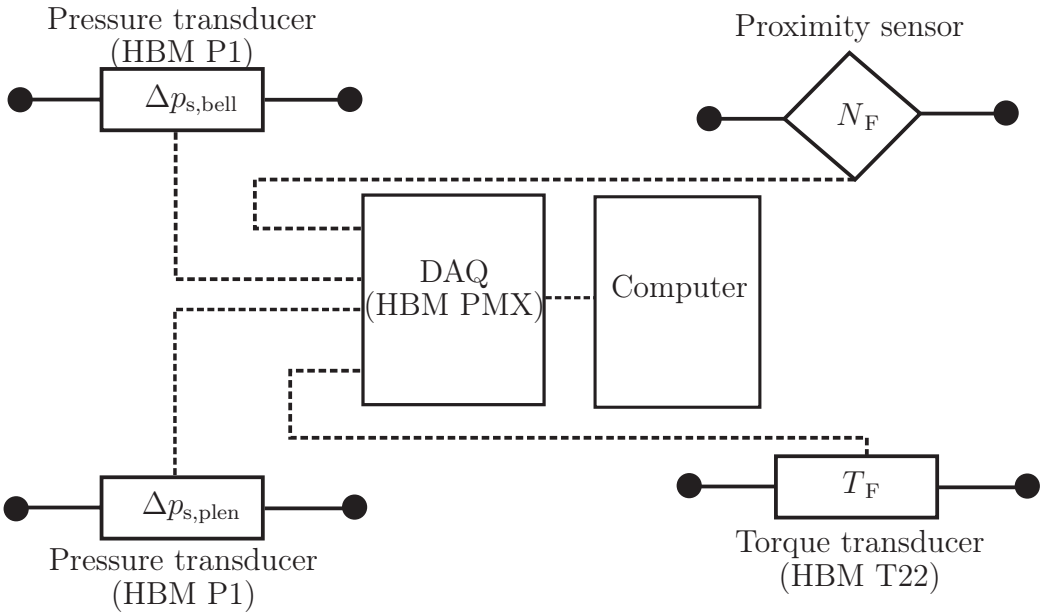

Figure 4.2: Line diagram of the measuring instrumentation at the BS 848 type A test facility

Table 4.1: BS 848 fan test facility measuring instrumentation and accuracy

Channel	**Range**	**Relative standard deviation (max.)**
Bellmouth ($\Delta\ p_{s,bell}$)	1000 Pa	±1.9 %
Settling chamber ($\Delta\ p_{s,plen}$)	1000 Pa	±2.1 %
Shaft torque (T_F)	100 Nm	±1.3 %
Rotational speed (N_F)	-	-
Temperature (T_a)	-	0.5 °C
Atmospheric pressure (p_{atm})	-	0.005 mm Hg

4.2.2 Experimental procedure

The blade stagger angle of the fan is measured at the blade hub uing a digital protractor (accuracy $\pm 1^{\circ}$) before installation of the fan onto the driving shaft. The fan tip gap is measured before each test set. This is done by measuring the distance between the fan hub and fan blade tip using a using a Vernier calliper. The concentricity of the fan shaft in relation to the shroud is adjusted by a set of turnbuckles. The bellmouth static pressure is sensitive to wind and all tests were conducted in wind free conditions. Once the above conditions are satisfied, a typical test run can be conducted in the following steps:

1. Run the fan for 5 minutes at design speed before any measurements are taken. It was found that the torque transducer needs some time to warm up before the readings would settle. This was also observed by le Roux (2010). The fan is then briefly stopped for the next step.
2. Record zero readings of all the channels while the fan is not rotating. The atmospheric pressure and temperature inside the plenum chamber must also be recorded at the start of the run.
3. Run the fan up to its design operating speed (722.1 rpm) using the VSD and set the flow louvres to their desired (start) position. The auxiliary fan is to be run at high fan volume flow rates close to the design flow rate and higher
4. The data is recorded for 15 seconds at a sampling rate of 100 Hz.
5. Adjust the louvres to record a new fan volumetric flow rate and pressure rise. This step is repeated until all the desired flow rates (fan operating points) are recorded.
6. End the test procedure by stopping the fan. Record the zero measurement for all channels as well as the plenum temperature and ambient pressure.

The recorded data is then processed as explained in Appendix C.3 in order to obtain the fan static pressure and static efficiency required for the characteristic performance curves.

4.3 Blade surface pressure measurement

Experimental test are conducted to measure the static pressure at selected points along the M-Fan (BSPM). Figure 4.3 shows the main components of the experimental setup. Two specially manufactured M-Fan blades have pressure taps on their surfaces. The pressure is transferred along tubes inside the blade to a module housing pressure sensors. This is then wirelessly transferred to a personal computer (PC) and the data processed for analysis. All experiments were conducted in the BS 848, type A fan test facility previously discussed in Section 4.2. The apparatus, test procedure, data recording and analysis required for BSPM are discussed in more detail.

4.3.1 BSPM blade

A technique that is similar to the method used to construct the BSPM blades of Louw (2015) is used, of which a summary is provided in Appendix A.3. The slight variation in blade manufacturing is intended to provide a basis for manufacturing BSPM blades for the large scale M-Fan. Even though it is not

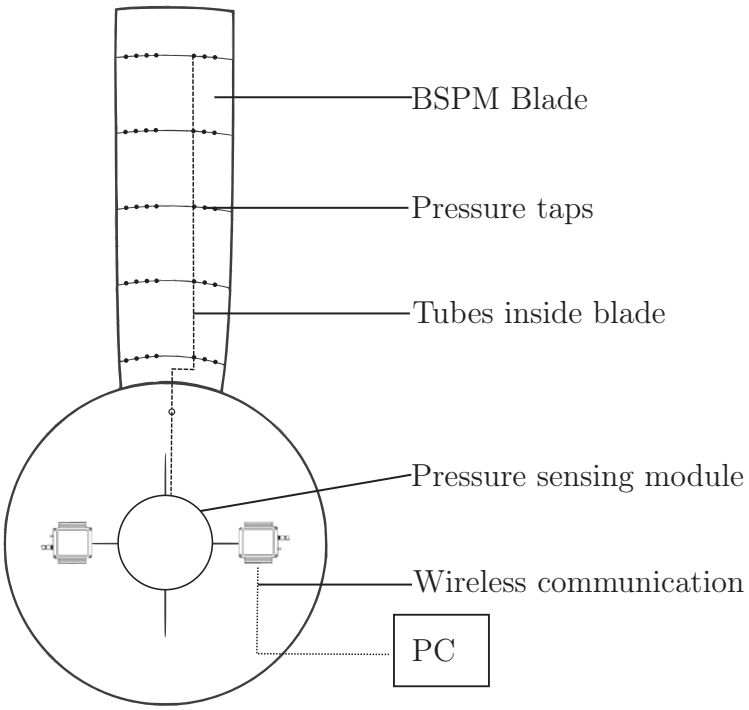

Figure 4.3: Main flow components and apparatus for blade surface pressure measurement

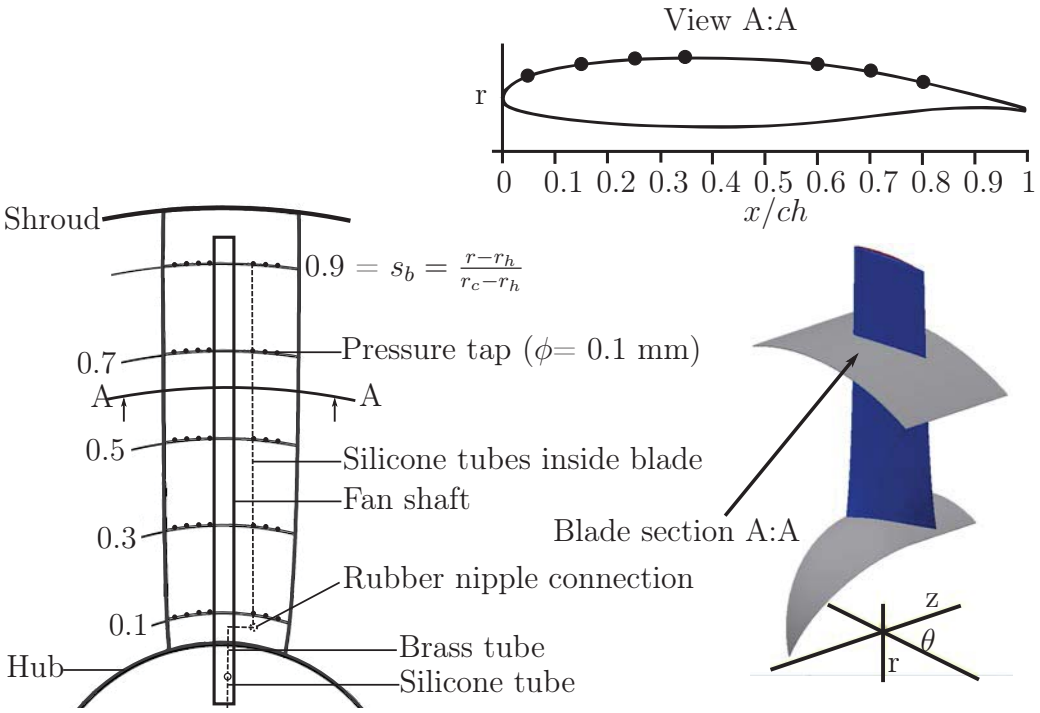

Figure 4.4: Schematic of BSPM blade and pressure tap locations

evident in the M-Fan (small scale), the difference in manufacturing method used in this thesis should be cheaper and result in a lighter blade construction for the full scale BSPM M-fan blades, compared to the method of Louw (2015).

Wilkinson *et al.* (2018) successfully conducted characteristic performance tests of the M-Fan in the BS 848, type A test facility. The M-Fan blades were manufactured using a carbon fibre hand layup. The same blade moulds and manufacturing technique is used to construct additional blades for the purpose of BSPM. A schematic of a BSPM blade is shown in the figure 4.4. More details on the manufacturing of the M-Fan blade skins can be found in Appendix A.2

Two manufacturing methods were tested, with the final one presented in this section while the other one is detailed in Appendix A.2.2. The initial manufacturing method resulted in catastrophic failure, which is detailed in Appendix A.2.3. This required six new M-fan blades to be manufactured along with the special BSPM blades. There were some complications during testing of the final M-fan BSPM blade and slight modifications had to be made to accommodate these complications, which will be explained in this section.

A single blade has sufficient space to accommodate the inside tap channels for either the suction or pressure blade measurements, necessitating the use of two blades. One blade has pressure taps on the suction side and the other

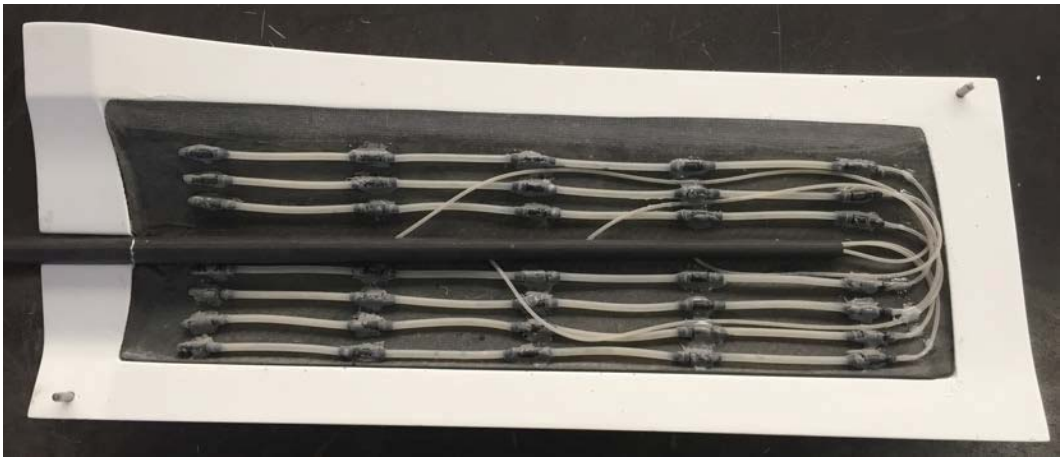

Figure 4.5: Tap location on the inside of the blade skin

blade has pressure taps on the pressure side. Each BSPM blade has thirty-five pressure taps of 1 mm diameter. The pressure taps are located using plastic t-pieces which are connected to silicone tubes inside the blade. These lead the pressurised air through the fan shaft and connect to the pressure measurement module with a brass connector onto silicone tubes.

Thicker silicone tubes are used for the inside of the blade while thinner silicone tubes needed to be used to accommodate the small area inside the blade shaft. The thinner silicone tubes are inserted along different tube locations (lengths) in order to retain the blade shaft's structural integrity inside the blade.

The seven pressure taps are located radially along a curved blade profile at five proportional blade span lengths (s_b) of 0.1, 0.3 ,0.5, 0.7, 0.9. This provides an even distribution of pressure measurements along the blade span. Each individual pressure tap profile has pressure taps located at dimensionless chord lengths (x/ch) of 0.05, 0.15, 0.25, 0.35, 0.6, 0.7, 0.8, where 0 is the leading edge and 1 the trailing edge of the blade. The placement of the taps closest to the leading and trailing edge is constrained by the thickness of the blade.

A paper print out of the blade surface with the pressure tap locations is used to locate the pressure tap holes onto the carbon fibre blade surface. Pressure tap holes are drilled through the blade skin. The plastic t-pieces and silicone tubes are glued to each pressure tap and allowed to set. The locations of the t-pieces with their silicone tubes on the inside of the blade skin are shown in figure 4.5.

During the first test run of the BSPM fan, the small silicone tubes inside the blade shaft became entangled/ kinked. This caused the pressure measuring channels to be blocked. The blockage was limited to only the small silicone

tubes connecting to the BSPM module and not the larger tubes inside the blade channel. This method would therefore have been more successful if the silicone tubes leading from the blade channel (through the fan shaft) onto the pressure module were thicker and more robust.

A small area on the non pressure tap side of each BSPM blade skin was consequently cut open. This allowed drilling directly from the fan root and into the first tap location (t-piece). A plastic tube was then inserted into the T-piece as shown in figure 4.6. The open area (flap) was closed with an epoxy based glue and sanded down for a smooth surface finish. The final modification is shown in figure 4.6. The channel at chord location $x/ch = 0.35$ could not be drilled open because of its close proximity to the blade shaft.

A vacuum test (-3000 Pa) was conducted on the fan blades to test whether the channels are all air tight after the manufacture. A Betz manometer was attached to a respective channel tube and then tested for 10 min and a maximum tolerance of 3 Pa was allowed. The experimental tests was run for a max time of 5 min. All channels were air right, except for the pressure side channels at a chord length of $x/ch = 0.15$ and $x/ch = 0.25$ along the length of the blade (ten pressure tap locations). This final BSPM blades allow for a maximum of fifty pressure taps to be measured during experimental testing.

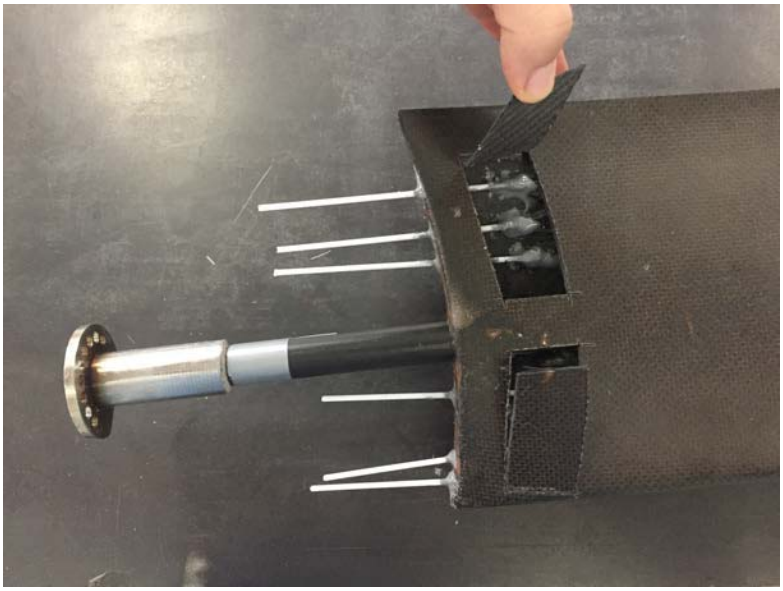

(a)

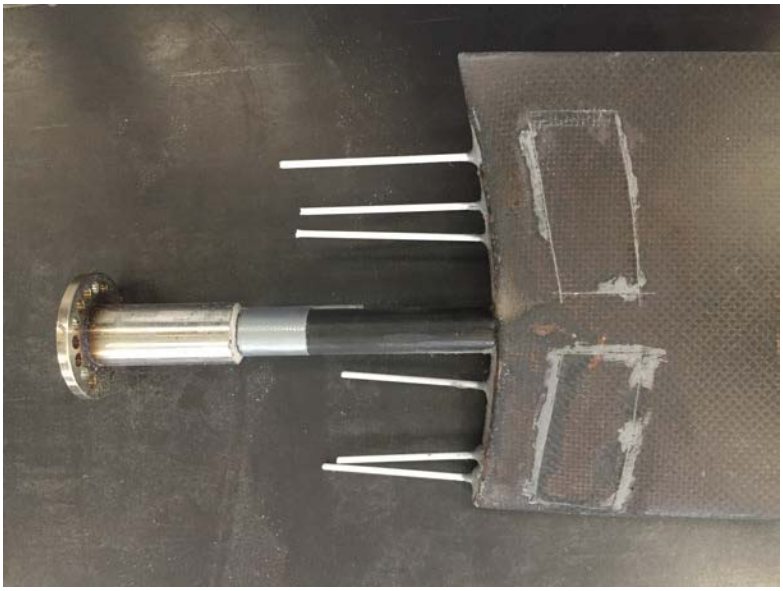

(b)

Figure 4.6: (a) Open blade skin flap for location of platic tube into T-piece and (b) closed blade skin flap

4.3.2 Pressure sensing module

The pressure sensing module measures the pressure from the blade surface pressure tap lines. It is located upstream of the fan onto the fan shaft. An aluminium module houses seven piezo-resistive pressure transducers (Freescale MPX 2010), allowing the measurement of all the pressure taps across one blade span. The module was developed by Louw (2012) who used it for his BSPM experimental setup.

The Freescale MPX 2010 pressure transducers measure the differential pressure across its two ports (Δp_{m}). The one port is connected to the blade pressure tap and will be referred to as the tap side. The other port serves as a reference pressure and will be referred to as the reference side. All transducer

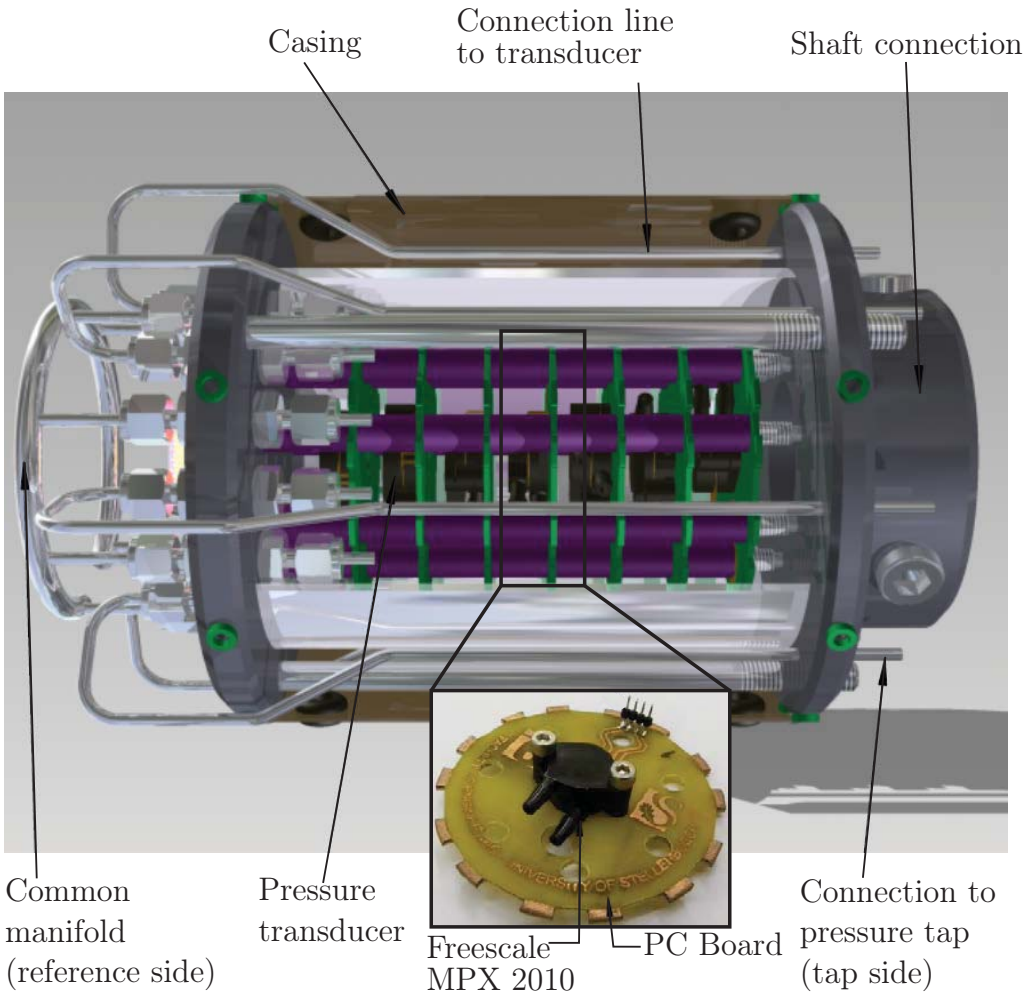

Figure 4.7: BSPM module (adapted from Louw (2015))

reference ports are connected to a common manifold. This is connected to a 2 m long stainless steel rod rotating inside bearings. The rod is located upstream of the fan inside the test facility's settling chamber. Louw (2015) found that this is required to accurately measure the settling chamber pressure, as it mitigates the effect of any rotationally induced pressure difference. The measurements are therefore referenced to the total pressure inside the plenum chamber ($\Delta p_{\mathrm{t,plen}}$).

Each transducer is mounted on a PC board, with its circuit connected to a D-sub plug. The transducers (and their membranes) are mounted parallel to the fan shaft to minimize centrifugal effects during rotation. The calibration, measurement accuracy as well as the potential centrifugal offset due to rotation is shown in Appendix C.4. The datasheet does not indicate an accuracy rating, however a maximum error of 2.7 % between all of the transducers (and all calibration sets) was measured against a Betz manometer.

4.3.3 Recording and telemetry equipment

Telemetry equipment from LORD MicroStrain is used to wirelessly transfer the measured pressure transducer readings. The D-Sub plugs from the module connect to two LORD Microstrain V-Links, which are fixed on the fan hub during fan rotation. The V-Links provide a 3 V excitation to the pressure transducers, amplify the tranducer's measured signal and transmit this to the LORD Microstrain WSDA-Base-101. The base station is connected to the computer and live readings are recorded using Node Commander® v 2.17.0. The V-links are set at a sampling rate of 512 kHz. Error and repeatability studies of the experimental data is shown in Appendix C.5.2.

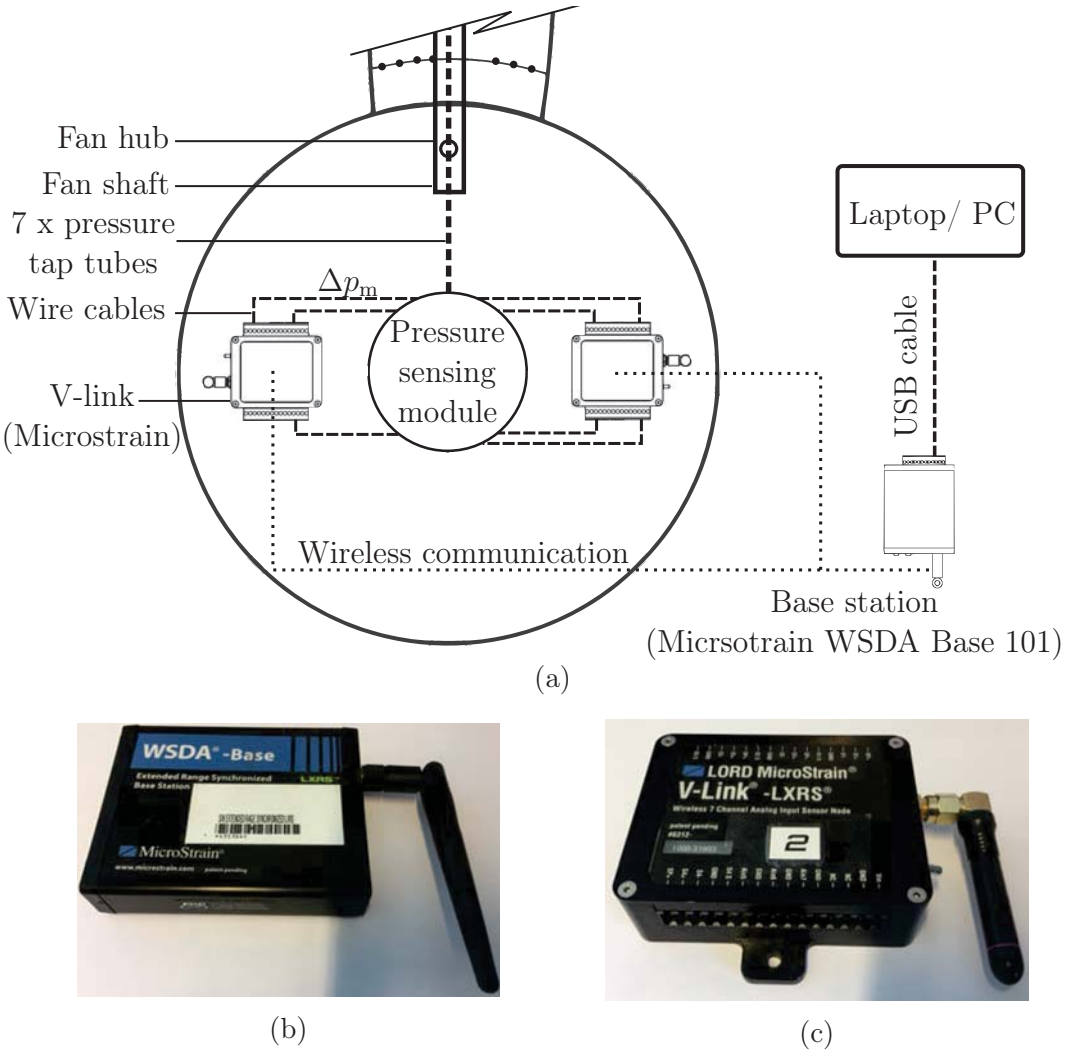

(a)

(b)

(c)

Figure 4.8: (a) Schematic of the BSPM telemetry along with its (b) base station and (c) V-Link

4.3.4 Test procedure and data processing

The fan characteristic measurements are required for final BSPM data processing, specifically to obtain the plenum pressure ($\Delta p_{t,plen}$). The measurement procedure in section 4.2.2 is run simultaneously with the pressure tap measurements. The D-sub plugs are connected to the V-links and the BSPM procedure conducted according to the following steps:

1. Cover all the blade pressure taps with translucent tape, except for the

taps which are being tested at their respective blade span. Make sure that the blade surface is clean and smooth at all times.

2. Record a zero pressure reading (Δp_{zero1}) of the pressure transducers.
3. Run the fan up to its design operating speed.
4. BSPM of the design operating point is required for this thesis. The louvres are therefore adjusted for measurements above and below the fan design operating point volume flow rate. This requires the operation of the booster fan.
5. Record the pressure at the blade taps (Δp_{m}) for 15 seconds (live recording).
6. After the second louvre setting is recorded, turn off the fan and conduct another zero measurement (Δp_{zero2}).
7. Cover the tested pressure taps with translucent tape, remove translucent tape from another blade span and repeat steps 2 to 6 for new BSPM recordings. The test is complete once BSPM measurements are recorded along all the blade spans of the blade suction and pressure side.

Once the experimental testing is complete, the tap measurements need to be processed. As mentioned, the centrifugal offset of the transducer membrane needs to be accounted for. The channels (air columns) inside the blade also experience a centrifugal (radial) loading during rotation. This results in an additional suction pressure being measured by the pressure transducers. Both offsets are accounted for by the following equation (derivation shown in Appendix C.5) for the actual pressure at the blade tap:

$$p_{\text{s,tap}} = e^{\omega^2 {r_{\text{tap}}}^2/2\text{R}T_{\text{a}}}[\Delta p_{\text{m}} + p_{\text{t,plen}} + p_{\text{atm}} - \Delta p_{\text{zero}}] - p_{\text{atm}} \tag{4.1}$$

Where is the ω is the fan rotational speed, r_{tap} is the radius of the tap location, R is the specific gas constant, T_{a} is the temperature inside the plenum chamber, p_{atm} the atmospheric pressure and the other pressures as defined in previous sections.

The static pressures at the design flow rate are calculated by linear interpolation. Linear interpolation is justified by the smooth, relatively linear decrease in static pressure vs volumetric flow rate, as will be shown in the following section in figure (5.7).

4.4 Summary

In this chapter, the experimental setup and method to perform the characteristic performance tests and blade surface pressure measurements on the M-fan has been detailed. All tests are conducted in the BS 848 type A, test facility at Stellenbosch University. The test facility along with its measuring equipment and experimental procedure have been detailed. The experimental setup and components to conduct BSPM, namely the blade, pressure module and measuring equipment have been described. Some alterations had to be conducted on the M-fan BSPM blade and a maximum of fifty pressure taps are available for testing. The following chapter shows the results of the experimental work and numerical simulation.

Chapter 5

Results

The results of the numerical simulation and experimental tests are shown and discussed in this chapter. The numerical simulation (P3DM) and experimental tests conducted on the B2a-fan are compared to literature. Once the results are shown to be satisfactory, a similar technique is applied to the M-Fan and results discussed thereafter. A statistical analysis is conducted where applicable. Definitions of the statistical analysis are shown in Appendix C.1.

5.1 B2a-fan results

Louw (2015) presented the performance of the B2a-fan in a dimensionless form. The B2a-fan data from the present study is therefore presented in the same form to facilitate a direct comparison between the data sets. The fan static pressure (Δp_{FS}) is defined by the following dimensionless static pressure coefficient:

$$\Psi_{Fs} = \frac{\Delta p_{FS}}{0.5\rho {u_c}^2} \tag{5.1}$$

where u_c is the circumferential speed at the blade tip, defined by:

$$u_c = \omega r = \frac{2\pi}{60} N r_{tip} \tag{5.2}$$

The flow coefficient is used to account for the volumetric flow rate ($\dot{V}$) in dimensionless form according to the following expressions:

$$\phi = \frac{c_{z,avg}}{u_c} \tag{5.3}$$

where $c_{\mathrm{z,avg}}$ is the axial flow velocity through the fan annulus area (A_{F}), as defined below.

$$c_{\mathrm{z,avg}} = \frac{\dot{V}}{A_{\mathrm{F}}} \tag{5.4}$$

The true pressure measured for the BSPM is defined by a dimensionless static pressure coefficient (C_p) as follows:

$$C_{\mathrm{p}} = \frac{p_{\mathrm{s}}}{0.5\rho_{\mathrm{atm}}u_t^2} \tag{5.5}$$

where u_t is the a tangential blade speed at the specific radial location. The specific blade profile span is defined as a dimensionless chord length (x/ch), defined in Section 4.3.1 .

5.1.1 Characteristic tests

The numerical and experimental static pressure and static efficiency values for the B2a-fan are shown in figure 5.1 and figure 5.2. The same instrumentation was used by Louw (2015). As discussed in chapter 4, one experimental test set is run through a range of flow rates. Three sets of experimental tests were conducted, each data point presented is the average value of the three ailable for each louvre setting. The tests were conducted at different times and provision was made for the changes in atmospheric temperature and pressure. A statistical analysis between the results at each louvre setting for the three data sets is shown in table 5.1. The low standard (σ) and relative deviation (RSD), defined in Appendix C.1 indicates that there is not a large deviation between the data sets. This shows good repeatability of the data sets and thus a reliable experimental procedure.

Table 5.1: Standard deviation and relative standard deviation between the three experimental data sets

Parameter	$\boldsymbol{\sigma}$ **[-]**	***RSD*** **[%]**
η_{ts}	0.02171	3.84
Ψ_{Fs}	0.00392	2.29

Operation at three different duties have been simulated by CFD in order to compare numerical and experimental data: the design flow rate (16 m^3/s, corresponds to ϕ =0.168), a flow rate lower than design (13 m^3/s, corresponds to ϕ =0.135) and a flow rate higher than design (19 m^3/s, corresponds to

ϕ =0.2). The CFD model revealed to be stable and accurate also for flow rate values far from design. The experimental and numerical studies of Louw (2015) are detailed in the literature study (chapter 2) and are compared against the present results. It should be noted that the Louw (2015) recorded thirty seven experimental data sets of the fan static pressure and fan static efficiency. He presented this as an experimental average by fitting a third and fifth order polynomial through the experimental data sets. The design flow rate of the B2a-fan is at a flow coefficient of 0.168 as indicated by the vertical line in the figures below.

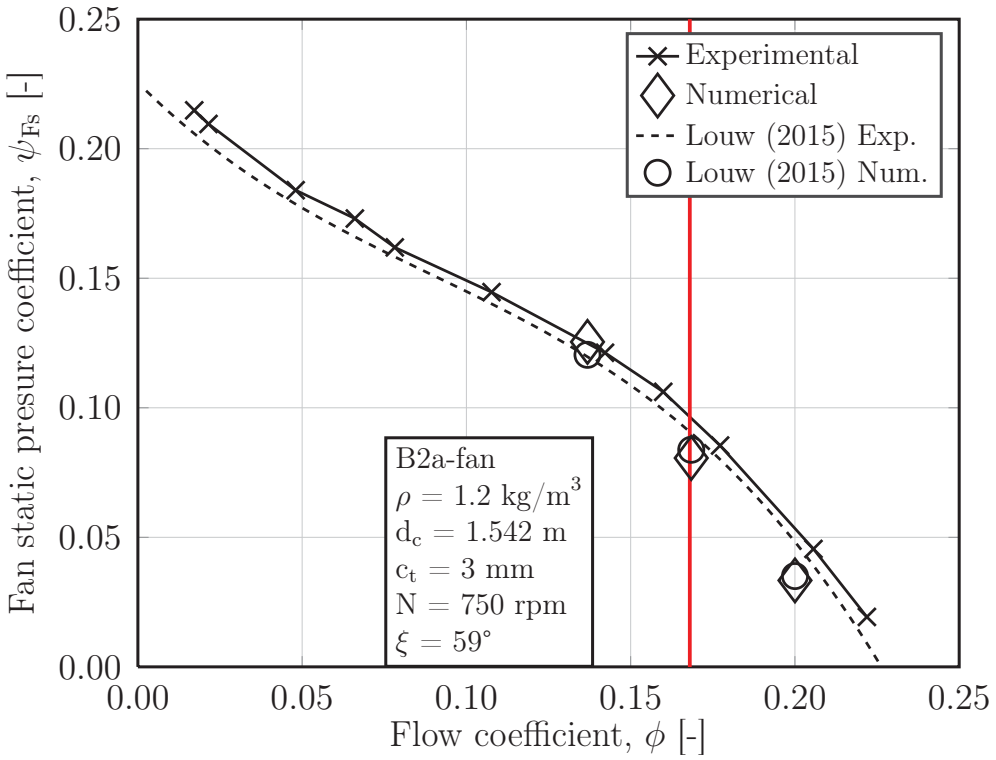

Figure 5.1: B2a-fan static pressure coefficient comparison

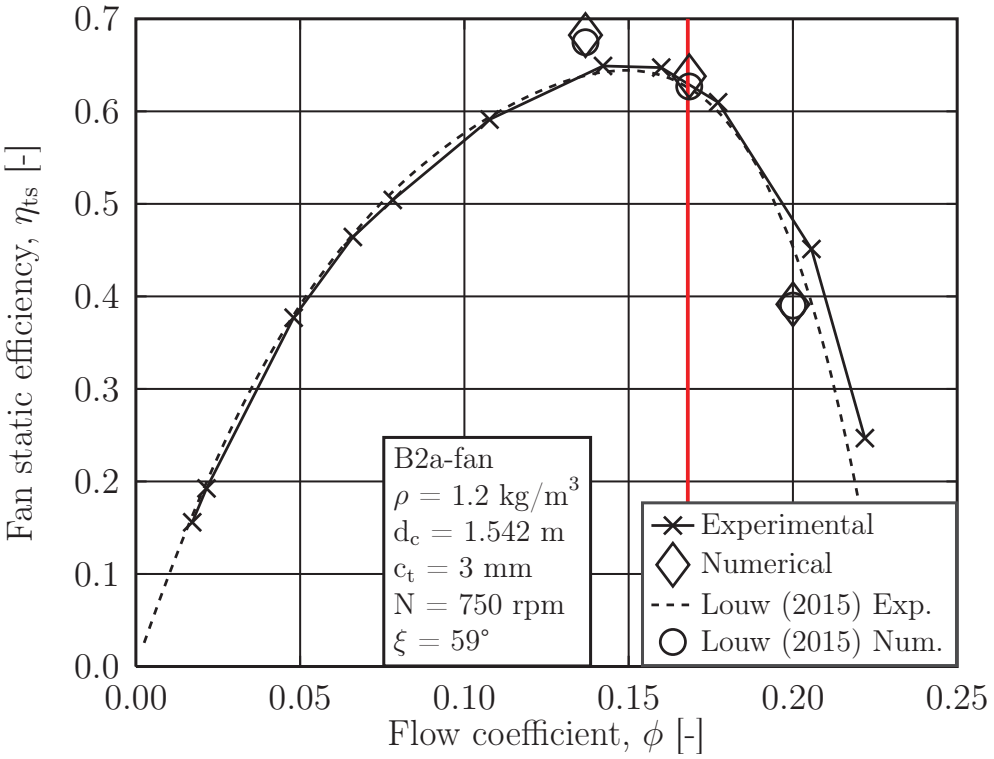

Figure 5.2: B2a-fan static efficiency comparison

The root mean square error (RMSE) and Pearson correlation (R_p) between the experimental data and other sets of data is presented in table 5.2 and table 5.3.

Table 5.2: RMSE between the experimental data and other sets of data for the B2a-fan

Data set	Ψ_{Fs} [-]	η_{ts} [-]
Numerical model	1.87×10^{-2}	9.72×10^{-2}
Exp. data Louw (2015)	8.42×10^{-3}	6.77×10^{-2}
Num. data Louw (2015)	1.31×10^{-2}	9.14×10^{-2}

From figures 5.1 and 5.2 it can be seen that a good correlation exists between the two experimental sets of data. Louw (2015) has a slightly lower fan static pressure throughout the entire flow range. The fan static efficiency deviates more at higher flow rates when compared to lower flow rates. The low RMSE and high Pearson correlation show the good correlation between the experimental data sets. The slight variation could be due to the higher number of experimental tests conducted by Louw (2015), possibly resulting in

Table 5.3: Pearson correlation (R_p) between the experimental data and other sets of data for the B2a-fan

Data set	$\Psi_{\mathbf{Fs}}$	$\eta_{\mathbf{ts}}$
Numerical model	0.9937	0.9751
Exp. data Louw (2015)	0.9985	0.9940
Num. data Louw (2015)	0.9959	0.9783

more accurate results. The results are however very similar and show that the experimental tests correlate well with literature.

The deviation between the numerical and experimental fan static pressure tends to increase with an increasing flow rate. The numerical fan static efficiency is over predicted below the design flow rate and under predicted at higher flow rates. Both these trends are also seen in the work of Louw (2015). It should also be noted that the y^+ values were evaluated for the design operating point (flow rate). The overall discrepancies could be attributed to unrealistic boundary layer simulation. This translates into a discrepancy in the predicted shaft torque, which leads to inaccurate static efficiency in the numerical model. There is however satisfactory correlation between the numerical and experimental data, especially at the design flow rate. This is also backed up by the low RMSE and high Person correlation. It should be noted that the statistical analysis of the numerical simulation is of all three flow rates. The numerical simulation has shown to correlate well with the characteristic experimental data and will be further investigated using more complicated (local) pressure measurements.

5.1.2 Blade surface pressure measurements

Three experimental tests of blade surface pressure measurements were successfully conducted, of which the average is presented. Table 5.4 shows the relative standard deviation between the three results for the various radial blade locations (s_b). The relative standard deviation is small and good repeatability is shown between the data sets.

The numerical and experimental results of the B2a-fan blade surface pressure measurements from the present study and Louw (2015) are shown in figure 5.3. Each subfigure shows the results of the pressure across the chord length (x/ch) at a specific blade span (s_b).

There is an outliner at the fourth pressure tap from the leading edge (x/ch = 0.35) of the pressure side of the blade. This was investigated by switching to a dif-

Table 5.4: Relative standard deviation (RSD) between the three experimental data sets for the pressure and suction side of the blade

Span location, s_b	***RSD* [%], Pressure**	***RSD* [%], Suction**
0.1	4.189	2.759
0.3	1.553	3.617
0.5	1.827	5.155
0.7	2.212	5.391
0.9	5.135	4.689

ferent pressure transducer and repeating the experiment. The same results however occured and the fault therefore was on the blade side of the system. A pressure test was conducted on the specific fan blade channel and a small leak was found inside the blade channel. The BSPM fan blade was stored outside for a duration of approximately three years. It is believed that the silicone tube inside the BSPM could have perished or a connection could have come loose.

There is a relatively small constant difference at the third pressure tap from the leading edge (x/ch = 0.25) of the suction side of the blade. The same procedure as above was conducted in an attempt to investigate the possible deviation from the other data. A leak was however not the cause. Another possible cause of the difference could be due to obstructions inside the blade, which occured during storage. This can however not be the case as a lower negative pressure is recorded than expected. An obstruction could only result if a higher negative pressure is observed. The reason for the error could not be found and further investigation of this would be required if the specific point is needed for an investigation.

The RMSE and pearson correlation between the different sets of data for each respective span length is presented in table 5.5 and table 5.6 after the figures. The outliner at span length x/ch = 0.35 is excluded from the statistical data analysis.

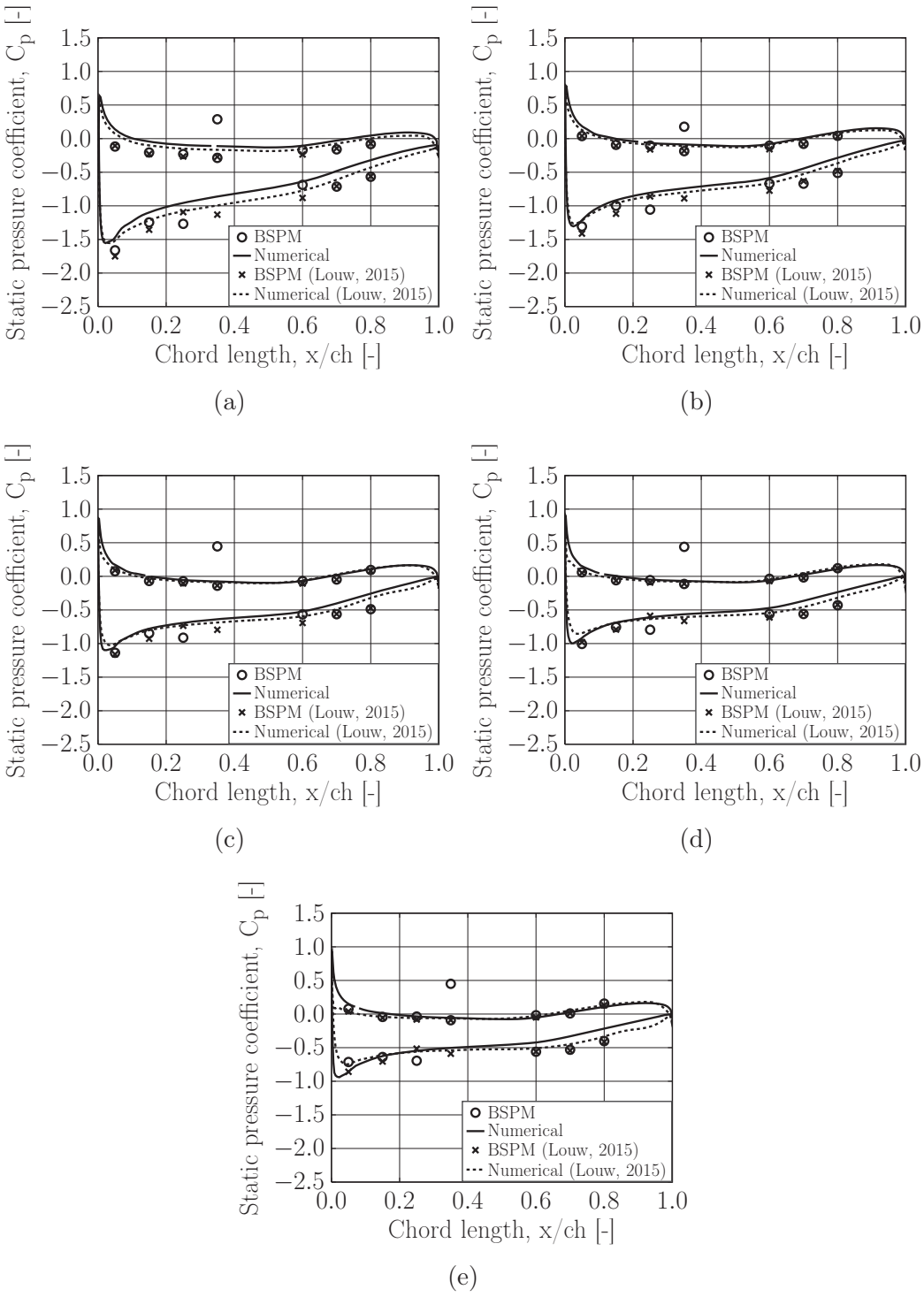

Figure 5.3: Blade surface pressure measurments of the B-fan at its design operating speed at the span length of s_b = (a) 0.1, (b) 0.3, (c) 0.5, (d) 0.7, and (e) 0.9

Table 5.5: RMSE of the static pressure coefficient (C_p) between the BSPM experimental data at design operating point of the B2a-fan

s_b	Numerical model	Exp. Louw (2015)	Num. Louw (2015)
0.1	0.1805	0.0824	0.1112
0.3	0.1315	0.0773	0.0903
0.5	0.1099	0.0643	0.0843
0.7	0.1028	0.0599	0.0782
0.9	0.1034	0.0672	0.0538

Table 5.6: Pearson correlation between the BSPM experimental data at design operating point of the B2a-fan

s_b	Numerical model	Exp. Louw (2015)	Num. Louw (2015)
0.1	0.971	0.986	0.974
0.3	0.986	0.994	0.992
0.5	0.986	0.991	0.989
0.7	0.984	0.996	0.992
0.9	0.955	0.977	0.983

The two experimental sets correlate well with each other, except for the two aforementioned suction taps which have been identified as outliners. The pressure side of the blade has a slightly better correlation than the suction side. The largest difference between the two sets of data is observed at the suction side tap of the leading edge of the blade (x/ch = 0.05). This is however relativly small, which shows that the experimental method has been correctly executed and similar tests can be conducted on the M-Fan.

There is a good correlation between the numerical model and the experimental results. This is seen by the low RMSE and high Pearson correlation. From figure 5.3, it can be seen that the pressure side of the blade has a slightly better correlation than the suction side of the blade. The numerical model has a lower static pressure at the pressure side and suction side of the blade when compared to the numerical model of Louw (2015). This decreases at higher blade spans and the reverse is observed at a localized region on the suction side at the leading edge of the blade chord.

5.1.3 Effect of nose fairing and BSPM module

An investigation into the effect of various hub configurations was conducted on the B2a-fan. Characteristic tests were conducted on a flat plate hub, a

pressure module attached to the flat hub and finally a half sphere nose fairing (shown in Appendix A.1). The results are shown in figure 5.4 to figure 5.6.

The half sphere nose fairing has a higher fan static pressure than the other two configurations close to the design operating point. The same can be seen in the fan power curve. The half sphere nose fairing has a higher fan static efficiency close to its operating point. The same performance trends between the half sphere nose fairing and flat hub on a similar B2-fan can be seen in the work of Bruneau (1994).

The flat plate hub and pressure module attached to a flat hub have very similar results. This shows that the pressure module does not significantly influence the global flow field when compared to the flat plate hub. Even though this is not of value to the B2a-fan, it shows that the effect of BSPM module on an axial fan of comparable size to the M-Fan (which has a flat hub) is very small.

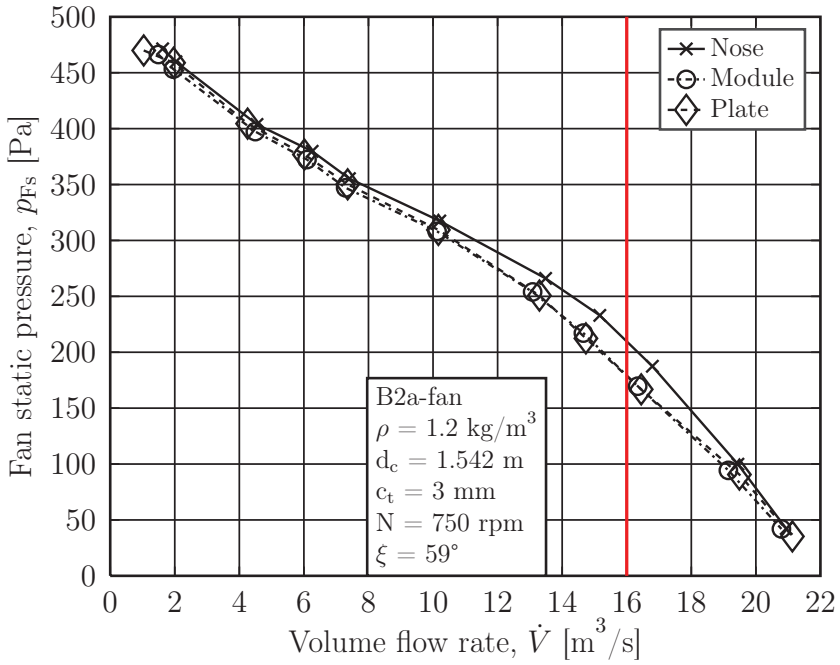

Figure 5.4: B2a-fan static presure coefficient vs flow coefficient (BS848)

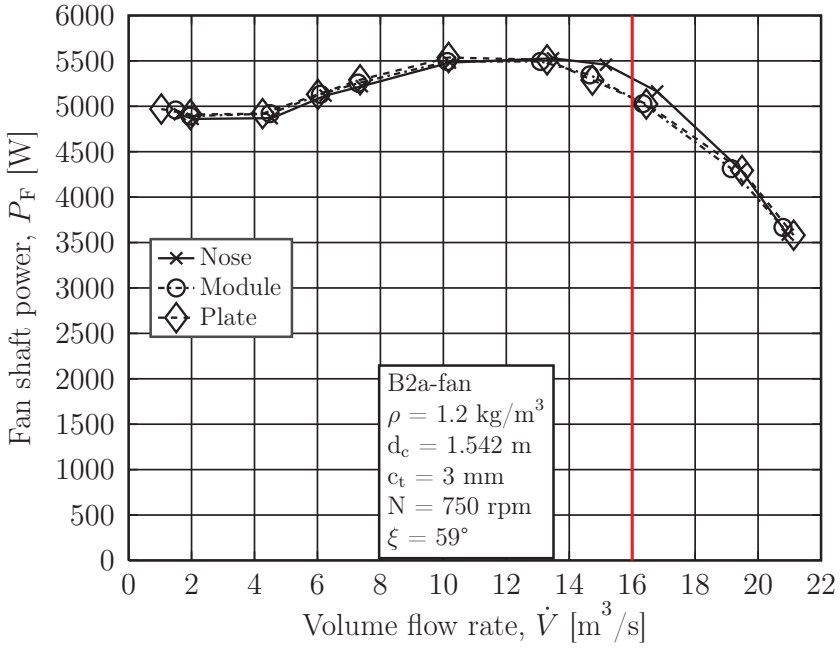

Figure 5.5: B2a-fan Power comparison between various nose configurations

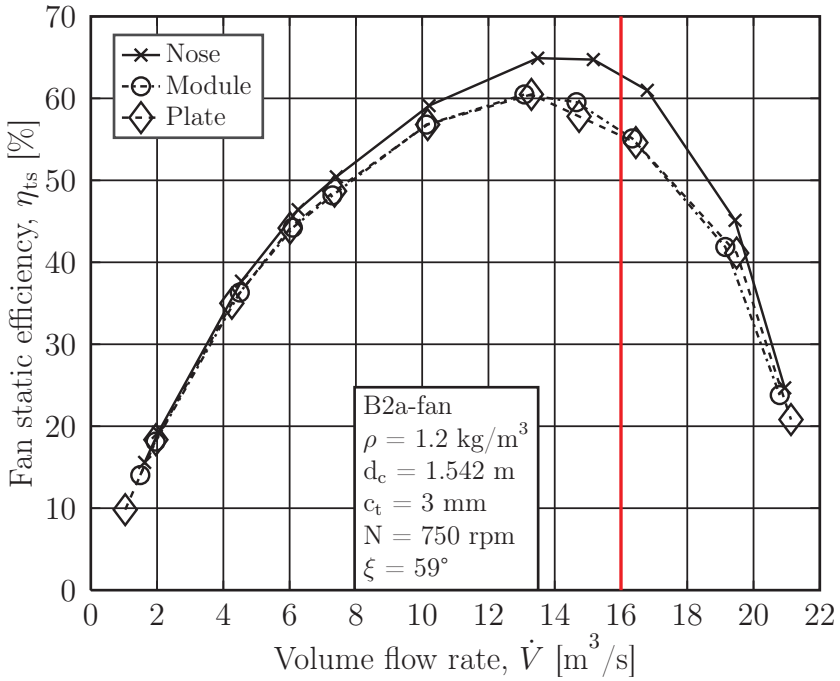

Figure 5.6: B2a-fan static efficiency comparison between various nose configurations

5.2 M-Fan results

Characteristic performance tests and BSPM are performed on the M-Fan. These are compared to the numerical model and literature where possible.

5.2.1 Characteristic tests

The numerical and experimental fan static pressure, power and static efficiency values for the M-fan are shown in figures 5.7, 5.8 and 5.9. One experimental test set is run through a range of flow rates. Three sets of experimental tests were conducted, of which the mean at each louvre setting is presented. A statistical analysis between the results at each louvre setting for the three data sets is shown in table 5.7. The low standard (σ) and relative deviation (RSD) indicates that there is not a large deviation between the data sets. This shows good repeatability of the data sets and thus a reliable experimental procedure.

Table 5.7: Standard deviation and relative standard deviation between the three experimental data sets

Parameter	$\boldsymbol{\sigma}$	$\boldsymbol{RSD}$
η_{Fs}	1.91 %	2.29 %
p_{Fs}	8.47 Pa	2.54 %

Additional operating points at a flow rate of 12 m^3/s and 16 m^3/s are numerically simulated. The experimental and numerical studies of Wilkinson *et al.* (2018) are detailed in the literature study (chapter 2) and are compared against the present results. It should be noted that Wilkinson *et al.* (2018) numerically modelled the fan with an annular model, similar to the one shown in Appendix B, figure B.2. The experimental results were carried out with a flat plate, similar to the one in the present study. Wilkinson *et al.* (2018) presented data for a 2 mm and 4 mm tip gap and the average of the results will therefore be used for a comparison to the M-Fan with a 3 mm tip gap.

The root mean square error (RMSE) between the experimental data and other sets of data is presented in table 5.8. It should be noted that the statistical analysis of the numerical simulation is of all three flow rates.

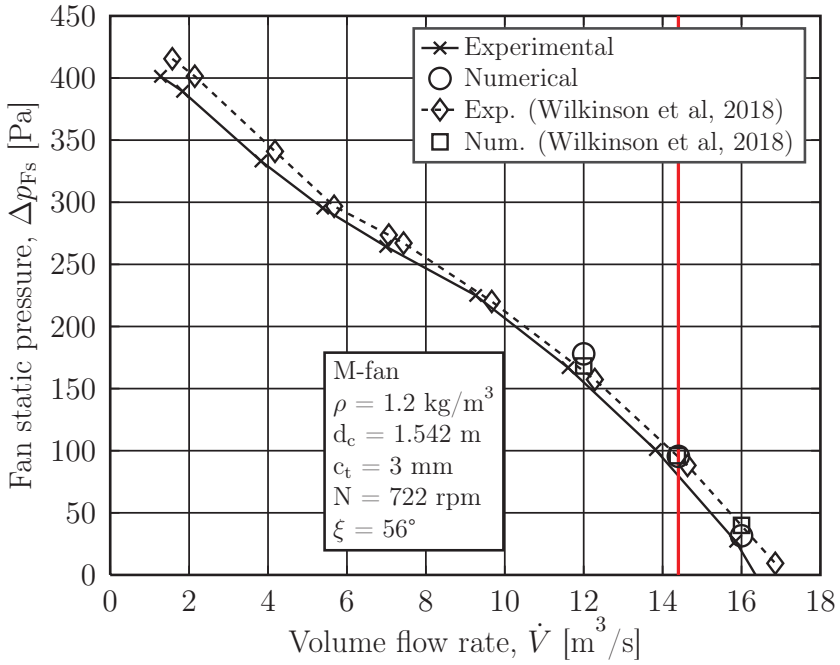

Figure 5.7: M-fan static presure coefficient vs volume flow rate (BS848)

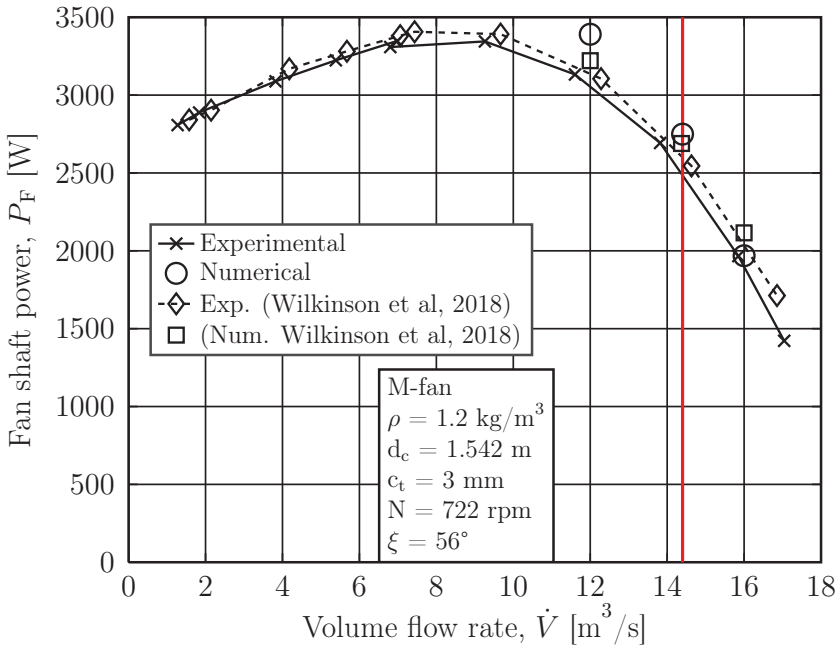

Figure 5.8: M-fan Power vs volume flow rate (BS848)

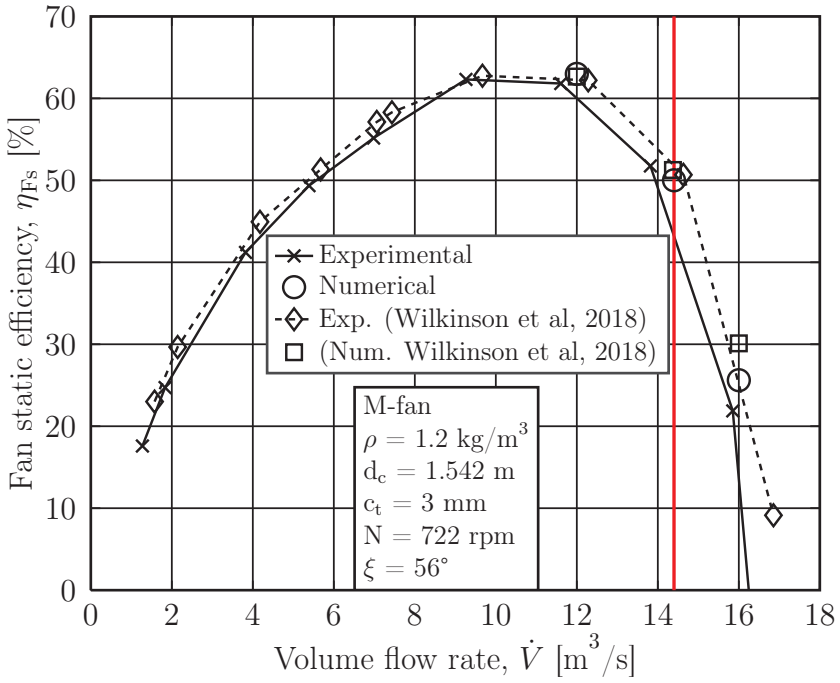

Figure 5.9: M-fan static efficiency vs volume flow rate (BS848)

Table 5.8: RMSE between the experimental data and other sets of data for the M-fan

Data set	η_{Fs} **[%]**	p_{Fs} **[Pa]**
Numerical model	5.02	20.78
Exp. data Wilkinson *et al.* (2018)	3.437	11.72
Num. data Wilkinson *et al.* (2018)	7.35	17.58

From figures figures 5.7, 5.8 and 5.9 it can be seen that a good correlation exists between the two experimental sets of data. Wilkinson *et al.* (2018) has a slightly higher fan static pressure throughout the entire flow range. This trend is also seen for the fan shaft power. The fan static efficiency is slightly lower than Wilkinson *et al.* (2018) and deviates more at higher flow rates when compared to lower flow rates. The low RMSE shows good correlation between the experimental data sets.

The difference in results could be due to a different set of M-fan blades being tested due to the reasons mentioned in section 4.3.1. The blade angles were measured and corresponded with the design specifications. The new set of blades have a different surface finish to the old ones but this is considered negligible. After a visual inspection, some blades exhibit a slight blade sweep

in the axial direction which could cause some deviation from the experimental data of Wilkinson *et al.* (2018). The results are however very similar and show that the experimental tests correlate well with experimental data found in literature.

The numerically simulated data and experimental results correlate relatively well with each other. The numerical fan static pressure and shaft power and static efficiency are consistently above the experimental data but the difference decreases at higher flow rates. The numerically simulated static pressure corresponds better than that of Wilkinson *et al.* (2018) at a flow rate of 16 m^3/s. The discrepancies could be attributed to the difference in inlet and outlet sub domains used in the numerical models.

There is satisfactory correlation between the numerical and experimental data, especially at the design flow rate where the difference is smallest. The numerical simulation has shown to correlate well with the characteristic experimental data and will be further investigated using more complicated (local) pressure measurements.

5.2.2 BSPM setup sensitivity

This section details the effect the BSPM experiental setup has on the performance of the M-Fan. A comparison between the characteristic performance of the M-Fan with two BSPM blades and pressure module and the M-Fan without any special modifications (desgin) is shown in figures 5.10, 5.11, 5.12.

From the graphs it can be seen that there is a slight difference between the two sets of data. The power and static pressure of the BSPM setup are lower than the design M-fan at flow rates below approx. 7 m^3/s and higher thereafter. The static pressure is however very similar and shows good correlation between the two setups. This was also observed for the B2a-fan (section 5.1.3). It can therefore be assumed that the BSPM experimental setup does not have a significant influence on the local flow field distribution of the M-fan.

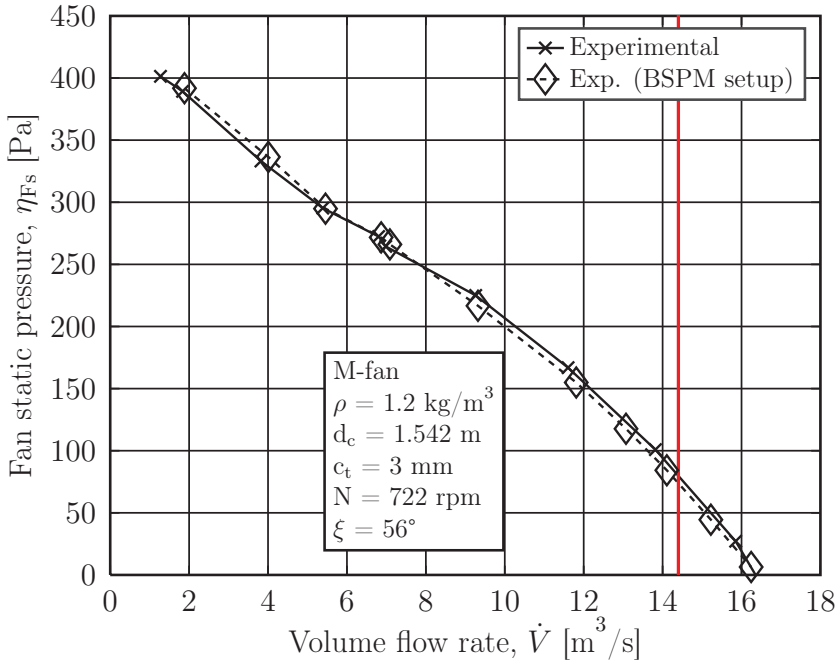

Figure 5.10: M-fan static presure coefficient vs flow coefficient (BS848) of BSPM setup

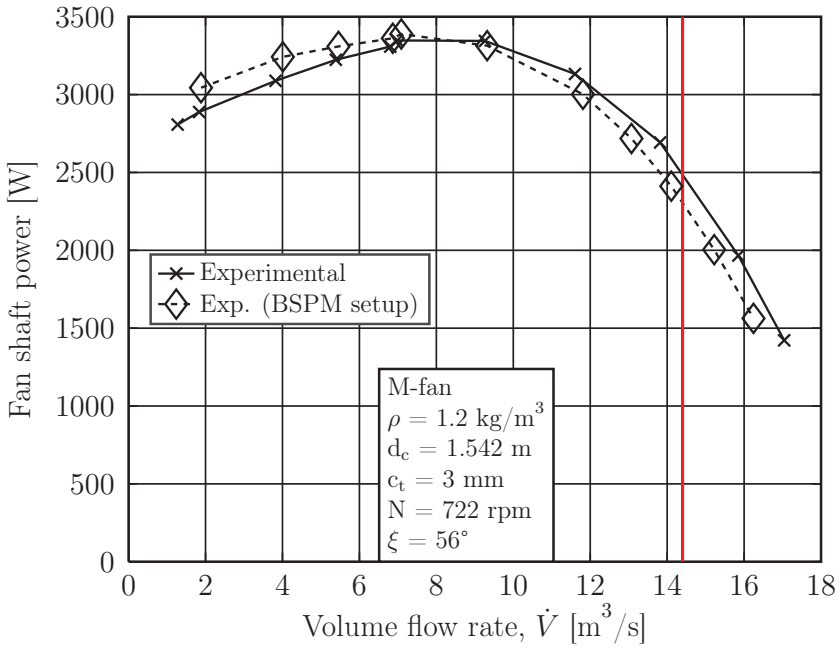

Figure 5.11: M-fan Power vs flow coefficient (BS848) of BSPM setup

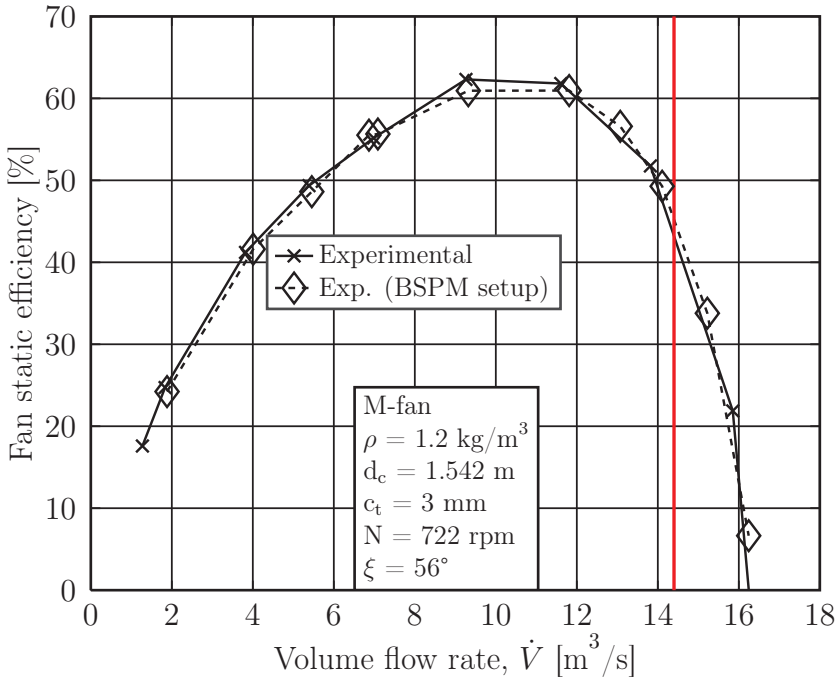

Figure 5.12: M-fan static efficiency vs flow coefficient (BS848) of BSPM setup

5.2.3 M-Fan operating range

An additional test was conduced to investigate the extent of the M-fan operating range. The blade angle was tested at one degree above and below the design root blade angle. The results are shown from figures 5.13 to 5.15.

From the figures, it can be seen that fan static pressure and power is highest at a root blade angle of 35°. The fan static pressure at a root blade angle of 33° is higher than that of the 34° at flow rates below 6 m^3/s and lower at flow rates thereafter. The static efficiency of the root blade angle of 35° is higher than that of the 34° root blade angle at flow rates higher than 10 m^3/s. This should be further investigated as the highest efficiency is traditionally at the design blade angle (34°). The static efficiency at a root blade angle of 33° is similar to that of 34° at flow rates close to the operating point.

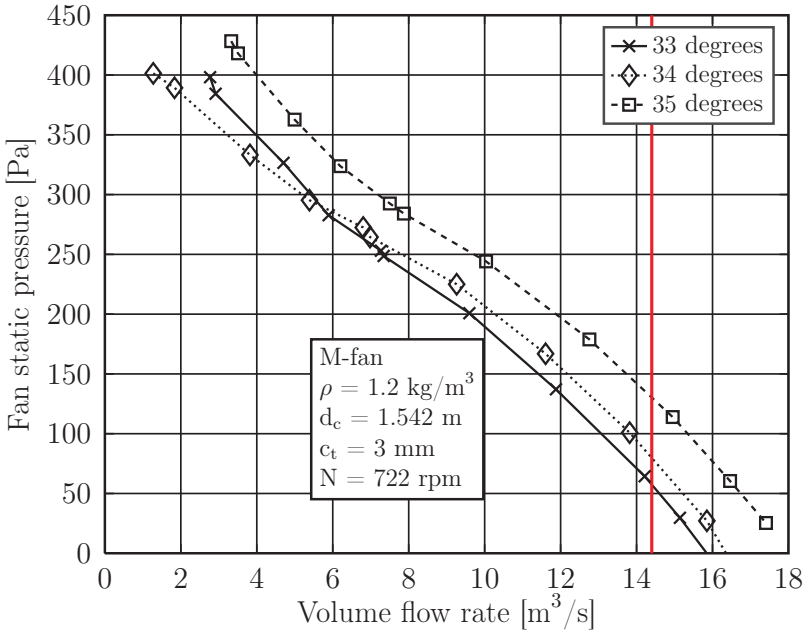

Figure 5.13: M-fan static presure coefficient vs flow coefficient (BS848) at various blade root angles

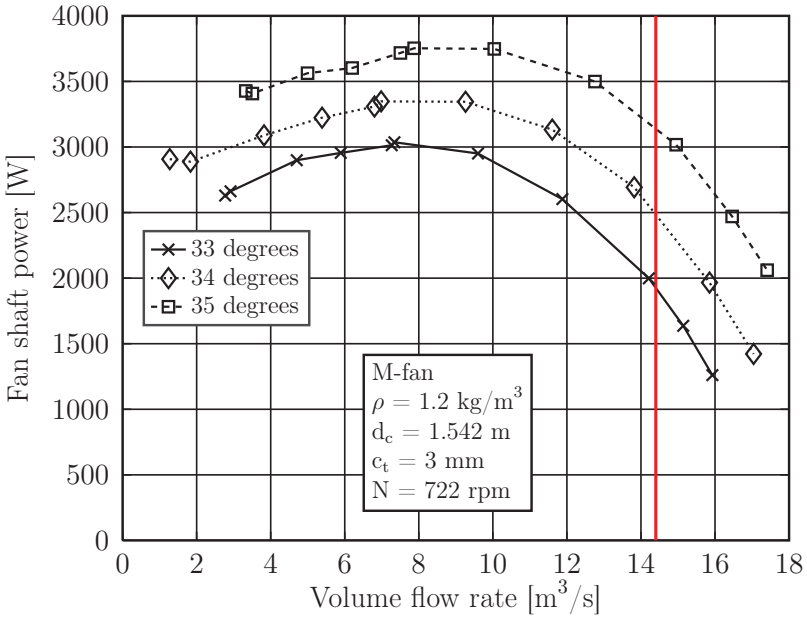

Figure 5.14: M-fan Power vs flow coefficient (BS848) at various blade root angles

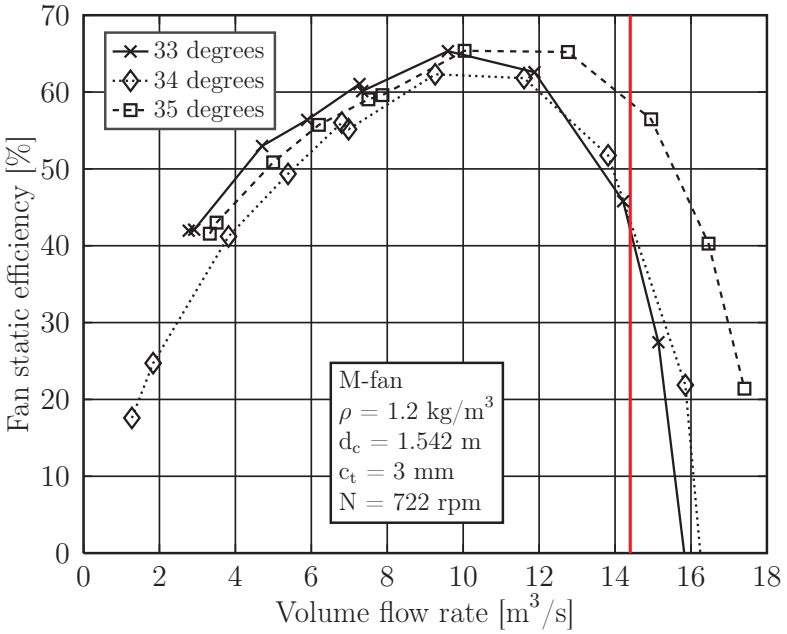

Figure 5.15: M-fan static efficiency vs flow coefficient (BS848) at various blade root angles

5.2.4 Blade surface pressure measurements

Three experimental test sets of blade surface pressure measurements were successfully conducted, of which the average is presented. Table 5.9 shows the relative standard deviation between the three results for the various radial blade locations (s_b). The relative standard deviation is small and good repeatability is shown between the data sets.

The numerical and experimental results of the M-fan blade surface pressure measurements are shown in figure 5.16. Each subfigure shows the results of

Table 5.9: Relative standard deviation (RSD) of static blade pressure between the three experimental data sets for the pressure and suction side of the M-fan blade

Span location, s_b	***RSD* [%], Pressure**	***RSD* [%], Suction**
0.1	2.95	1.29
0.3	3.64	2.59
0.5	4.86	3.57
0.7	3.53	3.16
0.9	2.89	2.86

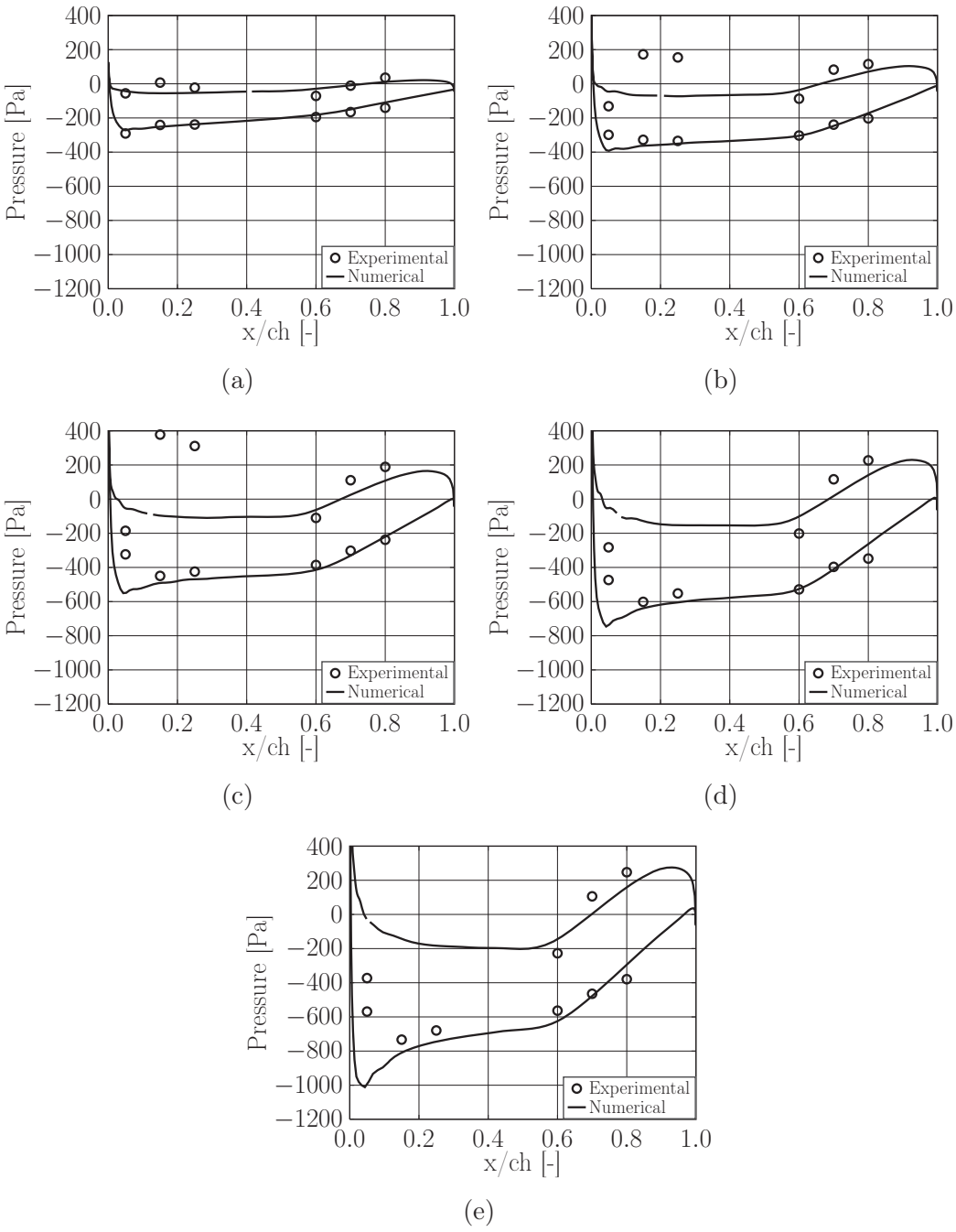

Figure 5.16: Blade surface pressure measurments of the M-fan at its design operating speed at the span length of s_b = (a) 0.1, (b) 0.3, (c) 0.5, (d) 0.7, and (e) 0.9

the pressure across the chord length (x/ch) at a specific blade span (s_b). The root mean square error (RMSE) and Pearson correlation (R_p) between the experimental data and other sets of data is presented in table 5.10. It should be noted that the outliers and faulty points discussed in the next paragraphs have been discarded from the statistical data analysis.

The valid experimental blade surface pressure measurements of the M-Fan correlate well with the numerical simulation. There is a maximum RMSE of 95.51 Pa (average 47.95 Pa, minimum 17.36 Pa) and minimum Pearson correlation of 0.941 (average 0.977). Forty out of sixty possible tap locations are considered for experimental evaluation. Ten experimental points at chord locations $x/ch = 0.15$ and 0.25 on the blade pressure side have been neglected due to channel leaks (as mentioned in section 4.3.1). Ten other points at chord locations $x/ch = 0.15$ on both the blade suction and pressure side have been neglected as they show a clear discontinuity when compared with the other experimental and numerical data. The possible reason for this are discussed at a later stage.

The small deviations between the valid experimental data points and numerically simulated results do not show a clear trend. The differences could be due to small (localized) defects in the blade skin such as smoothness or deviations from the design blade profile. Another reason could be due to the measurement inaccuracies of the pressure transducers, detailed in appendix C.4. The deviances are however small when considering the sensitivity and scale of pressure readings recorded.

The numerically simulated BSPM of the M-fan show a similar trend to that of the B2a-fan. The suction side at the blade leading edge has a steep negative drop due to the high change in velocity. Blade surface pressure then increases along the length of the chord towards the trailing edge. The pressure side of the blade shows a small drop in pressure at the leading edge and an increase in pressure towards the trailing edge. Further details of this are shown in the

Table 5.10: RMSE and Pearson correlation between the BSPM experimental data and numerical model at design operating point of the M-fan

Span location, s_b	**Suction**		**Pressure**	
	RMSE [Pa]	$\boldsymbol{R_p}$	**RMSE [Pa]**	$\boldsymbol{R_p}$
0.1	17.36	0.997	27.71	0.990
0.3	22.29	0.985	53.60	0.941
0.5	33.96	0.995	73.19	0.968
0.7	48.23	0.976	95.51	0.961
0.9	65.33	0.990	92.65	0.970

the following section.

It should be noted that the scale of the graphs are not dimensionless as in the case of the B2a-fan (figure 5.3) but in Pascal. This shows more detail and potential deviations when compared to the BSPM of the B2a-fan. The BSPM of the numerically simluated M-fan and B2a-fan is shown in Appendix B.5.

The difference between the suction and pressure side of the blade increases with an increase in blade span. This is due to the higher tip speed and relative velocity at higher blade spans. At the trailing edge there is a visible increase in pressure on the pressure side of the blade, which results in a duck tail shape. This is due to the slowing down of fluid from the leading edge towards the trailing edge as it follows the blade chord profile.

As mentioned in section 4.3.1, the channels at chord locations of $x/ch = 0.15$ and 0.25 are not air tight. This can be seen by the two outliers in figure 5.13 (b) and 5.13 (c) on the pressure side of the blade. The experimental points for the leaking channels for higher radial locations thereafter are discarded from the datasets and not shown in the graphs so that the scale remains constant and comparable to the other figures.

Both the experimental suction and pressure surface measurements of the leading edge at chord locations of $x/ch = 0.05$ do not correlate well with the numerical data. They show a discontinuity in the experimentally measured blade surface pressure profile (points).

A possible reason for the deviance could be due to slight blockages of the silicone tubes inside the BSPM blade. This is difficult to determine and air was blown through these channels to see whether a difference between the other functional channels is noticed. No clear difference between the channels was noticed. The recorded data of the pressure taps was also analysed. There is a constant value and no trend was observed (lagging) which would typically be seen in a blocked channel.

Another reason could be that the blade profile of the leading edge is different to the design blade profile (localized manufacturing deviance). This is however unlikely as the characteristic test (section 5.2.1) shows good correlation to experimental data. The leading edge of the blade was also visually inspected and did not show any obvious manufacturing faults.

A pressure transducer from a successfully measured blade channel was swapped with the pressure transducer at the faulty tap location. The same results however occured and the fault does therefore not lie with the pressure transducer.

5.3 M-Fan flow visualizations

The flow field obtained from the numerical simulation of the M-fan at its operating point is investigated. The high correlation between the experimental and numerical BSPM shows that further investigations on the M-fan numerical model can be considered for future investigations. The flow visualisations show some of the basic flow over the blade and further confirm successful numerical modelling.

The velocity streamlines of the M-fan blade for the pressure and suction side are shown in figure 5.17. From the figure it can be seen that the flow over the blades follows the circular arc of the aerofoils along the entire span of the blade. This includes flow close to the blade root, where deviances can easily occur. The free-vortex design is clearly seen by the uniform radial flow over the blade span.

The velocity and pressure distribution over the blade chord over various blade span lengths are shown in figure 5.18. The scales have been adjusted to clearly show the pressure and velocity gradients along the chord length.

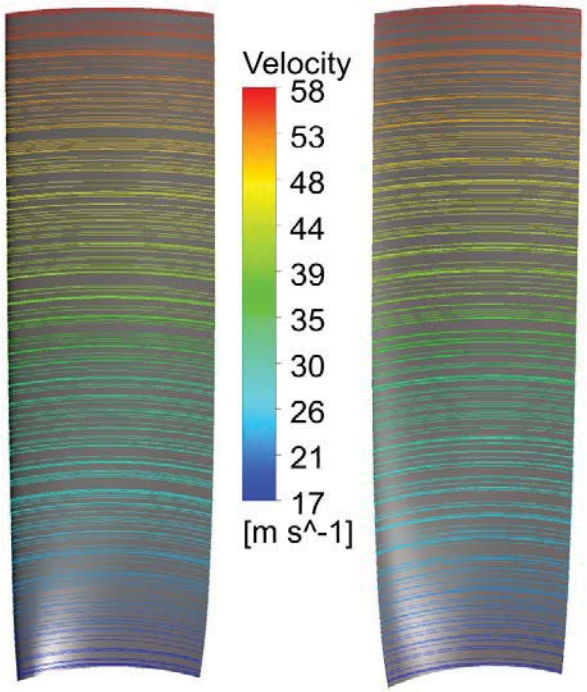

(a) (b)

Figure 5.17: Velocity streamlines of the M-fan blade for the blade (a) pressure side and (b) suction side

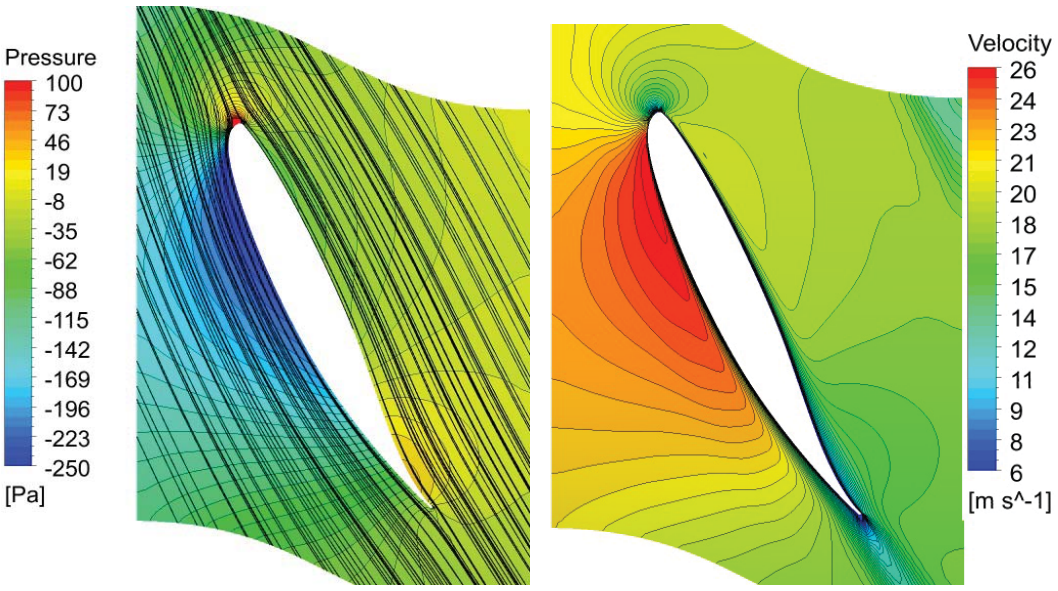

(a)

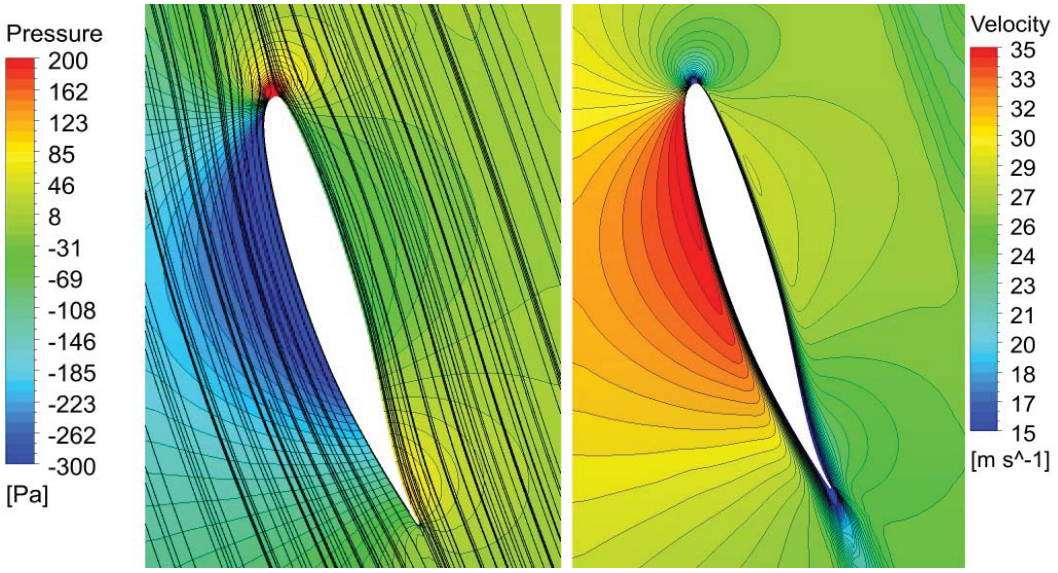

(b)

Figure 5.18: Velocity and pressure distribution of the blade chord at blade span locations of (a) s_{b}=0.1 and (b) s_{b}=0.3

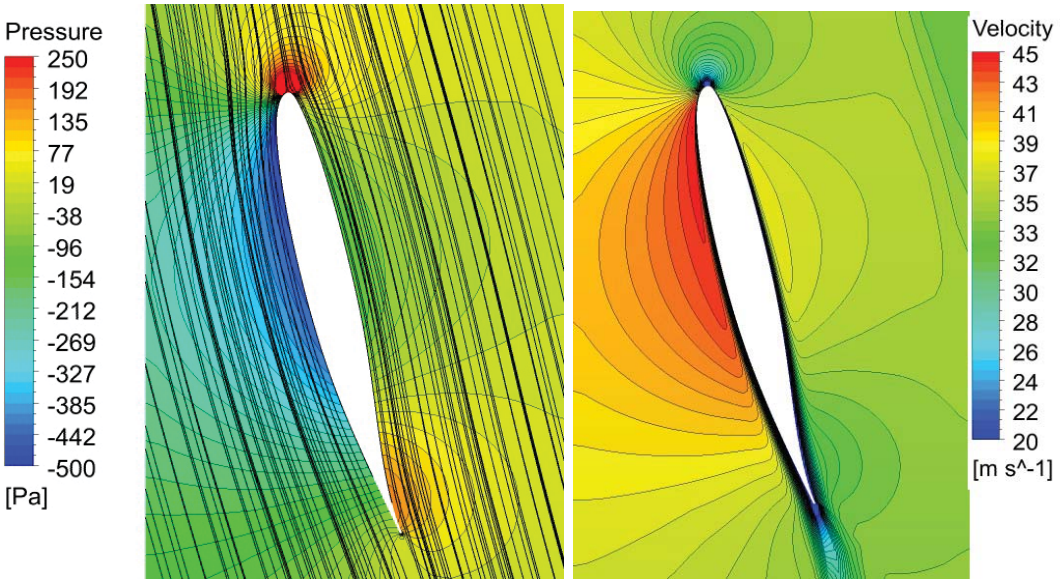

(c)

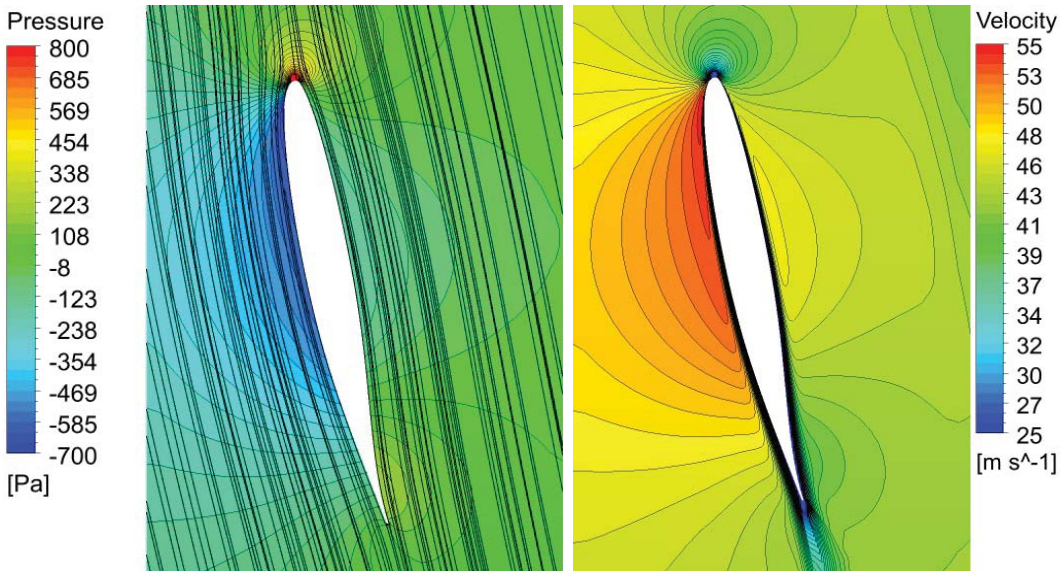

(d)

Figure 5.18: Velocity and pressure distribution of the blade chord at blade span locations of (c) $s_{\mathrm{b}} = 0.5$ and (d) $s_{\mathrm{b}} = 0.7$

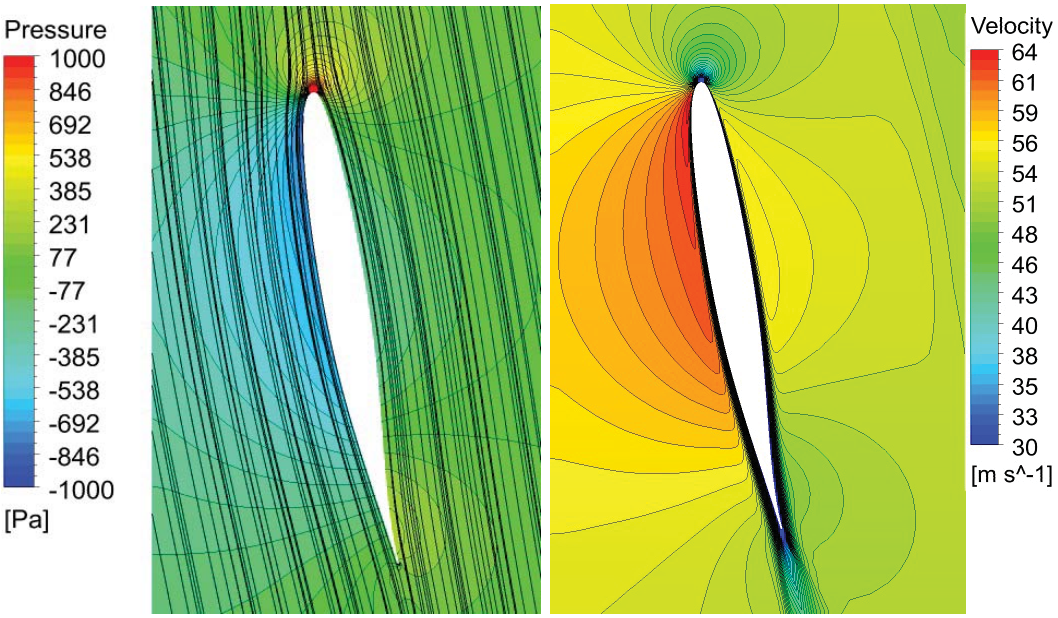

(e)

Figure 5.18: Velocity and pressure distribution of the blade chord at blade span locations of (e) $s_b = 0.9$

From figure 5.18 it can be seen that an increase in velocity on the suction side of the blade correlates with a decrease in pressure. This becomes more prevalent at higher blade span lengths and agrees with the BSPM shown in the previous section. The velocity contour plots show a wake at the trailing edge of the blade.

5.4 Summary

The characteristic performance tests of the B2a-fan and M-fan correlate well with their respective numerical simulation and literature. The results for the BSPM of the B2a-fan correlate well with literature and the experimental methodology has been successfully validated. The experimental and numerically simulated BSPM results of the M-fan correlate well with each other. Overall, the experimental results show that the methodology has a high level of precision and accuracy when determining the blade surface pressure measurements of two axial flow fans and can provide information on local flow fields along the blade span.

Chapter 6

Conclusion

6.1 Contributions

Experimental data on the operational fan performance can be used to analyse and further improve existing fan designs. A scale model ($d_c = 1.543$ m) of the M-fan is numerically modelled and experimentally tested. The experimental tests comprise of characteristic performance tests and blade surface pressure measurements. The experimental method and numerical model was firstly verified by testing an existing B2a-fan which was manufactured for blade surface pressure measurements and then applied on the scale model M-fan.

A periodic (1/8th) three dimensional numerical model of a single blade passage in a BS 848, type A test facility was generated. The geometry and mesh creation was performed using ANSYS® 17.2 Workbench and the simulation solved using ANSYS® Fluent. The computational domain was created using a frozen rotor approach. The blade, inlet and outlet mesh subdomain are detailed along with their respective boundary conditions. RANS turbulence modelling was conducted using the realizable k-e turbulence model and the enhanced wall function was used to model the flow near the wall boundary layer for the M-Fan.

Standard fan performance (characteristic) testing was conducted on both the scale M-fan and B2a-fan at the BS 848, type A test facility. A description of the test apparatus, experimental procedure and data processing is detailed. Blade surface pressure measurements were conducted in the existing B2a-fan blades and on the specially constructed M-Fan blades. Sixty M-fan pressure taps were measured at the design operating point, of which forty were deemed to be significant. The design of the specially manufactured fan as well as the experimental equipment, methods and data processing are explained in detail.

The experimentally determined characteristic curves of the B2a-fan compare well with those found in literature. The numerical model accurately predicts the static pressure and static fan efficiency at the design operating point. The experimental blade surface pressure measurements correlated well with the numerical data with minimum Pearson correlation factor of 0.955 (average 0.988). These results also correlated well with the work found in literature.

The experimentally determined M-fan static pressure, power and static efficiency (characteristic curves) compare well with the numerical model. The blade surface pressure measurements were successfully conducted on the newly constructed blades. Good repeatability was observed between the experimental data sets. The numerical model correlates well with the experimental data with a maximum RMSE of 95.51 Pa (average 47.95 Pa, minimum 17.36 Pa) and minimum Pearson correlation of 0.941 (average 0.977).

The experimental method used to measure the blade surface pressure is shown to be reliable and accurate for two axial flow fans. The manufacturing method of the BSPM blade can be scaled up to large scale fans by using suitably robust tubes. The experimental method, together with the numerical model, can be used as an effective tool to provide further understanding on local flow distribution (surface pressure) existing in the vicinity of axial flow fans in air cooled condensers.

6.2 Future Work and Recommendations

The objectives of the present study have all been achieved. Based on these, the following proposals and recommendations are made for future work:

- Since experimental information concerning the performance on the scale M-Fan has been conducted, it naturally follows that further tests need to be conducted on the full scale M-Fan at the full scale test facility at Stellenbosch University (currently under construction). Blade surface pressure measurements could be compared against the experimental data obtained in the current study.
- A numerical model of the full scale test facility at Stellenbosch University (currently under construction) should be created and compared to the experimental data obtained in this study or full scale experimental results.
- Numerically and experimentally investigate BSPM of the M-Fan at various flow rates and different hub configurations should be investigated

numerically and experimentally.

- The feasibility of performing on site blade surface pressure measurements should be assessed and possible apparatus and methods for industrial implementation should be investigated.

List of References

ANSYS Fluent Inc. (2017). ANSYS Fluent 17.0 Users Guide.

Augustyn, O. (2013). *Experimental and numerical analysis of axial flow fans*. M. Eng thesis, Stellenbosch University.

Augustyn, O.P., Van Der Spuy, S.J. and Von Backström, T.W. (2016). Numerical and experimental investigation into the accuracy of the fan scaling laws applied to large diameter axial flow fans. *Proceedings of the Institution of Mechanical Engineers, Part A: Journal of Power and Energy*, vol. 230, no. 5, pp. 477–486. ISSN 20412967.

Bamberger, K. and Carolus, T. (2012). Optimization of axial fans with highly swept blades with respect to losses and noise reduction. *Noise Control Engineering Journal*, vol. 60, no. 6, pp. 716–725. ISSN 07362501.

Bamberger, K. and Carolus, T. (2014). Performance prediction and optimization of low pressure axial fans by artificial neural networks. *10th European Conference on Turbomachinery Fluid Dynamics and Thermodynamics, ETC 2013*. ISSN 24104833.

Beiler, M.G. and Carolus, T.H. (1999). Computation and Measurement of the Flow in Axial Flow Fans With Skewed Blades. *Journal of Turbomachinery*, vol. 121, no. 1, p. 59. ISSN 0889504X.

Bredell, J.R. (2005). *Numerical Investigation of Fan Performance in a*. Masters, Stellenbosch University.

Bruneau, P.R.P. (1994). *The design of an axial flow fan for a cooling tower application*. M. Eng thesis, Stellenbosch University.

BSI Group (2007). BS EN ISO 5801:2008, BS 848-1:2007 Industrial fans. - performance testing using standardized airways.

Corsini, A. and Rispoli, F. (2004). Using sweep to extend the stall-free operational range in axial fan rotors. *Proceedings of the Institution of Mechanical*

Engineers, Part A: Journal of Power and Energy, vol. 218, no. 3, pp. 129–140. ISSN 09576509.

Corsini, A. and Rispoli, F. (2005). Flow analyses in a high-pressure axial ventilation fan with a non-linear eddy-viscosity closure. *International Journal of Heat and Fluid Flow*, vol. 26, no. 3, pp. 349–361. ISSN 0142727X.

Corsini, A., Rispoli, F. and Sheard, A.G. (2007). Development of improved blade tip endplate concepts for low-noise operation in industrial fans. *Proceedings of the Institution of Mechanical Engineers, Part A: Journal of Power and Energy*, vol. 221, no. 5, pp. 669–681. ISSN 09576509.

Corsini, A., Rispoli, F. and Sheard, A.G. (2010). Shaping of Tip End-Plate to Control Leakage Vortex Swirl in Axial Flow Fans. *Journal of Turbomachinery*, vol. 132, no. 3, p. 031005. ISSN 0889504X.

Downie, R.J., Thompson, M.C. and Wallis, R.A. (1993). An engineering approach to blade designs for low to medium pressure rise rotor-only axial fans. *Experimental Thermal and Fluid Science*, vol. 6, no. 4, pp. 376–401. ISSN 08941777.

Estevadeordal, J., Gogineni, S., Copenhaver, W., Bloch, G. and Brendel, M. (2000). Flow field in a low-speed axial fan: A DPIV investigation. *Experimental Thermal and Fluid Science*, vol. 23, no. 1-2, pp. 11–21. ISSN 08941777.

Fluent, A. (). Ansys Fluent Theory guide.

Goldschagg, H.B. (1993). Lessons Learned from the World's largest Forced Draught Direct Air-Cooled Condenser. In: *EPRI Meet.* Washington, U.S.A.

Himmelskamp, H. (1947). *Profile investigations on a rotating airscrew.* PhD, University of Göttingen.

Hunnabal, P. (1992). Control of Tonal Noise Generation in Axial Flow Fans by Optimizing Geometry of Fixed and Rotating Components. In: *Int. INCE Symp.*, pp. 475–482. CETIM, Senlis, France.

Hurault, J., Kouidri, S. and Bakir, F. (2012). Experimental investigations on the wall pressure measurement on the blade of axial flow fans. *Experimental Thermal and Fluid Science*, vol. 40, pp. 29–37. ISSN 08941777.

Hurault, J., Kouidri, S., Bakir, F. and Rey, R. (2010). Experimental and numerical study of the sweep effect on three-dimensional flow downstream of axial flow fans. *Flow Measurement and Instrumentation*, vol. 21, no. 2, pp. 155–165. ISSN 09555986.

Kergourlay, G., Kouidri, S., Rankin, G.W. and Rey, R. (2006). Experimental investigation of the 3D unsteady flow field downstream of axial fans. *Flow Measurement and Instrumentation*, vol. 17, no. 5, pp. 303–314. ISSN 09555986.

Kröger, D.G. (2004). *Air-cooled Heat Exchangers and Cooling Towers*. vol1 edn. PennWell Corporation, Tulsa, USA.

Lanzafame, R., Mauro, S. and Messina, M. (2013). Wind turbine CFD modeling using a correlation-based transitional model. *Renewable Energy*, vol. 52, pp. 31–39. ISSN 09601481.

Launder, B. and Spalding, D. (1974). The numerical computation of turbulent flows. *Computer Methods in Applied Mechanics and Engineering*, vol. 3, no. 2, pp. 269–289. ISSN 00457825. `1204.1280v1`.

le Roux, F.N. (2010). *The CFD simulation of an axial ow fan*. M. Eng thesis, Stellenbosch University.

Lee, G.H., Baek, J.H. and Myung, H.J. (2005). Effect of blade loading on the structure of tip leakage flow in a forward-swept axial-flow fan. *HVAC and R Research*, vol. 11, no. 1, pp. 95–117. ISSN 10789669.

Li, Y., Liu, J., Ouyang, H. and Du, Z.H. (2008). Internal flow mechanism and experimental research of low pressure axial fan with forward-skewed blades. *Journal of Hydrodynamics*, vol. 20, no. 3, pp. 299–305. ISSN 10016058.

Lien, F.S. and Leschziner, M.A. (1994). Assessment of turbulence-transport models including non-linear rng eddy-viscosity formulation and second-moment closure for flow over a backward-facing step. *Computers and Fluids*, vol. 23, no. 8, pp. 983–1004. ISSN 00457930.

Longhouse, R.E. (1977). Vortex shedding noise of low tip speed, axial flow fans. *Journal of Sound and Vibration*, vol. 53, no. 1, pp. 25–46. ISSN 10958568.

Louw, F.G. (2011). *Performance Trends of a Large Air-Cooled Steam Condenser during Windy Conditions*. Masters, Stellenbosch University.

Louw, F.G. (2015). *Investigation of the flow field in the vicinity of an axial flow fan during low flow rates*. Ph.D. thesis, Stellenbosch University.

Louw, F.G., Bruneau, P.R.P., Von Backström, T.W. and Van der Spuy, S.J. (2012). The design of an axial flow fan for application in large air-cooled heat exchangers. *The Proceeding of ASME Turbo Expo 2012*, pp. 1–15.

Louw, F.G., Von Backström, T.W. and Van der Spuy, S.J. (2014). Investigation of the flow field in the vicinity of an axial flow fan during low flow rates. *The Proceedings of ASME Turbo expo 2014*.

Masi, M., Castegnaro, S. and Lazzaretto, A. (2016 aug). Forward sweep to improve the efficiency of rotor-only tube-axial fans with controlled vortex design blades. *Proceedings of the Institution of Mechanical Engineers, Part A: Journal of Power and Energy*, vol. 230, no. 5, pp. 512–520. ISSN 0957-6509.

Meissner, T.W. (2018). *Numerical Investigation of the Effect of Scaling on the Performance of Large Scale Axial Flow Fans by*. M. Eng thesis, University of Stellebosch.

Menter, F.R. (1994). Two-Equation Eddy-Eiscosity Turbulence Models for Engineering Applications. *AIAA journal*, vol. 32, no. 8, pp. 1598–1605. ISSN 0001-1452.

Meyer, C.J. (2005). Numerical investigation of the effect of inlet flow distortions on forced draught air-cooled heat exchanger performance. *Applied Thermal Engineering*, vol. 25, no. 11-12, pp. 1634–1649. ISSN 13594311.

Meyer, C.J. and Kröger, D.G. (2001). Air-cooled heat exchanger inlet flow losses. *Applied Thermal Engineering*, vol. 21, no. 7, pp. 771–786. ISSN 13594311.

MinWaterCSP (2018). MinWaterCSP Project.
Available at: `https://www.minwatercsp.eu/`

Owen, M.T.F. and Kröger, D.G. (2010). The effect of screens on air-cooled steam condenser performance under windy conditions. *Applied Thermal Engineering*, vol. 30, no. 16, pp. 2610–2615. ISSN 13594311.

Salta, C.A. and Kröger, D.G. (1995). Effect of inlet flow distortions on fan performance in forced draught air-cooled heat exchangers. *Heat Recovery Systems and CHP*, vol. 15, no. 6, pp. 555–561. ISSN 08904332.

Schreck, S.J. (2007). Rotationally Augmented Flow Structures and Time Varying Loads on Turbine Blades Preprint. *45th AIAA Aerospace Sciences Meeting and Exhibition, Wind Energy Symposium*, , no. January, pp. 1–13.

Shih, T.-H., Liou, W.W., Shabbir, A., Yang, Z. and Zhu, J. (1995). A new k-e eddy viscosity model for high reybolds number turbulent flows. *Compurers Fluids*, vol. 24, no. 3, pp. 227–238. ISSN 00457930. `NIHMS150003`.

Sørensen, D., Thompson, M. and Sørensen, J. (2000). Toward improved rotor-only axial fans. 2: Design optimization for maximum efficiency. *Journal of fluids engineering*, vol. 122, no. June, pp. 324–330. ISSN 00982202.

Spalart, P. and Allmaras, S. (1992). A one-equation turbulence model for aerodynamic flows. *30th Aerospace Sciences Meeting and Exhibit*, , no. April 2015. ISSN 00341223. `arXiv:1011.1669v3`.

Stinnes, W.H. and Von Backström, T.W. (2002). Effect of cross-flow on the performance of air-cooled heat exchanger fans. *Applied Thermal Engineering*, vol. 22, no. 12, pp. 1403–1415. ISSN 13594311.

Thiart, G.D. and von Backström, T.W. (1993). Numerical simulation of the flow field near an axial flow fan operating under distorted inflow conditions. *Journal of Wind Engineering and Industrial Aerodynamics*, vol. 45, no. 2, pp. 189–214. ISSN 01676105.

Ubaldi, M., Zunino, P. and Cattanei, A. (1994). Relative flow and turbulence measurements within and downstream of an axial flow rotor. *Experimental Thermal and Fluid Science*, vol. 9, no. 2, pp. 186–196. ISSN 08941777.

Vad, J. (2008). Aerodynamic effects of blade sweep and skew in low-speed axial flow rotors at the design flow rate: An overview. *Proceedings of the Institution of Mechanical Engineers, Part A: Journal of Power and Energy*, vol. 222, no. 1, pp. 69–85. ISSN 09576509.

Vad, J. and Bencze, F. (1998). Three-dimensional flow in axial flow fans of non-free vortex design. *International Journal of Heat and Fluid Flow*, vol. 19, no. 6, pp. 601–607. ISSN 0142727X.

Vad, J., Kwedikha, A.R. and Jaberg, H. (2006). Effects of blade sweep on the performance characteristics of axial flow turbomachinery rotors. *Proceedings of the Institution of Mechanical Engineers, Part A: Journal of Power and Energy*, vol. 220, no. 7, pp. 737–751. ISSN 09576509.

Vad, J., Kwedikha, A.R.A., Horváth, C., Balczó, M., Lohász, M.M. and Régert, T. (2007). Aerodynamic effects of forward blade skew in axial flow rotors of controlled vortex design. *Proceedings of the Institution of Mechanical Engineers, Part A: Journal of Power and Energy*, vol. 221, no. 7, pp. 1011–1023. ISSN 09576509.

Van der Spuy, S.J. (2011). *Perimeter Fan Performance in Forced Draught Air-cooled Steam Condensers*. Ph.D. thesis, University of Stellenbosch.

Van der Spuy, S.J., von Backström, T.W.V. and Kröger, D.G. (2009). Performance of low noise fans in power plant air cooled steam condensers. *Noise Control Engineering Journal*, vol. 57, no. 4, pp. 1–8. ISSN 07362501.

Van Niekerk, C. (1958). Ducted fan design theory. *J. appl. Mech*, vol. 25, no. 3, pp. 325–331.

Venter (1990). *The Effectiveness of Axial Flow Fans in A-Frame Plenums*. Ph.D. thesis, University of Stellenbosch.

Venter, S.J. and Kröger, D.G. (1992). The effect of tip clearance on the performance of an axial flow fan. *Energy Conversion and Management*, vol. 33, no. 2, pp. 89–97. ISSN 01968904.

Versteeg, H. and Malalasekera, W. (2007). *An introduction to computational fluid dynamics*. 2nd edn. Pearson Prentice Hall, Harlow, England.

Wadia, A.R., Szucs, P.N. and Crall, D.W. (1998). Inner Workings of Aerodynamic Sweep. *Journal of Turbomachinery*, vol. 120, no. 4, p. 671. ISSN 0889504X.

Wallis, R.A. (1983). *Axial flow fans and ducts*. John Wiley & Sons Inc. ISBN 0471870862.

White, F.M. (2006). *Viscous Fluid Flow*. 3rd edn. McGraw-Hill, Singapore.

Wilcox, D. (1988). Re-assessment of the scale-determining equation for advanced turbulence models. *AIAA Journal*, vol. 26, no. 11, pp. 1299–1310.

Wilkinson, M., Volponi, D., Bonanni, T., Tieghi, L., Delibra, G., Corsini, A., Van der Spuy, S. and von Backström, T. (2018 may). CFD simulation results for the MinWaterCSP cooling fan. In: *Fan 2018*, May. Darmstadt, Germany.

Wilkinson, M.B. (2017). *The Design of an Axial Flow Fan for Air-Cooled Heat Exchanger Applications*. Masters Thesis, University of Stellenbosch.

Wilkinson, M.B. and Van der Spuy, S.J. (2015). The effect of fan tip configuration on air-cooled condenser axial flow fan performance. In: *Fan 2015*, pp. 1–12. Lyon, France.

Ye, X., Li, P., Li, C. and Ding, X. (2015). Numerical investigation of blade tip grooving effect on performance and dynamics of an axial flow fan. *Energy*, vol. 82, pp. 556–569. ISSN 03605442.

Yoon, J.H. and Lee, S.J. (2004). Stereoscopic PIV measurements of flow behind an isolated low-speed axial-fan. *Experimental Thermal and Fluid Science*, vol. 28, no. 8, pp. 791–802. ISSN 08941777.

Appendix A

Fan specifications and BSPM-fan details

Details of the M-fan and B2a-fan used in this thesis are provided in the sections below. Both fans are designed for a bellmouth casing diameter (d_c) of 1.543 m and the fans are constructed using a carbon fibre hand layup. The tip gap for each individual blade was set at 3 mm for this thesis. All specifications are given at standard atmospheric conditions. Details of the fan blades used for experimental blade surface pressure measurements are also provided at the end of the section.

A.1 Fan specifications

The B2a-fan makes use of the NASA LS 0413 aerofoil of McGhee and Beasley (1976). The fan blade shape is of a near free vortex design, with some relaxation of stagger angles occuring at the hub to reduce the angle of twist and increase the stall margin. The hub and tip chord lengths are determined by employing hub-tip lift coefficients to fit the design constraints. The B2a-fan uses a fixed aerofoil section between its root and tip, with a decrease in aerofoil thickness ($\Delta y/x$) from 0.013 at the blade root to 0.09 at the blade tip. A nose fairing was added to the B2a-fan by Louw *et al.* (2012) to provide more accurate modelling for his comparison with CFD data at low flow rates.

The M-fan was designed by Wilkinson (2017) according to the parameters put out by the MinWaterCSP project. The NASA LS 0413 aerofoil of McGhee and Beasley (1976) was used as a basis with an optimized camber profile along its blade span with a maximum of 3.5 % camber at the hub and 0.5 % at its tip.

The fan has a flat hub and root seals. The M-fan makes use of an optimized outlet velocity profile in an attempt to minimize kinetic energy flux at the fan exit. Other factors which distinguish it from the B2a-fan are its pressure and volume flow rate, inlet velocity vector and chord lengths. The dimensions and fan design specifications of the M-fan and B2a-fan are shown in table A.1 and figure A.1.

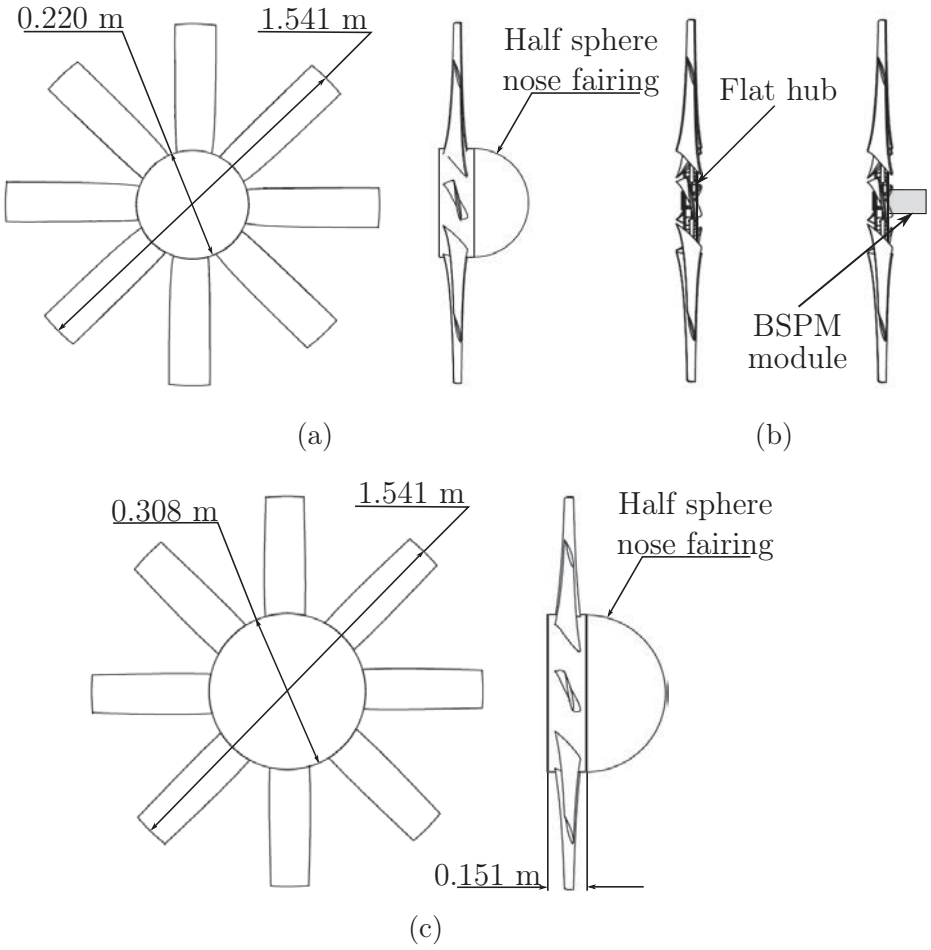

Figure A.1: Schematic of the (a) M-fan numerical model (b) M-fan experimenal fan and (c) B2a-fan experimental and numerical model, all with a tip gap of 3 mm

Table A.1: Design specifications of the M-fan and B2a-fan

Parameter	**M-Fan**	**B2a-fan**
Fan static pressure (Δp_{Fs})	115.2 Pa	210 Pa
Volumetric flow rate ($\dot{V}$)	14.4 m^3/s	16 m^3/s
Rotational speed (N)	722 rpm	750 rpm
Tip clearence (c_t)	0 mm	3 mm
Stagger angle (ζ)	56°	59°

A.2 M-Fan BSPM blade

Two different methods to construct the BSPM blades were tested as discussed previously in chapter 4.3. The BSPM blade used for the experimental results was already detailed in section 4.3. The second alternative method is explained in the following section, along with the description of its catastrophic failure during experimental testing. Both methods used carbon fibre blade skins and a summary of the method is given below.

A.2.1 Carbon fibre blade skins

The M-Fan fan blade is manufactured using a carbon fibre hand layup. Two moulds are needed: one for the suction side and the other for the pressure side of the fan. The two carbon fibre blade skins are then combined to form one complete blade. One blade is manufactured with pressure measurement taps on the suction side and another blade with taps on the pressure side. The blade skin with no pressure taps will be explained first, then followed by its partner blade skin with pressure measurement taps.

A waxed based releasing agent is firstly applied to the mould to prevent the carbon fibre skins from sticking, allowing an easy removal after the layup has cured. A layer of epoxy is then applied followed by a layer of carbon fibre. This process is repeated until there are five carbon fibre layers. Another layer of epoxy resin is applied, followed by a layer of Peelply (a tightly woven nylon fabric) which can be peeled off post cure, allowing for a smooth finish of the blade side. This is followed by a layer of breather fabric to provide a continuous air path for suction on the material. A final layer of vacuum bag is attached to a vacuum pipe. This sucks the layup onto the mould (shape) while the resin is entrained and evenly distributed through the carbon fibre layers. This allows the carbon fibre to cure tightly onto one another. Once this has cured the blade skin is taken out of the mould, deburred and cleaned.

Figure A.2: Aluminium blade profiles locating pressure channel positions along the blade span

A.2.2 Alternative blade design

Aluminium blade profiles with the locations of the pressure taps are placed along the five radial positions of the blade. Styrofoam strips were then glued along the marked pressure taps. A layer of epoxy adhesive is placed between and on top of the Styrofoam strips to insulate them from one another. The process then follows the steps as explained in the previous section. A hole is drilled into each channel at the bottom of the blade and a rubber nipple is placed inside. This is then connected to a 3 mm diameter brass tube (wall thickness 0.225 mm) which is bent and placed through the shaft. A hollow carbon fibre rod is placed onto the skin. At the end of the rod there is a stub with various holes indicating the blade angle.

Another hole is drilled at the top end of the blade into the channel. A dissolving agent is run through the channels causing the Styrofoam in the channels to dissolve and run out of the blade. This creates a hollow channel in which the induced pressure can be measured by the pressure sensors. The hole at the tip of the blade is then covered again with an epoxy adhesive.

The two blades are then glued together. This is then placed into one of the moulds of which a corner will be used as a reference location for the BSPM locations. A paper print out of the blade along with the pressure tap holes is placed on top of each side. The holes are then marked and carefully drilled by hand perpendicular to the localized profile gradient. Five aluminium blade profiles with BSPM hole locations are cut using a waterjet cutting system. These are located at their respective blade span inside the blade skin and used to mark the locations of the hollow pressure tap channels as shown in figure A.2. A paper print out of the blade surface with the pressure tap locations is used to locate the pressure tap holes onto carbon fibre blade surface.

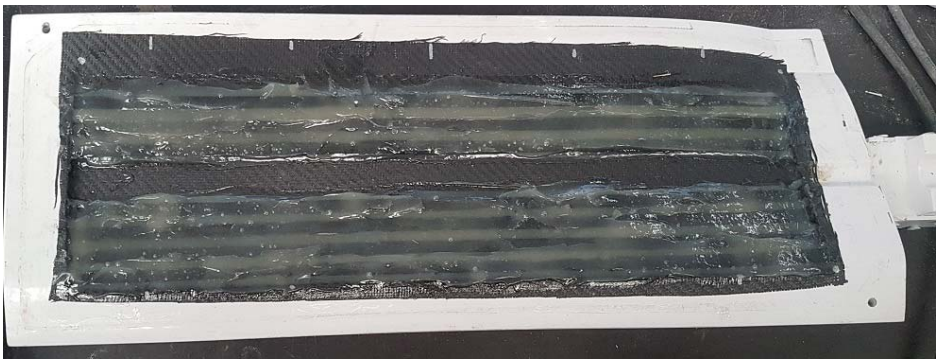

(a)

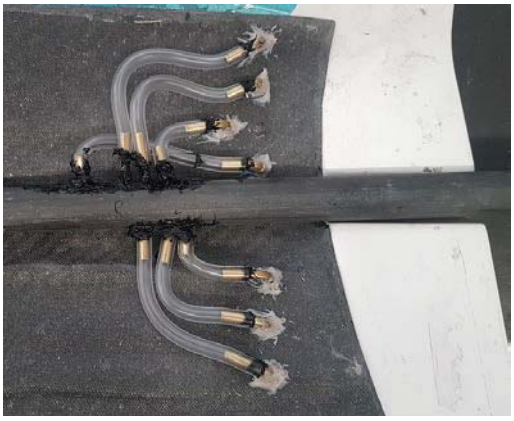

(b)

(c)

(d)

Figure A.3: Manufacturing process of the alternative M-fan: (a) epoxy adhesive ontop of styrofoam strips (b) connection between blade channels and brass rods (c) pressure tap holes (d) pressure tap tubes through fan shaft

(a)

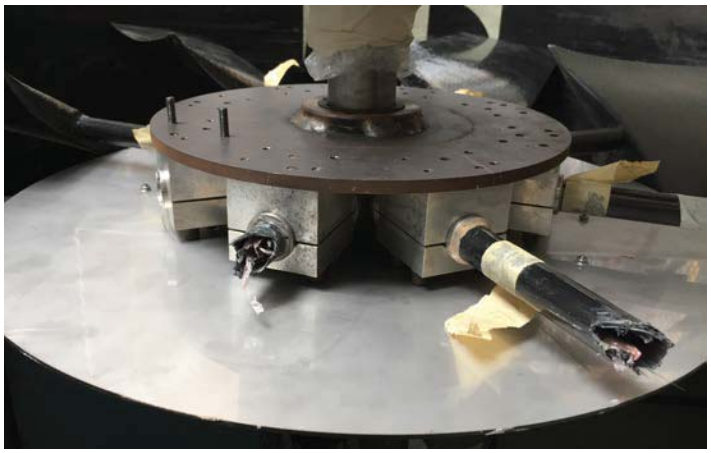

(b)

Figure A.4: Schematic of the (a) M-fan numerical model (b) M-fan experimenal fan and (c) B2a-fan experimental and numerical model, all with a tip gap of 3 mm

A.2.3 Fan failure

Experimental testing of the alternative BSPM blades resulted in catastrophic failure during a test run. Figure A.4 shows the fan hub and broken shafts.

An investigation was conducted after the fan was brought to halt. The radial forces exerted on the carbon fibre shaft pulled it out of the aluminium housing. The fan then struck and destroyed the other blades. The mass of the BSPM

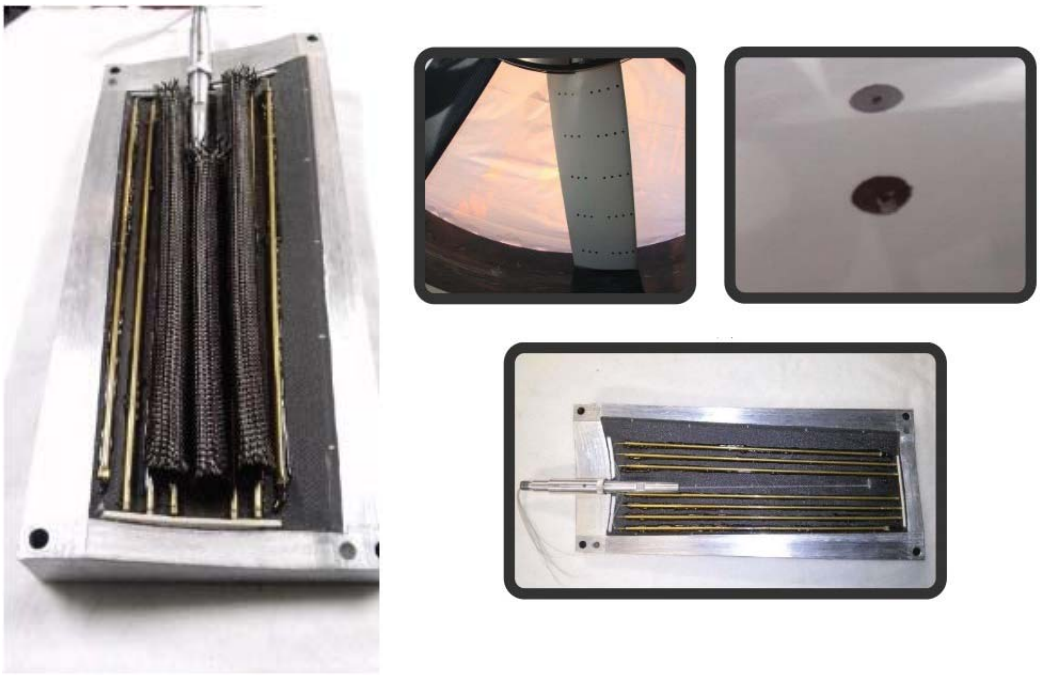

Figure A.5: B2a-fan for BSPM construction (Louw, 2015)

blades were too high due to the epoxy that was required for the manufacturing of the blade channels. The method was therefore not repeated again and should not be considered for blade surface pressure measurement, especially for the full scale BSPM M-fan.

A.3 B2a-fan BSPM blade

Two fibre glass B2a-fan blades are used to conduct BSPM tests. Louw (2015) designed and conducted BSPM on the blades. The placement of the pressure taps are located at the same dimensionless locations across the blade as the M-fan and there is an additional pressure tap at the chord location x/ch=0.35 as initially intended with the M-Fan. Brass tubes are located inside the blade and serve as air channels. A brass reducer is used to connect the channels to silicone tubes which go through the blade . More details on the blade, fan hub and nose fairing can be found in Louw (2015).

Appendix B

Numerical model

This section details the turbulence model used in chapter 3. The Reynolds-averaged Navies Stokes (RANS) equations are firstly derived, after which the Realizable k-ε model is described. This is followed by a description of the two wall functions used in the numerical model for the B2a-fan and M-fan.

The last part of this section details the mesh sensitivity study conducted on the M-Fan numerical model (P3DM).

B.1 RANS modelling

The fundamental flow equations for an incompressible Newtonian fluid are defined as:

Continuity :

$$\frac{\partial u_i}{\partial x_i} = 0 \tag{B.1}$$

Momentum :

$$\frac{\partial}{\partial t}(\rho u_i) + \frac{\partial}{\partial x_j}(\rho u_i u_j) = -\frac{\partial p}{\partial x_i} + \frac{\partial}{\partial x_j}(2\mu s_{ij}) \tag{B.2}$$

where s_{ij} is the strain rate tensor, defined as:

$$s_{ij} = \frac{1}{2}(\frac{\partial u_i}{\partial x_j} + \frac{\partial u_j}{\partial x_i}) \tag{B.3}$$

The Reynolds-averaged Navies Stokes (RANS) equation is derived by substituting each instantaneous quantity with a time-averaged (mean) and fluctuating component defined as:

$$\begin{aligned} u_i &= U_i + u_i', \\ p &= P + p', \\ \phi &= \Phi + \Phi' \end{aligned} \tag{B.4}$$

where the mean component is denoted by capitals as follows:

$$\begin{aligned} \overline{u_i} &= U_i, \\ \overline{p} &= P \end{aligned} \tag{B.5}$$

and the mean of individual fluctuating components conforms to:

$$\begin{aligned} \overline{u_i'} &= 0, \\ \overline{p_i'} &= 0 \end{aligned} \tag{B.6}$$

Substituting the above equations into the fundamental flow equations (B.1 and B.2) results in the RANS equations shown below. It must be noted that the product of the fluctuating components is not zero.

Continuity :

$$\frac{\partial \rho U_i}{\partial x_i} = 0 \tag{B.7}$$

Momentum :

$$\frac{\partial}{\partial t}(\rho U_i) + \frac{\partial}{\partial x_j}(\rho U_i U_j) = -\frac{\partial P}{\partial x_i} + \frac{\partial}{\partial x_j}(2\mu S_{ij}) - \frac{\partial}{\partial x_j}(\rho \overline{u_i' u_j'}) \tag{B.8}$$

where S_{ij} is the mean strain rate tensor, defined as:

$$S_{ij} = \frac{1}{2}\left(\frac{\partial U_i}{\partial x_j} + \frac{\partial U_j}{\partial x_i}\right) \tag{B.9}$$

The extra turbulent stresses $(\overline{u_i' u_j'})$ introduced into the momentum equation are known as Reynolds stresses. They consist of three normal stresses and three shear stresses. Using the commutative laws associated with the fluctuating components we are left with six unknown components . These need to be modelled to provide closure of equation Turbulence models are used to provide

mathematical closure of these unknown variables. The Boussinesq approximation assumes that the Reynolds stresses are proportional to the mean rates of deformation and is defined as:

$$(\rho\overline{u_i'u_j'}) = 2\mu_t S_{ij} - \frac{2}{3}\rho k\delta_{ij} \tag{B.10}$$

where μ_t is the tubulent or eddy viscosity.

δ_{ij} is the Kronecker delta which states that:

$$\begin{aligned} \delta_{ij} &= 0 \quad \text{if} \quad i \neq j \\ \delta_{ij} &= 0 \quad \text{if} \quad i = j \end{aligned} \tag{B.11}$$

and k is the kinetic energy per unit mass defined as:

$$\frac{1}{2}(\overline{u'^2} + \overline{v'^2} + \overline{j'^2}) \tag{B.12}$$

The turbulent viscosity can be solved using various transport equations, one of them being the realizable k-ε model. It models the turbulent viscosity by using two additional transport equations: the turbulence kinetic energy (k) and dissipation rate (ε).

B.2 Realizable *k-ε* model

A summary of the realizable k-ε model is provided in this section. More detail of the model derivation can be found in Shih *et al.* (1995) and the application of which in the ANSYS Fluent theory guide Fluent. The turbulent kinetic energy (k) and turbulent dissipation rate (ε) of the realizable k-ε model are defined as:

Turbulent kinetic energy :

$$\frac{\partial}{\partial t}(\rho k) + \frac{\partial}{\partial x_j}(\rho k U_j) = \frac{\partial}{\partial x_j}\left[\left(\mu + \frac{\mu_t}{\sigma_k}\right)\frac{\partial k}{\partial x_j}\right] + G_k + G_b - \rho\epsilon - Y_M - S_k \tag{B.13}$$

Turbulent dissipation rate

$$\frac{\partial}{\partial t}(\rho \epsilon) + \frac{\partial}{\partial x_j}(\rho \epsilon U_j) = \frac{\partial}{\partial x_j}\left[\left(\mu + \frac{\mu_t}{\sigma_\epsilon}\right)\frac{\partial \epsilon}{\partial x_j}\right] + \rho G_1 S_\epsilon - \rho C_2 \frac{\epsilon^2}{k + \sqrt{\nu\epsilon}} + C_{1\epsilon}\frac{\epsilon}{k} C_{3\epsilon} G_b + S_\epsilon \tag{B.14}$$

where

$$C_1 = \max\left[0.43, \frac{\eta}{\eta+5}\right], \quad \eta = S\frac{k}{\epsilon}, \quad S = \sqrt{2S_{ij}S_{ij}} \tag{B.15}$$

G_k represents the generation of turbulent kinetic energy due to the mean velocity gradients and is defined as:

$$G_k = \mu_t S^2 \tag{B.16}$$

G_b is the generation of turbulence kinetic energy due to buoyancy and is defined as:

$$G_b = \beta g_i \frac{\mu_t}{Pr_t}\frac{\partial \rho}{\partial x_i} \tag{B.17}$$

where g_i is the gravitational component in the i-direction and Pr_t is the (constant) turbulent Prandtl number, Pr_t=0.85. The thermal expansion coefficient, β is defined as:

$$\beta = -\frac{1}{\rho}\left(\frac{\partial \rho}{\partial T}\right) \tag{B.18}$$

Y_M represents the effect of incompressibility but is neglected for incompressible flows.

The constants for the above equations are defined as:

$$C_{1\epsilon} = 1.44, \quad C_2 = 1.9, \quad \sigma_k = 1.0, \quad \sigma_\epsilon = 1.2 \tag{B.19}$$

The effect of buoyancy on the turbulent dissipation rate $C_{3\epsilon}$ is normally a constant value but Fluent® defines it as:

$$C_{3\epsilon} = \tanh\left|\frac{v}{u}\right| \tag{B.20}$$

As in the other (ε), the turbulent viscosity is defined as:

$$\mu_t = \rho C_{mu}\frac{k^2}{\epsilon} \tag{B.21}$$

The realizable (ε) model however differs from the standard (ε) in that C_μ is no longer a constant but is defined as:

$$C_\mu = \frac{1}{A_0 + A_S\frac{kU^*}{\epsilon}} \tag{B.22}$$

where

$$U^* = \sqrt{S_{ij}S_{ij} + \tilde{\Omega}_{ij}\tilde{\Omega}_{ij}} \tag{B.23}$$

and

$$\begin{aligned} \tilde{\Omega}_{ij} &= \Omega_{ij} - 2\epsilon_{ijk}\omega k \\ \Omega_{ij} &= \overline{\Omega_{ij}} - \epsilon_{ijk}\omega k \end{aligned} \tag{B.24}$$

The mean rate of rotation in a moving reference frame with an angular velocity of ω_k is defined as:

$$\overline{\Omega}_{ij} = \frac{1}{2}\left(\frac{\partial U_i}{\partial x_j}\frac{\partial U_j}{\partial x_i}\right) \tag{B.25}$$

The model constants are defined as:

$$A_0 = 4.04, \quad A_S = \sqrt{6}\cos\phi \tag{B.26}$$

where

$$\phi = \frac{1}{3}\cos^{-1}(\sqrt{6}W), \quad W = \frac{S_{ij}S_{jk}S_{ki}}{\tilde{S}^3}, \quad \tilde{S} = \sqrt{S_{ij}S_{ij}} \tag{B.27}$$

B.3 Wall functions

Wall functions are used to model the viscosity-affected region between the wall and the fully turbulent region. This section provides a brief description of the standard wall function used in the B2a-fan and enhanced wall function used in the M-fan. More detail concerning the wall functions' implementation can be found in the ANSYS Fluent theory guide (ANSYS Fluent Inc., 2017). Figure B.1 shows the various regions for the near wall region plotted on a semi-log scale.

The viscous sub-layer is the thin fluid layer ($y^+ < 5$) in contact with the wall. The fluid behaviour is mostly laminar and dominated by viscous effects. The buffer layer is a transitional region which lies between $5 < y^+ < 30$. The log-law layer is outside the buffer layer and and this is where turbulent stresses dominate over viscous stresses. The velocity profiles of the viscous sub-layer and turbulent region are given below in dimensionless form:

Viscous sub−layer

$$u^+ = y^+, \qquad y^+ < 5 \tag{B.28}$$

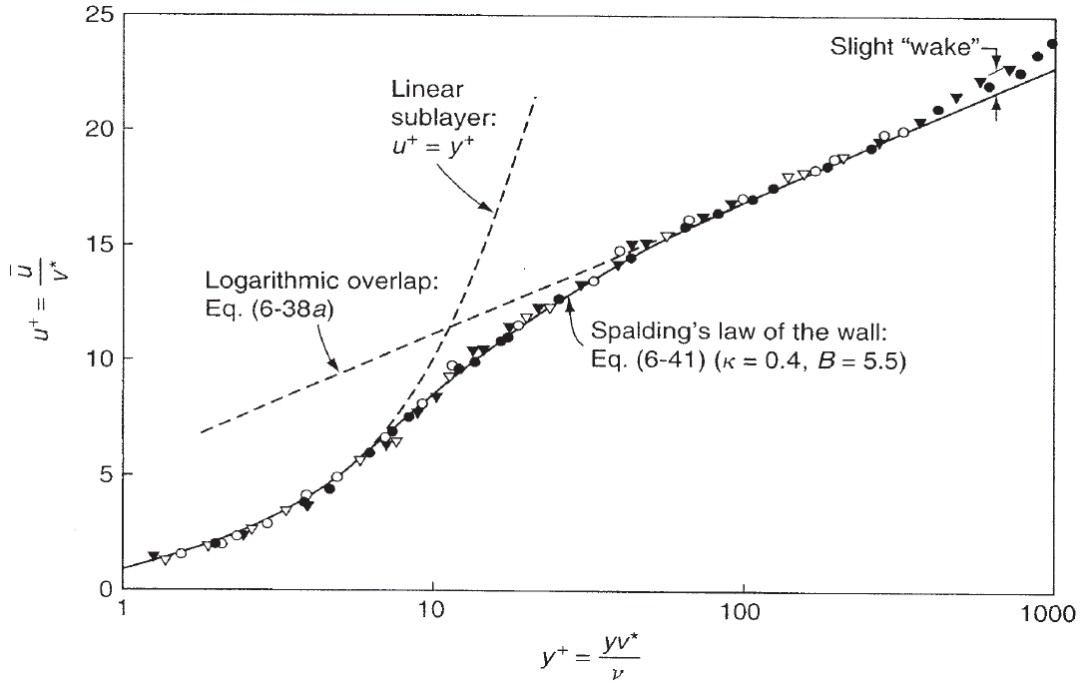

Figure B.1: Flow regions at the near wall region (White, 2006)

Log law layer :

$$u^+ = \frac{1}{\kappa} \ln y^+ + B, \qquad 30 < y^+ < 300 \tag{B.29}$$

where y^+ and u^+ are the dimensionless velocity and wall normal distance defined by

$$y^+ = \frac{y u_\tau}{v}, \quad u^+ = \frac{u}{u_\tau} \tag{B.30}$$

and u_τ is a reference velocity based in the wall shear stress (no-slip condition) given as

$$u_\tau = \sqrt{\frac{\tau_w}{\rho}}, \tag{B.31}$$

In the above equation B.29, κ is the von Kármaán constant and B is an integration constant.

The standard wall function of Launder and Spalding (1974) extends the log-law curve throughout the entire near wall region range until it intercepts the y-axis. ANSYS Fluent® differs slightly from this in that it extends both the viscous sublayer and log-law curve until they intersect at a y^+ value of 11.225

ANSYS Fluent Inc. (2017). Both methods neglect to model the buffer layer and it is therefore not included in the model. The modelling of the laminar sublayer should only be seen as a means to complete the wall function for localized near wall mesh regions with a small y^+ value. ANSYS Fluent Inc. (2017) suggests a y^+ value above 30 so that the solution can be modelled using only the log law. The viscous sub-layer and buffer layer have a much steeper slope (transition) in turbulent flow when compared to laminar flow. This region can often be neglected due to its small influence on the solution and the standard wall function is therefore more applicable in highly turbulent flows.

The enhanced wall function uses a blending function to model the buffer region and provides a model for flow between the two other regions. Equations B.28 and B.29 are used to solve the viscous and log-law layer for their respective y^+ regions. The enhanced wall function can therefore model all y^+ values. Its ability to model fine meshes more accurately at low y^+ values makes it more favourable than the standard wall function for fine meshes.

B.4 Mesh dependency study

This section details the mesh sensitivity study for modelling the M-fan in the BS 848, test facility as described in chapter 3. It should be noted that the realizable k-ϵ model with enhanced wall function requires a y^+ value in the range of $0 < y^+ < 5$ at the wall boundaries. The mesh sizing (density) of each subdomain of the P3DM are investigated, resulting in an optimal (economical) choice of mesh size. The blade subdomain is first investigated because the other two subdomain interfaces are dependent on this outcome.

The mesh density was progressively increased until there was a satisfactory convergence in solution. The total to static pressure rise ($P_{s,tot}$) as well as fan static efficiency (η_{ts}) are used as a criteria for mesh accuracy in each subdomain.

B.4.1 Blade subdomain

An annulus model is used to investigate the blade subdomain. This allows for a faster converging answer while only focusing on the flow through the blade domain. Wilkinson (2017) found that after a length of 2 m, the inlet and outlet subdomains length did not significantly inflence the outcome. The fan was initially modelled without a tip clearance as the main focus is on

the entire blade span. The mesh quality guidelines in ANSYS Turbogrid® ((ANSYS Fluent Inc., 2017)) were all satisfied.

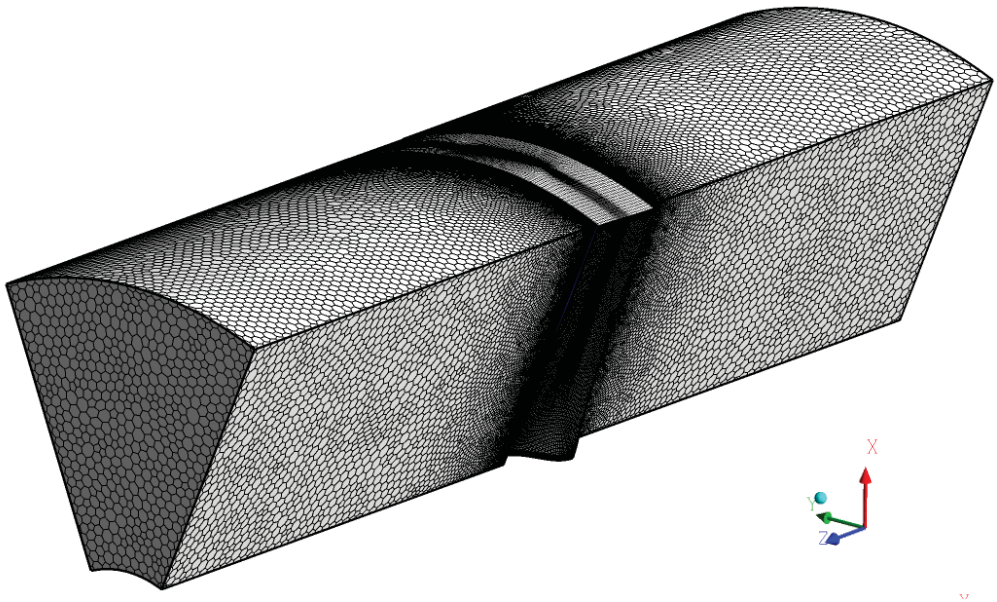

Figure B.2: Annular domain used for the mesh dependency study of the blade subdomain

Table B.1: Blade subdomain mesh dependency investigation with 0 mm tip gap

Mesh	**No. of elements**	$\boldsymbol{P_{s,tot}}$ **(Pa)**	$\boldsymbol{\eta_{ts}}$ **(%)**
1	2036320	107.98	55.47
2	2251452	107.72	55.51
3	2492689	106.87	55.59

It can be seen that the mesh density investigated in this study does not have a significant influence on the total to static pressure rise and fan static efficiency values. Mesh 1 will therefore be chosed for the simulation of the blade sub domain.

The tip gap ($c_t = 3$ mm) mesh density was investigated by varying the amount of spanwise element layers between the tip and the shroud. A minimum of 40 layers was required to maintain good mesh quality. The results from table B.2 show that there is little diffference between the two tip gaps and the smallest one is chosen for computational efficiency.

Table B.2: Tip gap mesh dependency study ($c_t = 3$ mm)

Mesh	No. of layers	$P_{s,tot}$ (Pa)	η_{ts} (%)
1	40	96.24	50.78
2	60	96.24	50.78

B.4.2 Inlet and outlet subdomain

The inlet domain outflow boundary required a mesh density higher than the blade subdomain inlet boundary as explained in section 3.1.1. Each subdomain consists of three mesh sections of varying mesh densities to account for their respective velocity gradients. The section closest to the blade domain is investigated first while the other zones have their most dense mesh setting. The first zone has the nose fairing which requires a very fine mesh at the wall boundary to adhere to the enhanced wall function requirements ($0 < y^+ < 5$). Once the first zone investigation is complete, the middle and then the last zone is investigated and lastly the third Zone. The results of the inlet subdomain mesh independence study is shown in table B.3.

Table B.3: Mesh dependency study on inlet subdomain

Zone	No. of elements	$P_{s,tot}$ (Pa)	η_{ts} (%)
1	1467949	95.47	50.06
	1761538	95.47	50.06
2	117777	95.47	50.06
	151617	95.57	50.12
	180341	95.61	50.23
3	10935	95.47	50.06
	13011	95.56	50.12
	15476	95.71	50.29

The outlet domain has an inflow boundary which is of similar density to the blade subdomain outlet. The same approach was used as for the inlet subdomain, where the zone closest to the blade subdomain is investigated first and the other zones have their highest mesh density. The inlet boundary of the outlet subdomain contains a mesh density similar to that of the blade subdomain outlet boundary. The results of the outlet subdomain mesh independence study are shown in table B.4.

Table B.4: Mesh dependency study on outlet subdomain

Zone	No. of elements	$P_{s,tot}$ (Pa)	η_{ts} (%)
1	1351369	95.47	50.06
	1702428	95.44	50.09
2	81857	95.47	50.06
	102780	95.51	50.10
	123228	95.77	50.35
3	226509	95.47	50.06
	267043	95.69	50.24
	323628	95.81	50.49

Both the tables B.3 and B.4 clearly show that there is a small change in fan performance with increasing mesh densities. Both subdomains are dependent on the blade subdomain boundary cells and small y^+ requirement of the enhanced wall function. This already makes the subdomains require a very fine mesh while also adhering to good cell proportionality and expansion from one zone to another. The least dense (economical) zones are chosen for their respective subdomains.

B.5 BSPM comparison of B2a-fan and M-fan

The BSPM of the numerically simluated M-fan and B2a-fan are compared on the same set of axis as shown in figure B.3. The differences between the blades are described in Appendix A. From the figures, it is evident that blade pressure side of the B2a-fan and M-fan have similar pressure distributions. The blade suction side of the B2a-fan is however much lower than the M-fan and results in an overall higher pressure difference.

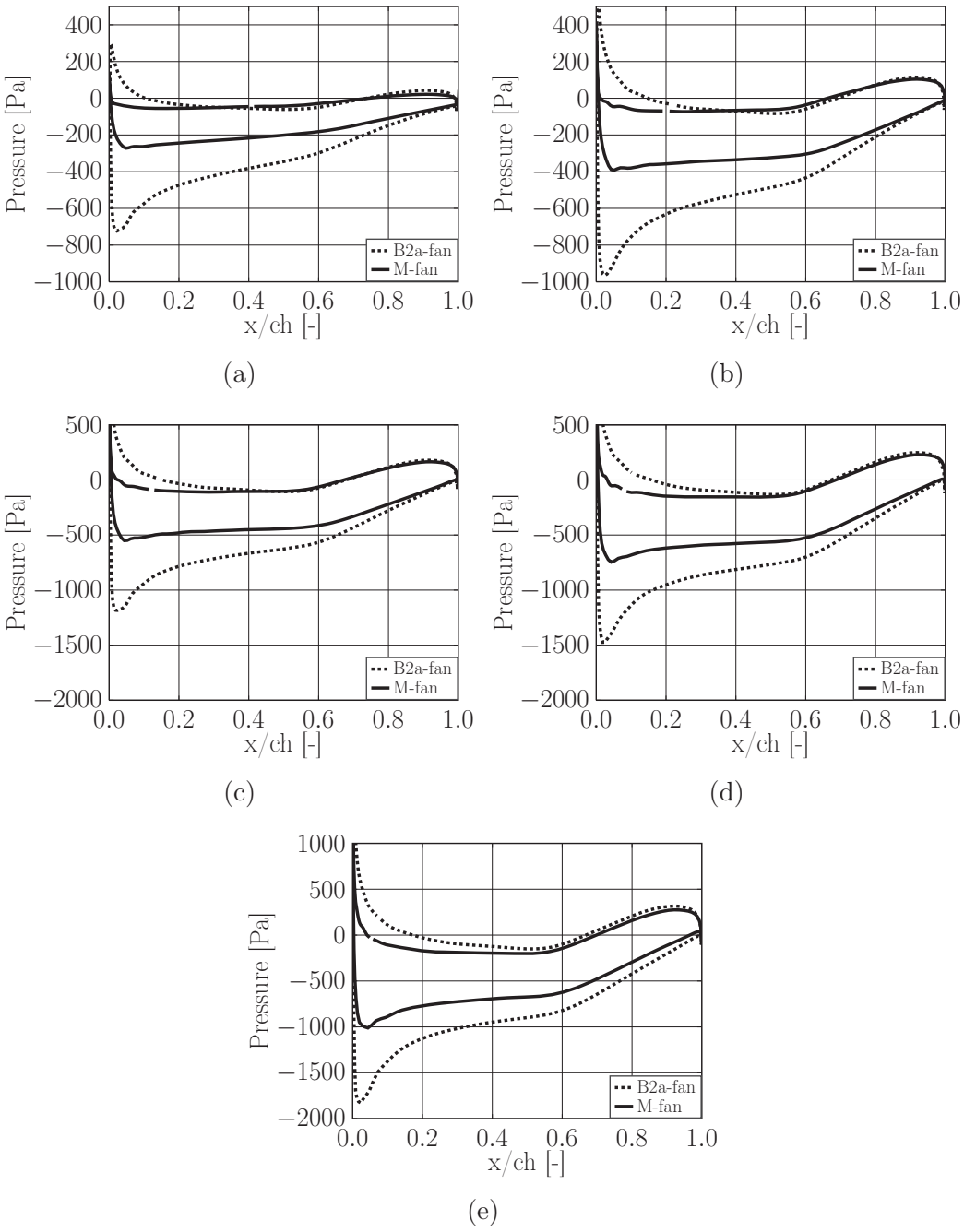

Figure B.3: Numerically simulated blade surface pressure measurements of the B2a-fan and M-fan at their design operating speed at the span length of s_b = (a) 0.1, (b) 0.3, (c) 0.5, (d) 0.7, and (e) 0.9

Appendix C

Experimental testing

This section details the calibration and derivation of the characteristic tests and blade surface pressure mesurements conducted at the BS 848, type A test facility at Stellenbosch University. A definition of the statistical analysis tools used throughout this thesis is briefly discussed.

C.1 Error measurement analysis

Statistical analysis are conducted on data sets using standard deviation (σ) and relative standard deviation (RSD). These are defined as follows:

$$\sigma = \sqrt{\frac{1}{n}\sum_{i=1}^{n}(x_i - \mu)^2} \tag{C.1}$$

$$RSD = \frac{\sigma}{\mu} \times 100 \tag{C.2}$$

where n is the size of the population, x_i the specific value of the data point and μ the arithemtic mean of the data points.

The correlation between different data sets can be analysed using the root mean square error (RMSE) and the Pearson correlation (R_p), which are defined as follows:

$$RMSE = \sqrt{\frac{\sum_{i=1}^{n}(x_i - y_i)^2}{n}} \tag{C.3}$$

$$R_p = \frac{\sum[(x_i - \bar{x})(y_i - \bar{y})]}{\sqrt{\sum(x_i - \bar{x})^2 \sum(y_i - \bar{y})^2}} \tag{C.4}$$

where y represents a holding value for the second set of data points. In many cases, the average of the various RMSE and R_p are used in evaluating a string of data sets (e.g. BSPM analyses).

C.2 Calibration of BS 848 measuring equipment

The calibration of the equipment used to measure pressure, torque and speed at the BS 848, type A test facility is described in the sections that follow. Calibration was conducted before experimental testing of the B2a-fan and M-fan respectively.

C.2.1 Pressure transducers

Two HBM PD1 pressure transducers are located inside the test facility's control room. Each pressure transducer was individually calibrated using a Betz water column manometer (accuracy $\pm$ 1 Pa). A t-connection is used to fit one side of the pressure transducer to the manometer and connection side to a ball valve as shown in figure C.1. The other side of the pressure transducer is open to the atmosphere.

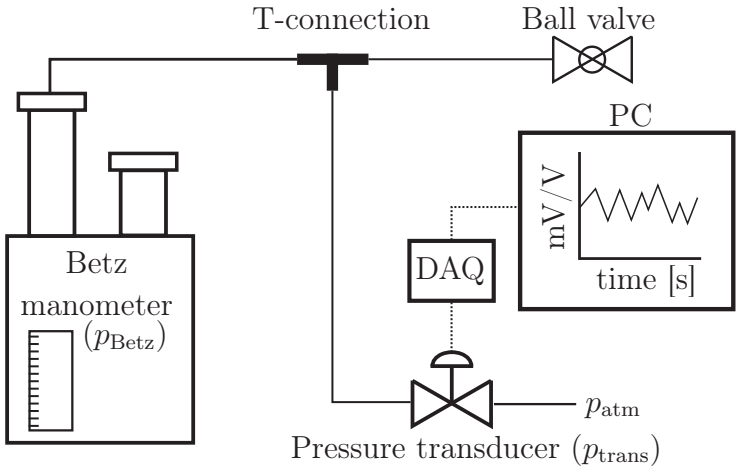

Figure C.1: Experimental setup for pressure transducer calibration

The Betz manometer is firstly zeroed against the atmospheric pressure, after which a zero pressure reading is recorded. An initial suction pressure is then

applied and pressure released back into the system at regular intervals. Each pressure interval is allowed to settle during which any leaks can be detected by monitoring the Betz manometer. The data is then recorded for 10 s during which any irregularities (e.g. noise or drift) are monitored. The data is averaged and the process is repeated for the next pressure. Three calibrations sets were conducted at various pressure, individual sets averaged and used for processing the recorded voltage to its corresponding pressure. The figures below show a typical recording (500 Pa) and calibration curve of the pressure transducer.

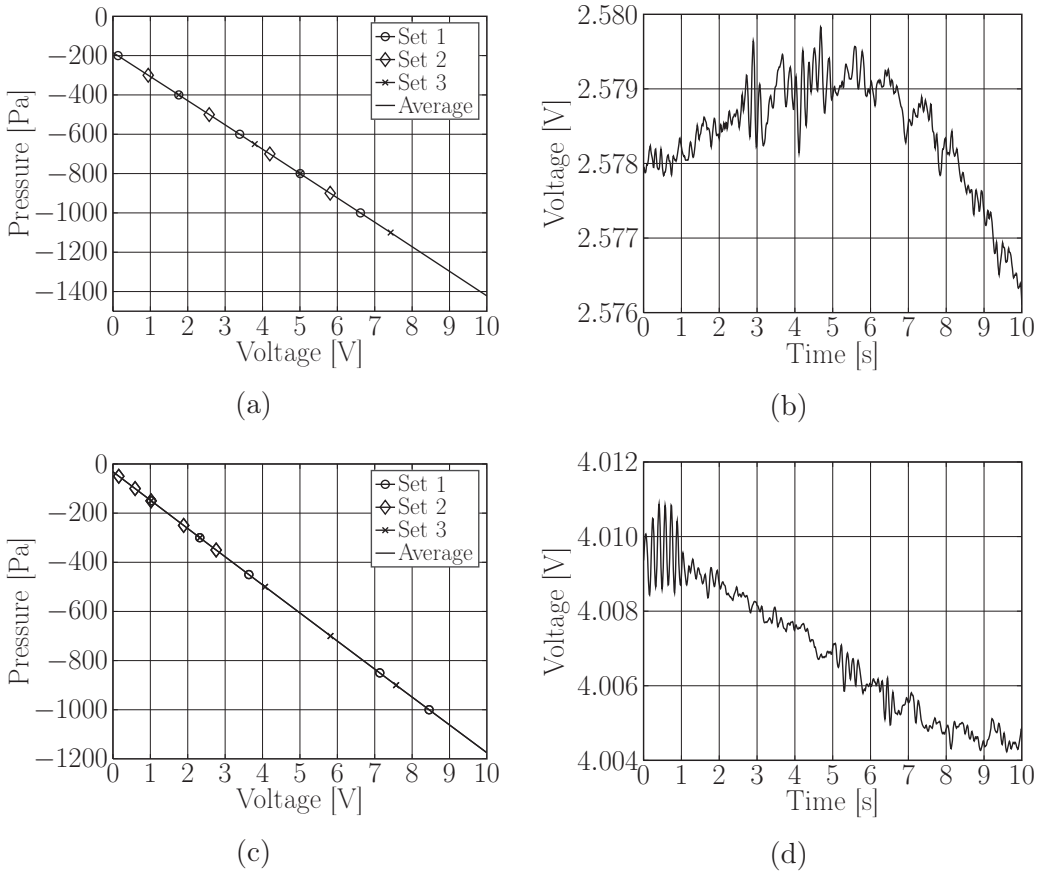

Figure C.2: Calibration curve and typical calibration recording of (a), (b) pressure transducer 1 and (c), (d) pressure transducer 2

C.2.2 Torque transducer

The HBM T22 torque transducer was calibrated using a static cantilever setup shown in figure C.3a to C.3c. The shaft on the drive side is securely fixed with

two chains so that it cannot rotate. The fan must be removed so that a cantilever arm can be placed on the shaft where the fan is normally located. The cantilever arm is balanced when there is no extra mass placed onto it. A digital protractor (accuracy $\pm 1°$) is used to measure the cantilever arm at its horizontal position, after which it is tightened onto the fan shaft. A rotational force is added onto the shaft by adding a known mass on the one side of the cantilever arm. The angle at which the arm rotates is then recorded using a digital protractor. The torque applied on the shaft is then calculated as shown in figure C.3c. A measurement is recorded for 10 s. A typical recording (-500 Pa) and calibrated trend line is shown in figure C.4.

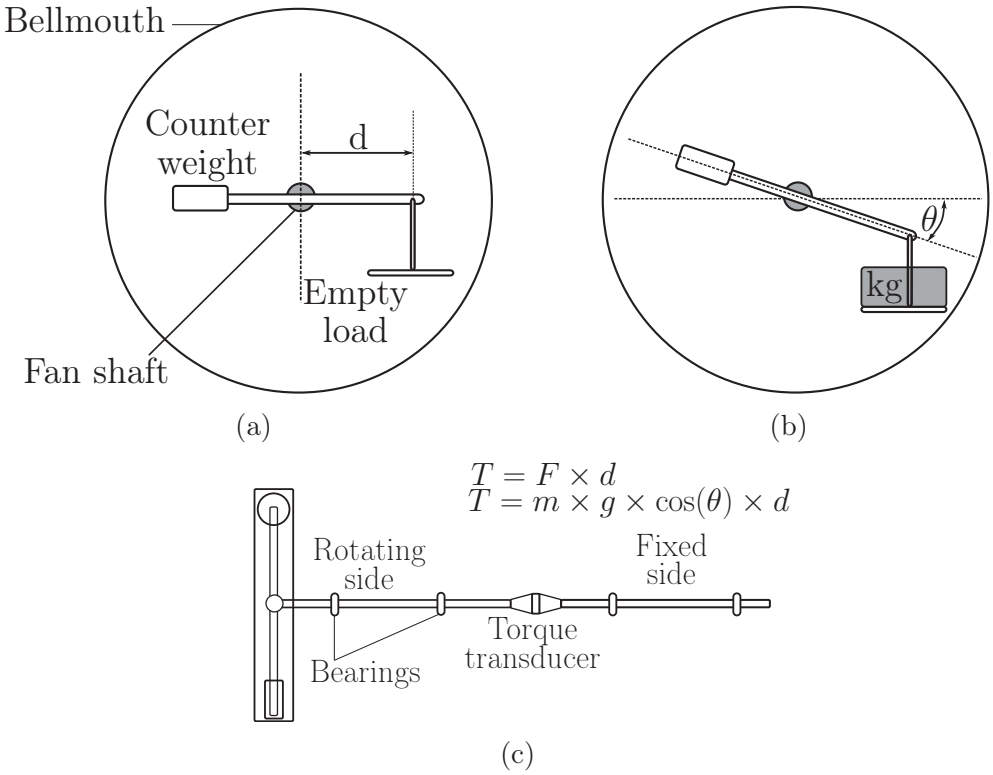

Figure C.3: Experimental setup for torque transducer calibration

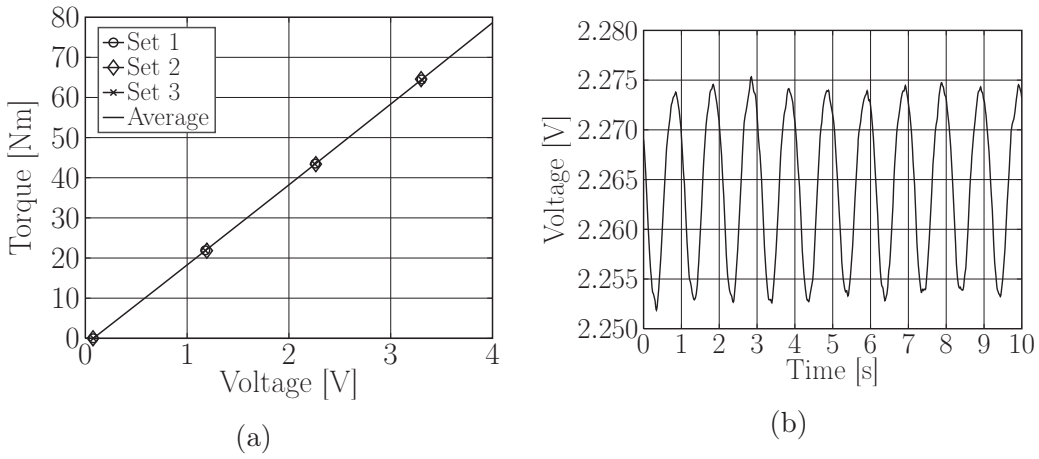

Figure C.4: (a) calibration curve and (b) typical calibration recording of torque tansducer

C.2.3 Fan speed

The rotational speed of the shaft was calibrated using a hand held stroboscope. The fan was firstly removed from the shaft. A small strip of reflective material is stuck from the shaft centre to the outer edge. A reference station with a horizontal reflective material strip is placed next to the shaft. The calibration was conducted early in the morning when the plenum chamber was dark. The tachometer must be adjusted so that both reflective strips seem stationary to one another i.e. the rotational speed is measured by the tachometer when the two strips match up and do not move. The calibration was conducted for 10 s to ensure that the frequency was correct. The results are shown in figure C.5.

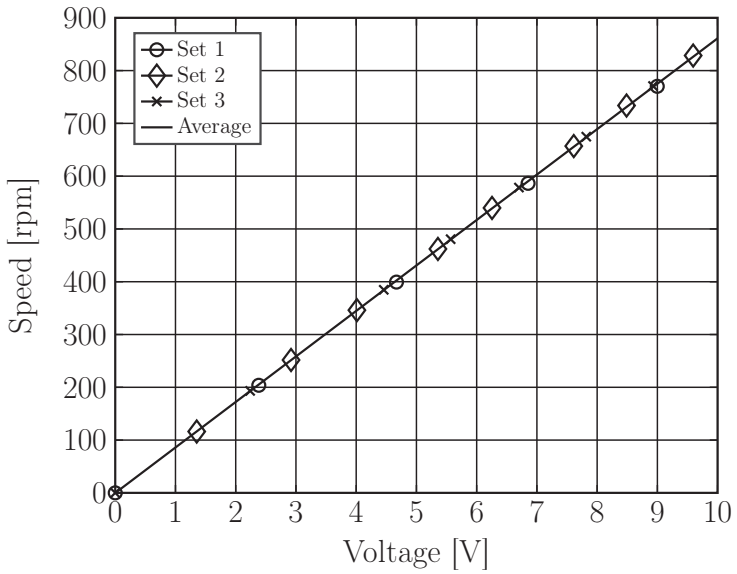

Figure C.5: Calibration curve for shaft speed

C.3 BS 848 calculation

The procedure for calculating the fan performance characteristic curves from the measured data at the BS 848, type A test facility is detailed in this section.

The average of the temperature (T_{a}) and pressure (p_{atm}) recorded at the start and end of the test set is used for all data processing as shown in equation C.5 and C.6 . This is justified by small deviations between the start and end of a test set which subsequently does not significantly affect the results.

$$T_{\mathrm{a}} = \frac{T_{\mathrm{a,start}} + T_{\mathrm{a,end}}}{2} \tag{C.5}$$

$$p_{\mathrm{atm}} = \frac{p_{\mathrm{atm,start}} + p_{\mathrm{atm,end}}}{2} \tag{C.6}$$

The recorded torque (T_{shaft}), speed (ω_{shaft}) and pressure ($\Delta p_{\mathrm{s,bell}}$, $\Delta p_{\mathrm{s,plen}}$) values are time averaged over each respective recording, as discussed in section 4.2. A zero measurement is recorded at the start and end of each test run for the respective measurement station. The drift during a test run is significant and is calculated by linear interpolation between the initial start zero value and end zero valueas shown in eqn. C.7.

$$drift = data_{zero1} + \left(\frac{i}{n_{tot}}\right)(data_{zero2} - data_{zero1}) \tag{C.7}$$

The start and end zero measurement are referred to as $data_{zero1}$ and $data_{zero2}$, and i the specific test number in the total number of measurements, n_{tot} (excluding the zero measurements). The corrected value is then obtained by subtracting the drift from the specific averaged recorded value ($data_{recorded,i}$) as shown in eqn.C.8.

$$data_{corrected} = data_{recorded,i} - drift \tag{C.8}$$

The ambient denisty for the test set is calculated by:

$$\rho_{\text{atm}} = \frac{p_{\text{atm}}}{RT_{\text{atm}}} \tag{C.9}$$

where p_{atm} is the atmosheric pressure, R is the specific gas constant for air and T_{atm} is the atmospheric temperature which is equal to T_{a} (see section 4.2).

The mass flow rate ($\dot{m}$) through the test facility is calculated by:

$$\dot{m} = \text{K}_{\text{n}} \frac{\pi d_{bell}^2}{4} \sqrt{2\rho_{\text{atm}} \Delta p_{\text{bell}}} \tag{C.10}$$

where the bellmouth diameter is $d_{bell} = 1.008$ m and the test facility loss coefficient is $\text{K}_{\text{n}} = 0.9082$ (Venter, 1990).

The air density inside the settling (plenum) chamber is adjusted relative to the atmospheric pressure as shown in eqn. C.11.

$$\rho_{\text{plen}} = \frac{p_{\text{atm}} - \Delta p_{\text{s,plen}}}{RT_{\text{plen}}} \tag{C.11}$$

The dynamic pressure can now be calclated using the mass flow rate and plenum density as follows:

$$\begin{aligned} p_{\text{d,plen}} &= \frac{1}{2}\rho_{\text{plen}} {V_{\text{plen}}}^2 \\ &= \frac{1}{2}\rho_{\text{plen}} \left(\frac{\dot{m}}{\rho_{\text{plen}} A_{\text{plen}}} \right)^2 \\ &= \frac{\dot{m}^2}{2\rho_{\text{plen}} {A_{\text{plen}}}^2} \end{aligned} \tag{C.12}$$

where the area of the plenum chamber (A_{plen}) is equal to 13.69 m^2.

The total pressure upstream of the fan is the sum of the static and dynamic pressure inside the plenum chamber and is defined as:

$$\Delta p_{\text{t,plen}} = \Delta p_{\text{s,plen}} + p_{\text{d,plen}} \tag{C.13}$$

The fan static pressure rise is the difference between the fan outlet static pressure (which is equal to the atmospheric pressure) and total inlet pressure (BSI Group, 2007). Taking the fact that the measured plenum pressure is the difference between the settling chamber wall static pressure and atmospheric pressure and that it is a negative value, we can calculate the fan static pressure as follows:

$$\begin{aligned}\Delta p_{\mathrm{Fs}} &= p_{\mathrm{atm}} - p_{\mathrm{t,plen}} \\ &= p_{\mathrm{atm}} - (p_{\mathrm{s,plen}} + p_{\mathrm{d,plen}}) \\ &= p_{\mathrm{atm}} - (p_{\mathrm{atm}} + p_{\mathrm{s,plen,rel}} + p_{\mathrm{d,plen}}) \\ &= -p_{\mathrm{s,plen,rel}} - p_{\mathrm{d,plen}} \\ &= p_{\mathrm{s,plen}} - p_{\mathrm{d,plen}}\end{aligned} \tag{C.14}$$

where $p_{\mathrm{t,plen}}$ is the total pressure inside the plenum (settling) chamber, $p_{\mathrm{d,plen}}$ is the dynamic component of the pressure and $p_{\mathrm{s,plen,rel}}$ is the measured static pressure relative to the atmosphere.

The volumetric flow rate through the test facility is calculated by:

$$\dot{V} = \frac{\dot{m}}{\rho_{\mathrm{plen}}} \tag{C.15}$$

Once the torque offset has been taken into account, the power input of the fan can be calculated by:

$$P_{\mathrm{F}} = T_{\mathrm{F}}\omega \tag{C.16}$$

The fan static efficiency is defined as

$$\eta_{\mathrm{Fs}} = \frac{\Delta p_{\mathrm{Fs}}\dot{V}}{P_{\mathrm{F}}} \tag{C.17}$$

and fan total efficiency is defined as

$$\eta_{\mathrm{Ft}} = \frac{\Delta p_{\mathrm{Ft}}\dot{V}}{P_{\mathrm{F}}} \tag{C.18}$$

The fan scaling laws are used to reference the experimental fan data to a standard air density (ρ_{ref}) of 1.2 kg/m^3 and a rotational speed (N_{ref}) of 722 rpm. It should be noted that the scaling of the fan diameter diameter can be omitted as they both the experimental and reference fan have the same diameter. This results in the following equations for the characteristic variables:

$$\Delta p_{\mathrm{Fs,ref}} = \Delta p_{\mathrm{Fs}} \left(\frac{N_{\mathrm{ref}}}{N}\right)^2 \left(\frac{\rho_{\mathrm{ref}}}{\rho}\right) \tag{C.19}$$

$$\dot{V}_{\text{ref}} = \dot{V}\left(\frac{N_{\text{ref}}}{N}\right) \tag{C.20}$$

$$P_{\text{F,ref}} = P_{\text{F}}\left(\frac{N_{\text{ref}}}{N}\right)^3\left(\frac{\rho_{\text{ref}}}{\rho}\right) \tag{C.21}$$

C.4 BSPM calibration

The pressure transducer used in the BSPM module is calibrated using a Betz Manometer setup similar to figure C.1. One side of the transducer is connected to the manometer while the other side is open to the atmosphere. A digital signal is recorded for each pressure calibration reading. The V-link amplification is set to achieve maximum resolution while still allowing all data to be recorded at the upper and lower signal limits. Three calibration sets were conducted in which the results have a maximum relative standard deviation (RSD) of ± 1.69% from the Betz Manometer reading.

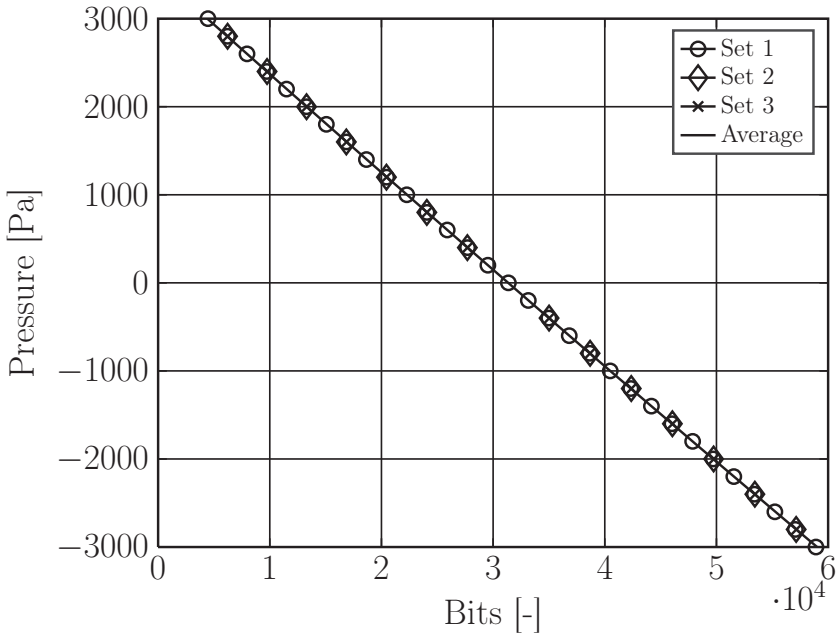

Figure C.6: Calibration curve of a MPX 2010 pressure transducer

A dynamic test was conducted to determine the accuracy of the pressure transducers while in a rotating (test) environment. A pitot tube setup was used as

shown in figure C.7. The measurement side of the pressure transducer is connected to the pitot tube while the reference side is connected to the extended rod in the settling chamber as previously described in section 4.3.

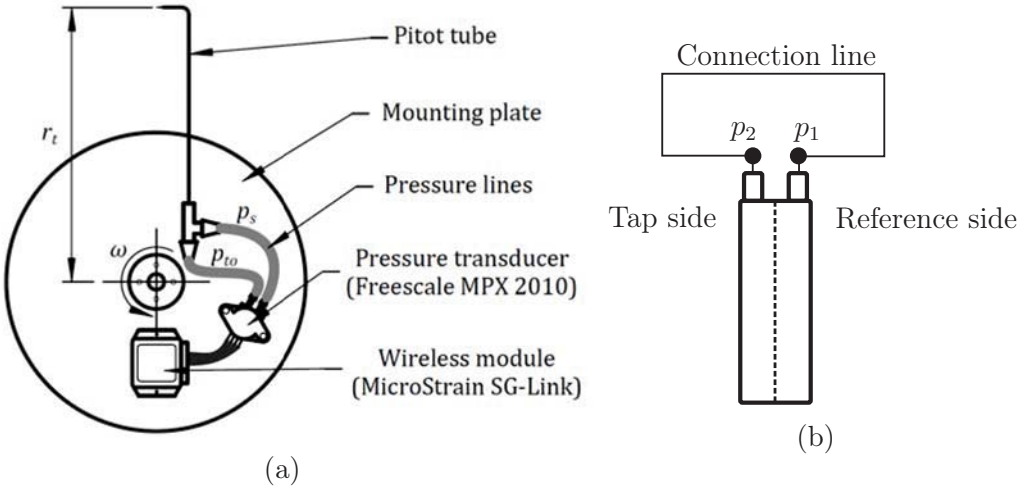

Figure C.7: Experimental setup for (a) dynamic test (Louw, 2015) and (b) centrifugal offset of the BSPM pressure transducer

The setup is rotated at the design operating speed of 722 rpm. The pressure was measured at the pitot tube radius (r_{tip}) of $s_b = 0.9$ and 0.1 for a duration of 10 seconds. This process was repeated three times and included zero measurements for drift calculations. The experimental (dynamic) pressure at the pitot tube tip can be compared to the theoretical dynamic pressure as defined by eqn. C.22.

$$p_{\text{d,theoretical}} = \frac{1}{2}\rho {v_{\text{tip}}}^2 \tag{C.22}$$

where the v_{tip} is the tip velocity and is defined as:

$$v_{\text{tip}} = \omega r_{\text{tip}} \tag{C.23}$$

Three sets of tests were conducted with a maximum standard deviation of 5.3 Pa. The maximum difference between the experimental and theoretical dynamic pressure is 29.26 Pa and occured at a blade span of 0.9. The theoretical dynamic pressure is always above the experimental dynamic pressure. This compares similarly with the results of Louw (2015) who found that the pressure transducers have a max. deviation of 35.19 Pa below the theoretical

values at a speed of 750 rpm. It is not clear what the reason is for the error. Louw (2015) explains that the reason could be due to the pitot tube wake interfering with the experimental results. It is however unclear whether the unaccuracy lies with the pressure transducer and no offset will be added as a result of these tests.

Even though the pressure transducer is located parallel to the fan shaft, the pressure transducer membrane can experience a possible offset during fan rotation. An experiment is conducted with the pressure transducer arrangement shown in figure C.7. Each pressure transducer's outlets are connected to each other, allowing measurement of any centrifugal offset in the transducer during fan rotation. Three experimental runs were conducted and a maximum offset of 4.5 Pa was measured at an operating speed of 722 rpm.

C.5 BSPM calculation

The measured blade surface pressure at the tap location carries an offset due to the rotation of the fan during measurements. A very small offset is due to the pressure transducer membrane as experimentally determined in the previous section. A much larger pressure offset is due to the force caused by the air that is constrained in the blade channels.

The pressure taps are located at various radial (channel) distances from the pressure transducers. A centrifugal (radial) force is induced which effectively results in a higher measured pressure difference than actually present. A derivation of the pressure offset due to the blade channel distance to the pressure tap is firstly presented in section C.5.1. This result is then incorporated to complete the calculation procedure required for the actual pressure value at the blade tap.

C.5.1 Centrifugal pressure offset in blade channel

The derivation for centrifugal pressure distribution along the radius of the blade channel is taken from Louw (2015). A control volume of air is constrained at an angle in the blade channel between the pressure tap and pressure transducer as shown in figure C.8.

The control volume is located at a height y, at which the pressure due to centrifugal forces can be given as:

$$\mathrm{d}p = \frac{\mathrm{d}F_{\mathrm{n}}\cos\lambda}{A} \tag{C.24}$$

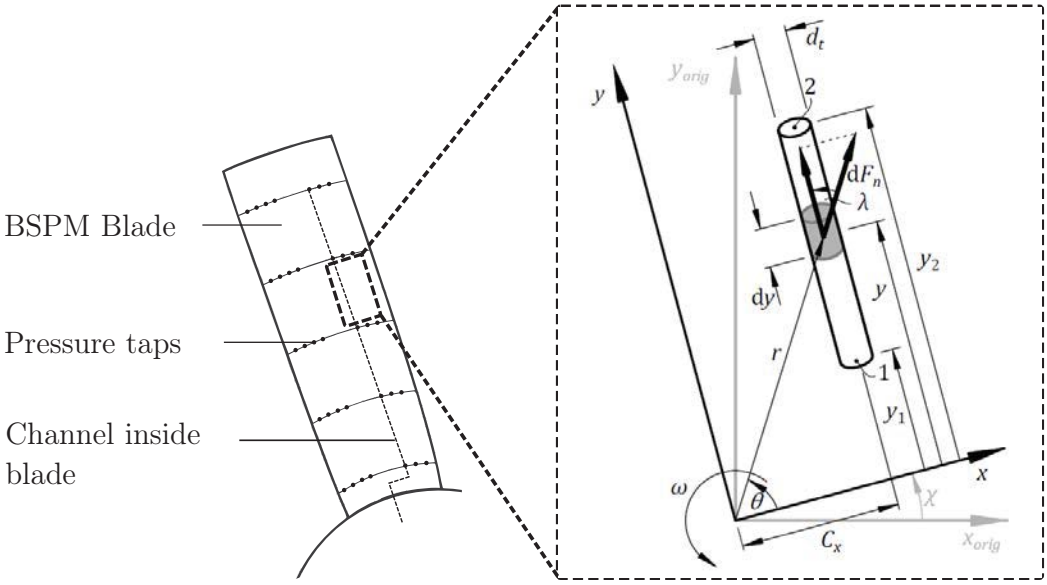

Figure C.8: BSPM derivations for centrifugal forces, adapted from Louw (2015)

where

$$A = \frac{\pi d_{\mathrm{t}}}{4} \tag{C.25}$$

$$\lambda = \frac{\pi}{2} - \theta \tag{C.26}$$

and

$$\theta = \arctan\left(\frac{y}{C_x}\right) \tag{C.27}$$

The normal force, $\mathrm{d}F_{\mathrm{n}}$ in equation C.24 can be defined as:

$$\mathrm{d}F_{\mathrm{n}} = a_{\mathrm{n}}\mathrm{d}m \tag{C.28}$$

where

$$\mathrm{d}m = \rho_{\mathrm{a}} A \mathrm{d}y \tag{C.29}$$

and

$$a_{\mathrm{n}} = \omega^2 r = \omega^2 \sqrt{y^2 + C_x^2}. \tag{C.30}$$

The fluid density is determined assuming the ideal gas law given by:

$$\rho_{\mathrm{a}} = \frac{p}{RT} \tag{C.31}$$

The mass of air in the control volume can be calcululated as follows:

$$\mathrm{d}m = \frac{pA\mathrm{d}y}{RT} \tag{C.32}$$

Substituting the above equations into equation C.24, the differential pressure as a function of y becomes:

$$\mathrm{d}p(y) = \frac{p(y)\omega^2\sqrt{y^2+C_x^2}\cos\left[\frac{\pi}{2} - \arctan\left(\frac{y}{C_x}\right)\right]\mathrm{d}y}{RT} \tag{C.33}$$

Integrating the above equation gives:

$$\begin{aligned}\int \frac{\mathrm{d}p(y)}{p(y)} &= \frac{\omega^2}{RT}\int \sqrt{y^2+C_x^2}\cos\left[\frac{\pi}{2} - \arctan\left(\frac{y}{C_x}\right)\right]\mathrm{d}y \\ \ln p(y) &= \frac{\omega^2}{RT}\int \sqrt{y^2+C_x^2}\frac{y}{\sqrt{y^2+C_x^2}}\mathrm{d}y \\ &= \frac{\omega^2 y^2}{2RT} + C \end{aligned} \tag{C.34}$$

The equation can now be represented as a function of the radius by using the substitution $y = \sqrt{r^2 - C_x^2}$ which gives:

$$\begin{aligned}\ln p(r) &= \frac{\omega^2(r^2 - C_x^2)}{2RT} + C \\ &= \frac{\omega^2 r^2}{2RT} - \frac{\omega^2 C_x^2}{2RT} + C \\ &= \frac{\omega^2 r^2}{2RT} + C_1 \end{aligned} \tag{C.35}$$

From eqn. C.35 it is shown that the centrifugal pressure distribution inside the channels is dependent only on the radius, rotational speed and air temperature.

C.5.2 Measurment correction for BSPM

This section details the procedure to calculate the actual static pressure at the blade tap from the measured data from the pressure transducer. A schematic of the pressure chain for the BSPM setup is shown in figure C.9. The reference side of the transducer is connected to an extended rod and measures the total pressure inside the plenum chamber $p_{\mathrm{t,plen}}$ as detailed in section 4.3. Referring to figure C.9, the tap side of the transducer is connected to the blade channels which lead to the pressure taps.

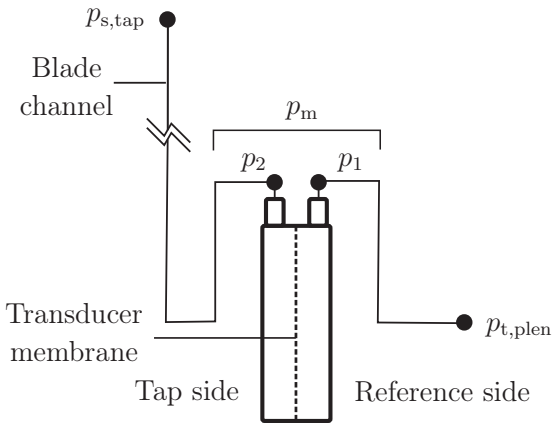

Figure C.9: Schematic of blade surface pressure measurement

The pressure difference measured by the transducer is defined by:

$$\Delta p_m = p_2 - p_1 + \Delta p_{zero} \tag{C.36}$$

where Δp_{zero} is the initial offset in the transducer membrane due to rotation discussed in the previous section. The absolute pressure at the reference side is defined as:

$$p_1 = p_{t,plen} + p_{atm} \tag{C.37}$$

The absolute pressure at the pressure transducer tap side is defined as:

$$p_2 = p_{s,tap} + p_{atm} - \Delta p_n \tag{C.38}$$

where $p_{s,tap}$ is the actual static pressure at the blade pressure tap location and Δp_n is the difference due to the centrifugal offset of air in the blade channels at the specific blade pressure tap radius r_{tap} as discussed in the previous section.

The boundary conditions at the pressure tap and pressure transducer with regards to the centrifugal offset are as follows:

At r $= 0$, $p_n = 0$ and
at r $= r_{tap}$, $p_n = p_{n,tap}$

where p_n is the pressure at the transducer due to centrifugal forces and $p_{n,tap}$ the pressure at the tap location due to centrifugal forces. These boundary conditions are now applied to eqn. C.35 as follows:

$$\ln p(r) = \frac{\omega^2 r^2}{2RT} + C_1 \tag{C.35 revisited}$$

At r = 0:

$$\begin{aligned} \ln(p_{\mathrm{n}}) &= 0 + C_1 \\ &= C_1 \end{aligned} \tag{C.39}$$

Applying the boundary condition at r = r_{tap} and substituting the result from eqn. C.39 into eqn. C.35 results in:

$$\ln(p_{\mathrm{n,tap}}) = \frac{\omega^2 {r_{\mathrm{tap}}}^2}{2RT} + \ln(p_{\mathrm{n}}) \tag{C.40}$$

We can now rearrange and integrate this results in a final equation for the pressure offset due to the centrifugal offset in the blade channels (Δp_{n}) as follows:

$$\begin{aligned} \frac{\omega^2 {r_{\mathrm{tap}}}^2}{2RT} &= \ln(p_{\mathrm{n,tap}}) - \ln(p_{\mathrm{n}}) \\ &= \ln\left[\frac{p_{\mathrm{n,tap}}}{p_{\mathrm{n}}}\right] \\ \int \ln\left[\frac{p_{\mathrm{n,tap}}}{p_{\mathrm{n}}}\right] &= \int \frac{\omega^2 {r_{\mathrm{tap}}}^2}{2RT} \\ \frac{p_{\mathrm{n,tap}}}{p_{\mathrm{n}}} &= \mathrm{e}^{\omega^2 {r_{\mathrm{tap}}}^2/2RT} \\ p_{\mathrm{n,tap}} &= p_{\mathrm{n}} \mathrm{e}^{\omega^2 {r_{\mathrm{tap}}}^2/2RT} \end{aligned} \tag{C.41}$$

We can now define the difference in pressure due to centrifugal pressure as follows:

$$\begin{aligned} \Delta p_{\mathrm{n}} &= p_{\mathrm{n,tap}} - p_{\mathrm{n},0} \\ &= p_{\mathrm{n},0}\left(\mathrm{e}^{\omega^2 {r_{\mathrm{tap}}}^2/2RT} - p_{\mathrm{n}}\right) \end{aligned} \tag{C.42}$$

Substituting eqn. C.42 back into eqn. C.38 results in:

$$\begin{aligned} p_2 &= p_{\mathrm{s,tap}} + p_{\mathrm{atm}} - p_2\left(\mathrm{e}^{\omega^2 {r_{\mathrm{tap}}}^2/2RT} - 1\right) \\ &= \frac{p_{\mathrm{s,tap}} + p_{\mathrm{atm}}}{\mathrm{e}^{\omega^2 {r_{\mathrm{tap}}}^2/2RT}} \end{aligned} \tag{C.43}$$

Substituting the above and eqn.C.37 back into eqn.C.36 results in the following:

$$\Delta p_{\mathrm{m}} = \frac{p_{\mathrm{s,tap}} + p_{\mathrm{atm}}}{\mathrm{e}^{\omega^2 {r_{\mathrm{tap}}}^2/2RT}} - p_{\mathrm{t,plen}} - p_{\mathrm{atm}} + \Delta p_{\mathrm{zero}} \tag{C.44}$$

By rearranging the above, we can finally derive the actual blade surface pressure at the blade tap as follows:

$$p_{\mathrm{s,tap}} = \mathrm{e}^{\omega^2 {r_{\mathrm{tap}}}^2/2RT}(\Delta p_{\mathrm{m}} + p_{\mathrm{t,plen}} + p_{\mathrm{atm}} - \Delta p_{\mathrm{zero}}) - p_{\mathrm{atm}} \tag{C.45}$$